Photoionization of Cold Atoms and Non-Neutral Plasma Dynamics

by

Michael Anthony Viray

A dissertation submitted in partial fulfillment
of the requirements for the degree of
Doctor of Philosophy
(Physics)
in the University of Michigan
2021

Doctoral Committee:

Professor Georg Raithel, Chair
Professor Steven Cundiff
Professor Alex Kuzmich
Professor Vanessa Sih
Professor Alexander Thomas

Michael Anthony Viray

mviray@umich.edu

ORCID ID: 0000-0001-5296-3907

“If you learn to use it right, the adversity, it will buy you a ticket to a place you couldn’t have gone any other way.”

-Tony Bennett

ACKNOWLEDGEMENTS

Experimental physics is best when done collaboratively, and I have many people to thank for their mentorship and mutual effort. First and foremost, thank you to my advisor, Georg Raithel, for taking me on as his student. I have learned so much from you, and I hope that one day I can be half the physicist you are. Special thanks as well to Stephanie Miller, who was my main mentor during my first two years of grad school, and Lu Ma, Prof. Eric Paradis, Leo Nofs, and Cainan Nichols for their hard work and helpfulness in our shared projects. Shout out to the many members of Raithel Group, both past and present, for their friendship along the way: Ryan Cardman, Alisher Duspayev, Pound Thaicharoen, Andira Ramos, Jamie MacLennan, Kaitlin Moore, David Anderson, and Rachel Sapiro. Thank you for the baked goods, conference memories, and many fun times.

Thank you to Profs. Vanessa Sih, Steve Cundiff, Alex Kuzmich, and Alec Thomas for serving on my defense committee. Profs. Sih and Cundiff also served on my prelim committee, and I am happy to have them on my defense committee for continuity.

Thank you as well to the people who gave me research opportunities before graduate school and helped prepare me for life as a Ph.D. student. Thank you to Prof. Robert Jones, Prof. Craig Sarazin, and David Van Petten for my research experiences as an undergraduate student at the University of Virginia, and thank you to Prof. Tom Killian, Joe Whalen, Roger Ding, and Francisco Camargo for welcoming me into their research group at Rice University as an REU student.

I also have many teachers to thank for inspiring me in their classrooms. Thank you in particular to Profs. Ted Norris, Herbert Winful, and Almantas Galvanauskas from UMich, Profs.

Craig Group, Keith Williams, and Rick Marshall from UVA, and Dr. John Barnes and Ms. Jennifer Todd from Maggie Walker Governor's School. You all helped me become the scientist I am today.

Part of what makes the UMich physics department so great is its positive culture, and I believe that much of that can be attributed to the staff. I'd like to recognize Paul Thurmond, Lauren Segall, Nitesh Singh, Chrissy Zigulis, Elise Bodei, and Ana Austin for being great to work with, and for being the heart and soul of the department. Thank you as well to Jim Tice and Dave Carter of the machine shop for teaching me how to use the machine equipment, and for making custom parts for my experiments.

I think it goes without saying that physics graduate school is a grind, and I never could have made it without the friends I've made along the way. Thank you to Rachel Hyneman, Callum Jones, Brandon and Kate Berg, Steve Novakov, Joe and Alissa Kleinhenz, Brian McPeak, Chris Barnes, Taylor Baildon, Stephen DiIorio, Shruti Paranjape, Josh Foster, Noah Steinberg, and Melissa Hutcheson, among many others. You all have made these years unforgettable, and I hope that we continue to stay in touch long after our grad school days are behind us.

Equally important are my friends outside of school, who have kept me tethered and given me support over the years. Thank you to my New Years crew: Steven Gizzi, Tim Swartz, and Colin Greatwood. Your friendship means the world to me, and I can't wait to celebrate with you when I see you again. Thank you as well to Tucker Dean, Joy Whitehurst, Christian Boughner, and the rest of my friends back home for keeping RVA special to me.

Finally, thank you to my parents, Carla and Willie Viray, my brother Joey, and my grandmother Kathleen Cripe for their love and support from the very beginning. 2021 is shaping up to be a big year for all of us, and I look forward to welcoming Kailey Washok into our family as my sister-in-law.

TABLE OF CONTENTS

LIST OF FIGURES

FIGURE

LIST OF TABLES

TABLE

LIST OF APPENDICES

APPENDIX

LIST OF ABBREVIATIONS

MOT magneto-optical trap

AOM acousto-optic modulator

BEC Bose-Einstein condensate

PDL pulsed dye laser

PI photoionization

NIR near-infrared

UV ultraviolet

EDA electric dipole approximation

LVIS low-velocity intense source

FWHD full width at half depth

RMS root-mean-square

BLOB ball lens optical box

AMO atomic, molecular, and optical

MCP micro-channel plate

EIT electromagnetically-induced transparency

TBR three-body recombination

DIH disorder-induced heating

TIP tip ionization probe

ABSTRACT

The development of atom trapping and cooling techniques has been a boon for the field of low temperature plasma physics. By forming plasmas through photoionization (PI) of cold atoms, researchers are able to create cold, dense plasmas that often lie in the strong-coupling regime. This is especially remarkable considering that many naturally-occurring plasmas in the strong-coupling regime are in inaccessible environments (e.g. the insides of stars and gas planets), whereas these laboratory-based plasmas prepared in cold-atom systems are relatively easy to produce and analyze with standard AMO techniques.

In this thesis, I present my work from several projects on photoionization, plasma formation and dynamics, and plasma trap development. I first discuss an experiment that I spearheaded on expansion dynamics in cold, non-neutral plasmas. In this experiment, cold plasmas are formed by photoionizing rubidium atoms in a MOT, and the resulting plasma ions are allowed to expand for a variable wait time before being imaged with a single-ion imaging system. This ion imaging system, along with the rest of the experimental setup, was originally used to study Rydberg atoms. I have adapted the setup for plasmas by installing a new laser and changing the experimental timings. I report on plasma features seen in this experimental setup, such as shock shells and time-evolved ion pair correlations. This study of non-neutral plasma expansion is complete, but the same experimental setup can be adapted to look at new configurations such as neutral plasmas or plasma collisions.

I also present findings from a computational study of wavelength-dependent PI of Rydberg atoms, namely Rydberg-state rubidium and cesium. The main goal of the study is to find PI minima, wavelengths where the atom's PI cross section decreases dramatically. These minima can be caused by Cooper minima or shape resonances, which each have their own telltale signs.

This computational study paves the way for an informed experimental measurement of the locations of some of the identified PI minima, and comparing their experimental locations with the computational results. This is, in part, interesting because the latter depend on whether length or velocity gauge is used. An experimental measurement of PI cross sections could be a good way to explore the significance of gauge dependence in ℓ-dependent potentials. While this study is outside the scope of plasma physics, it is relevant in that it is a direct study of photoionization, and that it may be conducted in the same ion imaging chamber as the expansion study. The results of this study were recently published.

I conclude with a discussion of a project centered on creating a small MOT with diverging cooling beams inside of a metal enclosure. This project was a collaboration with researchers at Eastern Michigan University. The idea to make a MOT with these design features was born out of plans for cryostatic plasma experiments. Now, it has potential applications in plasma experiments, precision measurements, and quantum information. Design-wise, the diverging beams are formed by sending narrow laser beams into 1.5 mm ball lenses, which cause the beams to diverge rapidly. Six ball lenses, one for each cooling beam, are mounted on a metal structure called the ball lens optical box (BLOB), which encases the trapped atom cloud. This enclosure provides immediate benefits for plasma experiments, as it offers Faraday shielding from stray electric fields. The first build successfully produced and maintained a MOT, making it the first known case of a MOT made with diverging beams from ball lenses. No further experiments are planned for this first build, but the concept of a ball lens MOT will certainly be implemented into future experimental efforts. Subsequent designs may include more design features, such as interior electrodes for custom field configurations. The design may also be implemented in precision measurement and atomic clock experiments, as the enclosure helps reduce perturbations from blackbody radiation.

CHAPTER 1

Introduction

Plasma, often referred to as the fourth state of matter, is produced when particles become ionized, resulting in a charged, gaseous substance. Ionization can happen in a variety of ways, including collisions, electric discharge, and thermal ionization. Plasma is by far the most abundant form of matter in the visible universe; 99% of normal, baryonic matter can be described as plasma and is found in stars and the interstellar medium. Plasma can be found at all length scales, from the aforementioned astrophysical systems to subatomic particle size (e.g. quark-gluon plasma), and it can also be found in relativistic settings. Plasma can also be seen in everyday settings, such as in lightning and neon signs. Most physics students are familiar with the Jacob's Ladder, shown in Fig 1.1, which is often used to demonstrate plasma formation. Figure 1.2 lists additional sources of plasma, both naturally occurring and manmade, along with their temperatures and densities.

In this thesis, I discuss plasmas from the perspective of atomic, molecular, and optical (AMO) physics. In the AMO context, plasmas are typically made from photoionized atoms, which can be either at room temperature in vapor cells, or at millikelvin temperatures in cold atom traps. Over the course of this introduction, I will explain why AMO labs are good environments for plasma experiments, and I will give a brief overview of recent plasma/AMO experiments.

1.1 Photo-excited Laboratory Plasmas

There are several factors that make AMO labs well-suited for plasma studies. Photoionization, which often is the tool of choice for forming plasmas in these environments, is accessible, easy to set up, and creates plasmas with predictable initial conditions. Another benefit is the ability to produce plasma from cold atoms, thereby creating cold plasma. In plasma physics, one of the most important physical parameters is the Coulomb coupling parameter, Γ. For a single-component plasma, Γ is defined as:

$$\Gamma = \frac{q^2/(4\pi\varepsilon_0 r_{WS})}{k_B T} \tag{1.1.1}$$

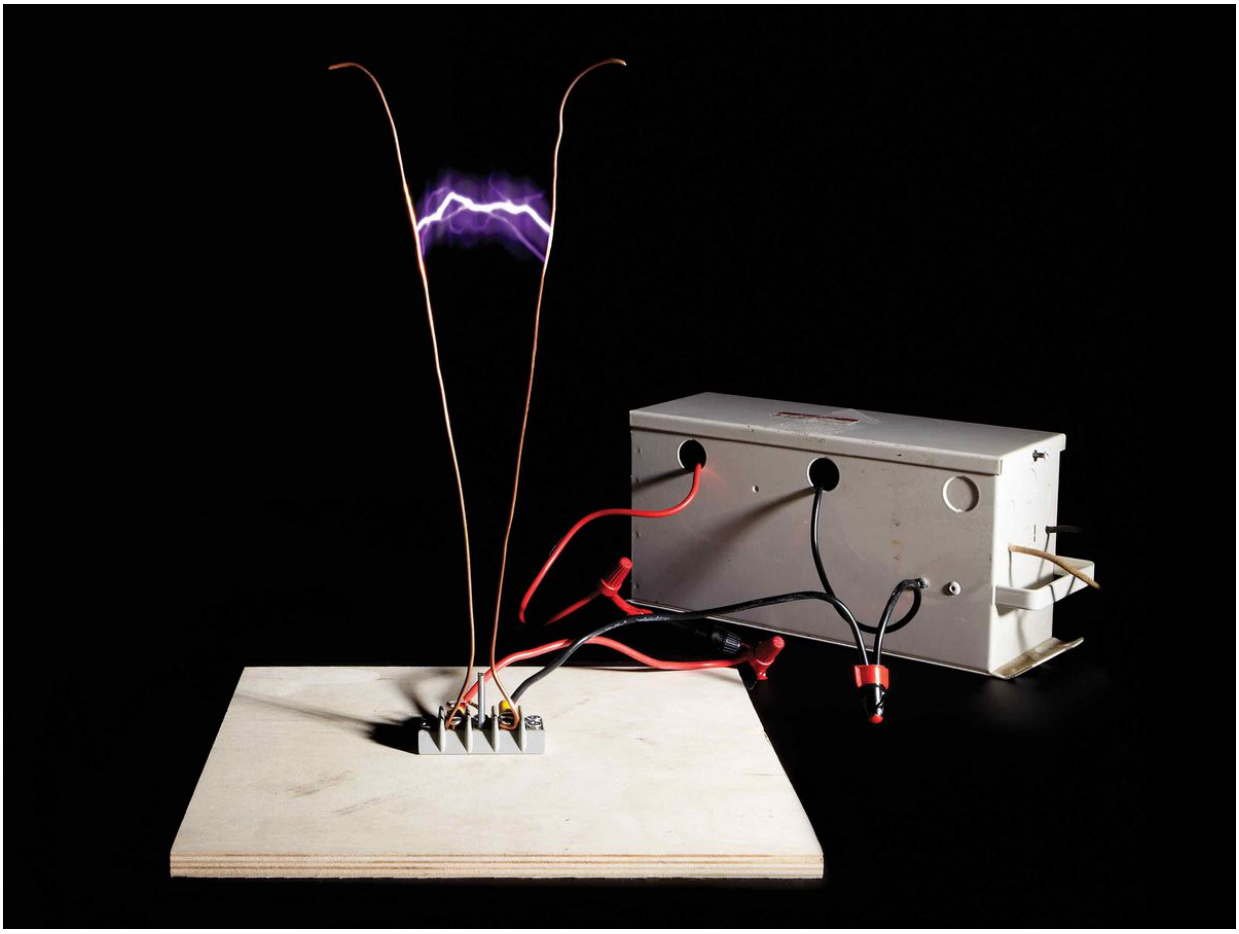

Figure 1.1: A Jacob's Ladder device. The leads are placed at a high potential difference, causing the air in between to ionize into plasma and conduct an arc current. The plasma is hotter than the surrounding air, and it rises up the electrical leads before dissipating. Photo credit: Brian Klutch, https://www.popsci.com/how-to-build-jacobs-ladder/

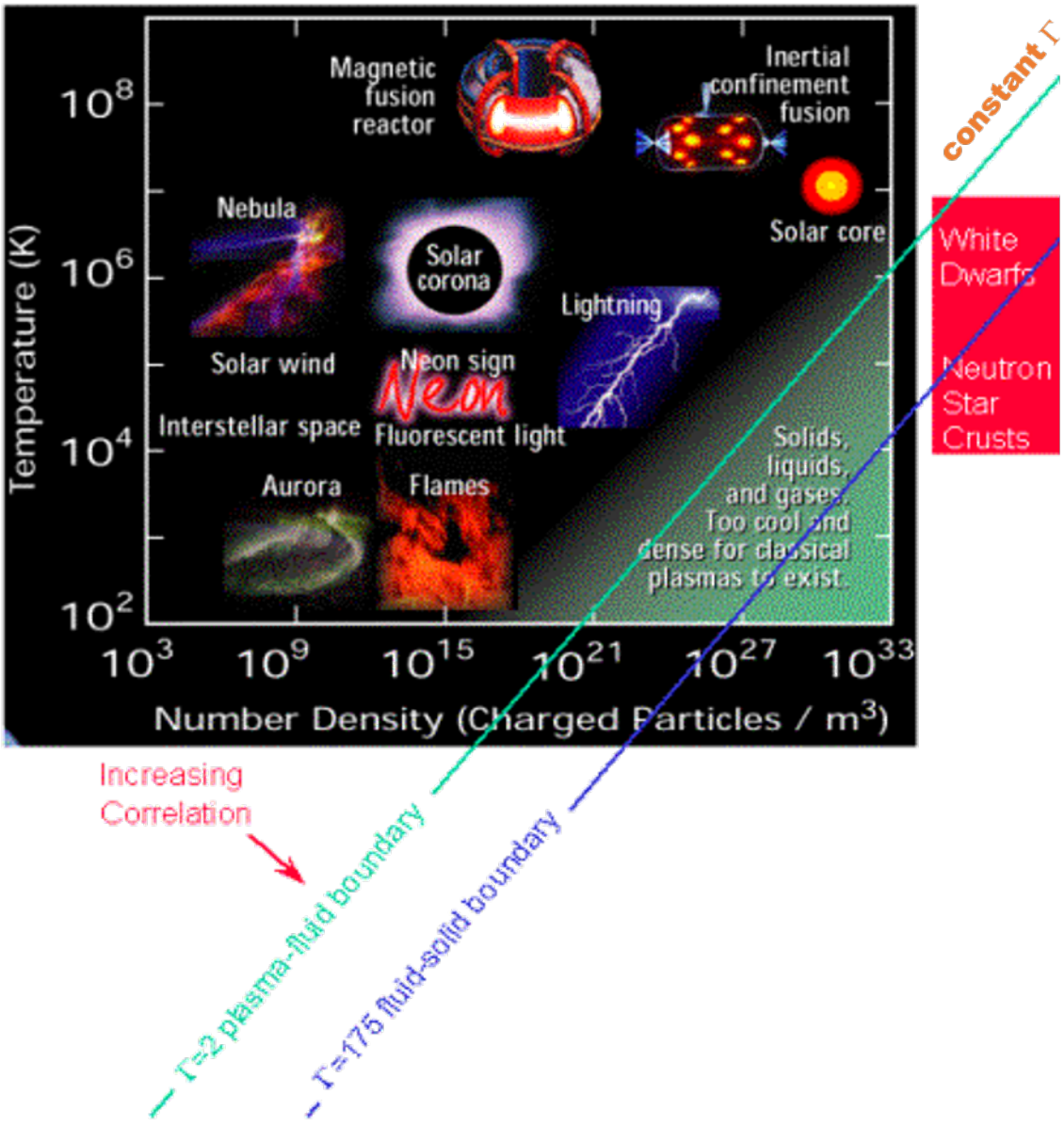

Figure 1.2: Log-log plot of temperatures and densities of various plasma sources, both naturally-occurring and manmade. The green and blue diagonal lines represent constant Γ values. Most examples of plasma are weakly coupled, meaning their thermal energy is much greater than their electrostatic energy ($\Gamma < 1$). Image credit: http://www.physics.udel.edu/wwwusers/mitchell/research-interests.html

Here, q is the plasma particle charge, ε_0 is the permittivity of free space, k_B is the Boltzmann constant, and T is the temperature. r_{WS} is the Wigner-Seitz radius and is defined as:

$$r_{WS} = \sqrt[3]{3/(4\pi n_V)} \tag{1.1.2}$$

Here, n_V is the volume density of the plasma.

The Coulomb coupling parameter will be explained in greater detail in Chapter 3. The gist is that it describes the ratio of a plasma's electrostatic energy to its thermal energy, and a plasma with $\Gamma \gtrsim 1$ is considered "strongly coupled." Strongly-coupling plasmas are of interest to researchers because, although they occur naturally, they are rare and typically form in hard-to-observe environments. This point is further emphasized in Fig. 1.2 by the green and blue diagonal lines. These lines represent constant Coulomb coupling parameter; green represents $\Gamma = 2$, which are plasmas that are barely in the strong-coupling regime, while blue represents $\Gamma = 175$, which are plasmas that are firmly entrenched in the strong-coupling regime. As Fig. 1.2 shows, naturally-occurring strongly-coupled plasmas can only be found in white dwarfs and neutron star crusts, astrophysical environments that have significantly lower temperatures than the interiors of stars but are no more accessible.

One way to circumvent this problem is to create strongly-coupled plasmas in the lab, and since Eq. 1.1.1 tells us that coupling strength is inversely proportional to temperature, it stands to reason that cold plasmas allow for easy access to the strong-coupling regime. It should come at no surprise, then, that the development of atom trapping and cooling processes [3–5] has been a boon for experimental plasma physics. A MOT, a common cold-atom trap configuration, typically holds atoms at a temperature of $\sim$100 μK. If these atoms are then photoionized, the resulting initial plasma temperature is somewhere in the millikelvin range, depending on factors such as the ionization wavelength. This initial temperature, and potential subsequent cooling processes, can yield strongly-coupled ion plasmas. More information on cold plasma experiments will be covered later in this chapter, as well as in Chapter 4.

AMO laboratories are also well-suited for plasma experiments in that many of the measurement and analysis techniques and equipment can be easily adapted for studying plasmas. Two techniques that I would like to highlight in particular are ion imaging and atom-based field sensing. Ion imaging, as the name suggests, is the process of producing images of ions that have minimal distortion and preserve spatial distribution. It works by directing ions through focusing and/or collimating tubes (often referred to as ion optics, due to their similarity to light and lenses) and into a detector called a micro-channel plate (MCP). Ion imaging has been used in the past to investigate Rydberg blockade radii [6], van der Waals interactions [7], and dipole-dipole interactions [8]. While these three experiments centered around Rydberg atoms, not plasma, the imaging system functioned the exact same way (in the Rydberg experiments, the Rydberg atoms

were field-ionized by the imaging electric field). Ion imaging has also been used by other groups to study ionization spectra [9, 10], tunnel ionization rates [11], and quantum gases [12].

Atom-based field sensing is a technique that is mostly utilized in vapor cells. The driving principle is a phenomenon called EIT, which is capable of producing narrow, Doppler-free atomic transition signals. Appendix B contains a more thorough explanation of how EIT works. If one of the coupled states in the EIT scheme happens to be a Rydberg state, the EIT signal becomes highly sensitive to external fields. When present, external fields induce a quantum mechanical effect called the Stark Effect, which causes shifting and/or splitting of atomic energy levels. The Stark Effect has a greater effect on higher-lying/Rydberg states due to increased dipole moment and polarizability (see Sec. 2.2), and the shifting and splitting manifest themselves in the EIT signal. Once the shifting/splitting has been measured, the magnitude of the external field can be calculated if certain quantities like transition dipole moment or polarizability are known. This makes Rydberg-EIT a very good tool for measuring both AC and DC electric fields. This technique has been used by many groups to observe a variety of electric fields, including RF [13, 14], microwave radiation [15–18], and DC electric fields [19]. Plasmas, meanwhile, produce interesting electric fields of their own. For example, the electric fields of many plasmas can be described by a statistical distribution called the Holtsmark distribution [20]. EIT can be used, among other uses, to measure the spatial distribution of a plasma's electric field and see how it compares to the Holtsmark distribution. To summarize, Rydberg-EIT is a versatile, non-invasive method of measuring a plasma's electric field, and it is also accessible to most AMO labs.

With these various techniques, AMO physicists have been able to greatly contribute to experimental plasma physics. Atom trapping and cooling has made it possible to create cold, photoexcited plasmas in the laboratory, both neutral and non-neutral [21–24]. This enables models that scale to hard-to-access plasmas that occur, for instance, in astrophysical environments (insides of stars and gas planets) [25], magnetic-confinement fusion [26, 27], and inertial-confinement fusion [28, 29]. Recent work in cold plasma physics has explored plasma laser cooling [30], pair correlations [31–34], dual-species ion collisions [35, 36], Rydberg atom-plasma interactions [37], plasma field-sensing applications [38], and quenched randomness and localization [39]. Rydberg-EIT, meanwhile, has been used in vapor cell plasmas to characterize plasma electric fields [20, 40].

One area of interest in laboratory plasma physics is the expansion of plasma into vacuum [41–43], a topic that has been of interest, for instance, because of its parallels to astrophysical systems [44, 45]. Non-neutral plasma expansion, in particular, is known as Coulomb expansion [38, 46, 47]. Expanding non-neutral plasmas can exhibit several interesting phenomena such as vortices [48], Bernstein modes [49], and shock shells. Shock shells form in Coulomb explosions if, initially, the outer layer of ions is less dense than the center [50, 51]. If so, intermediate layers of the plasma tend to catch up with peripheral layers, and form a higher-density shock shell. Shock fronts form in both spherically-symmetric and cylindrically-symmetric plas-

mas [50]. They can form in a wide variety of non-neutral plasmas, including relativistic electron clouds [52]. Rapidly expanding plasmas also are intriguing thermodynamic systems [43]. As the plasma expands, the temperature changes globally in time due to disorder-induced heating and adiabatic cooling [53], and locally in space across the shock shells [51]. Shock shells and expansion thermodynamics will be discussed in greater detail in Chapter 4.

1.2 Ion Plasma Traps

While some experiments study plasmas that are generated in free space and freely expanding/moving, other experiments require the plasma to be held in place by some sort of trap. Ion trapping shares some similarities with atom trapping, but the fundamental difference between the two is that ions are charged, thus ion traps can make use of electric fields [1]. It is important to note, though, to consider Earnshaw's theorem, which states that charged particles cannot be trapped by a static electric field alone. Therefore, ion traps either have dynamic electric fields, or combinations of electric and magnetic fields.

Two of the most popular ion trap configurations are the Paul trap and the Penning trap. The Paul trap uses a dynamic electric field to trap ions. It works by forming an electric quadrupole field, which is then rotated about its center at a fast enough rate to create a stable potential well. This can be visualized by imagining a ball sitting on a saddle. The saddle represents the quadrupole field, with areas of higher and lowed potential. If the ball is placed at the center of the saddle and is nudged, the ball is likely to roll off the side of the saddle. However, if the saddle is spun fast enough, it forms a stable well, and the ball will remain inside the well even if nudged. These are the exact same principles at play in the Paul trap, except we are dealing with an electric potential well instead of a gravitational potential well.

The Penning trap also contains a quadrupole electric field, but in this case the field is static instead of dynamic. Additionally, there is a constant magnetic field along the axis of symmetry of the quadrupole electric field. The electric field on its own does not trap the ions, but the magnetic field causes the moving ions to rotate in a circle, confining them to the center of the trap.

Currently, there is considerable interest in designing structures with embedded electrodes for both vapor cell and cold atom experiments. Embedded electrode systems with appropriate spatial symmetry can be used to make compact Penning [54, 55] and Paul traps [56]. In vapor cells, silicon electrodes have been successfully bonded to glass and integrated into the bodies of vapor cells; more on this can be found in Chapter 7 and in [57]. In cold atom experiments, several groups have implemented compact Penning traps into their atom cooling setups [58–60]. These compact ion traps are often entirely contained in metal structures, which provide additional benefits. First, and most obviously, the metal enclosure provides Faraday shielding. Plasmas are

easily perturbed by stray electric fields, so Faraday shielding is important for preventing unwanted effects from stray fields. Metal enclosures also result in well-defined boundary conditions, which is important for ion trap design. The benefits of metal enclosures for cold atoms extend beyond plasma physics; precision-measurement and atomic-clock experiments that employ MOTs are susceptible to black-body radiation shifts [61–64] and DC Stark shifts [65], both of which metal enclosures can protect against. Chapter 6 discusses metal atom/ion enclosures in further detail and presents a successful proof-of-principle test of a MOT made with diverging cooling beams inside of a metal box.

1.3 Thesis Outline

The body of this thesis is split into two main parts: background information (Chapters 2 and 3), and research (Chapters 4, 5, and 6).

Chapter 2 is a review of atomic physics. I discuss atom cooling and trapping, which is essential for the experiments. I also discuss other relevant aspects of atomic physics, including Rydberg atoms and photoionization.

Chapter 3 is a summary of the relevant plasma physics for this thesis. I talk about how plasmas are quantitatively defined, what makes a plasma "strongly coupled," and how expanding plasmas behave.

In Chapter 4, I present a study of expanding non-neutral plasmas made from cold, photoionized atoms. The plasma is formed, allowed to expand for a predetermined wait time, and imaged with an ion imaging system. By adjusting the wait time, I can observe the plasma as it expands over several microseconds. In this chapter, I observe plasmas at two different densities and highlight the different phenomena that appear at each density. I also compare the experimental findings to computer simulations.

In Chapter 5, I take a deeper dive into the process of photoionization and study the process in Rydberg-state atoms. I present calculations of wavelength-dependent photoionization cross sections for Rydberg atoms, and I discuss the occurence of cross section minima, caused by both Cooper minima and shape resonances. These calculations are performed for rubidium and cesium.

Chapter 6 returns to the experimental side with a look at the ball lens MOT, a development which has the potential to be implemented in future plasma experiments, particularly plasma trapping. I discuss the construction of the apparatus and present experimental data and analysis of the MOT. I also present a corresponding simulation that notes the differences between this MOT and a traditional design, and predicts expected trapped atom number given the physical

parameters.

Chapter 7, the conclusion, summarizes the thesis and discusses future research plans related to these experiments.

CHAPTER 2

Atomic Physics Background

Atomic physics provides the backdrop for all of the studies presented in this thesis, as well as all future plasma projects in the group. As was mentioned in Chapter 1, the experimental methods and equipment in AMO labs allow for easy access to the plasma strong coupling regime through photoionization of cold atoms. Cold atoms in general are critical to many atomic physics experiments, and at this point there are numerous atom trapping and cooling techniques. The formation of an atom-based Bose-Einstein condensate (BEC), for example, uses a combination of several different trapping and cooling techniques performed in a specific order. A full review of atomic cooling and trapping techniques is beyond the scope of this chapter and can be found in books such as *Laser Cooling and Trapping* by Metcalf [4]. Instead, this chapter will present an in-depth look at one specific type of cold atom trap, the MOT. I will discuss the underlying physics that govern the classic, six-beam MOT design. This information is particularly relevant to Chapter 6, where a new MOT design is presented.

The second half of this background chapter will be dedicated to Rydberg atoms, which are the central subject of Chapter 5. Rydberg atoms are useful for pure photoionization studies, and they can also be used as probes for studying plasma electric fields. I will discuss the physical properties of Rydberg atoms, along with other relevant information for photoionization and plasma studies. More in-depth information on Rydberg atoms can be found in *Rydberg Atoms* by Gallagher [2] and *Rydberg States of Atoms and Molecules*, a collection of texts edited by Stebbings and Dunning [66].

2.1 The Magneto-Optical Trap

The MOT is one of the most widespread cold atom configurations in AMO research. The classic design consists of six orthogonal laser beams with specific polarizations, and a quadrupole magnetic field whose field zero is centered at the intersection point of the lasers. In a way, the MOT

can be seen as a successor to optical molasses, which is another cooling configuration that features six orthogonal beams but no quadrupole field. Aside from the physics differences between a MOT and an optical molasses, a MOT can typically contain more atoms than a molasses can (a MOT can hold $10^8 - 10^{10}$ atoms, depending on how it is loaded, etc.). Optical molasses, on the other hand, can reach cooler atom temperatures than a MOT, so it is not uncommon to have experimental sequences where a MOT stage is immediately followed by a molasses stage.

2.1.1 Underlying Physics

The power of the MOT comes from its ability to both trap and cool atoms. The cooling mechanism is optical molasses which, as the name suggests, is a purely optical phenomenon that is driven by the six orthogonal laser beams. Optical molasses works as follows: first, a cooling transition for the specific atomic species is chosen (this frequency is ω_0). Then, the lasers are set to a frequency ω that is slightly red-detuned from the cooling frequency ($\omega < \omega_0$). Once the laser configuration is ready, atoms are loaded into the center of the molasses. If an atom is sitting immobile at the intersection point of the six beams, the atom will experience equal and opposite radiation pressure from each pair of counterpropagating beams. These radiation pressure effects cancel each other out, and the atom ultimately feels no net force at all. If, however, an atom is moving along one of the directions of the counter-propagating beam pairs, it will feel imbalanced radiation pressure. In the rest frame of the atom, the frequency of the beam propagating counter to the atom's movement will appear blueshifted to a frequency closer to the cooling transition resonant frequency, ω_0. This causes the atom to experience a faster rate of absorption from this particular beam, leading to more radiation pressure from this beam, which ultimately slows down the atom. Faster atomic speeds result in more blueshifting and more radiation pressure force, so the molasses force takes the mathematical form of $F_{mol} \propto -v$. Thus, the molasses force behaves exactly like linear drag force from classical mechanics. Figure 2.1 gives visual aid into how the process works.

As a result of this process, the atom absorbs a photon and reaches the excited state. After a brief amount of time, the atom will spontaneously emit the photon and drop back to the lower state. Spontaneous emission causes the atom to have a random velocity afterwards, and if the atom moves in the direction of a counter-propagating pair again, the same absorption/emission process will occur again. The overall idea behind this method is that if there are enough atoms at the center of the beams constantly reabsorbing/reemitting photons and picking up new velocities, then over time the thermal velocity of the collection of atoms will drop to nearly zero, signaling successful cooling.

Optical molasses is naturally limited by the decay rate of the upper energy level. This is called the Doppler limit, and in order to cool atoms below the Doppler limit and make things

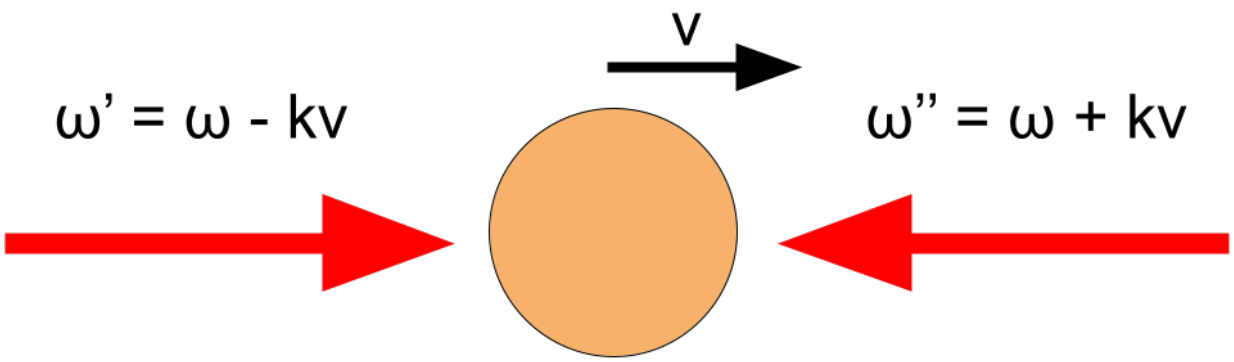

Figure 2.1: Illustration of an atom in the path of two counter-propagating lasers (not to scale). The atom has a resonant frequency of ω_0, and the lasers run at a frequency of ω, where $\omega < \omega_0$. The atom is moving to the right with velocity v. This movement causes the beams to be Doppler-shifted in the rest frame of the atom; the frequency of the left beam is redshifted and decreases to $\omega' = \omega - kv$, while the frequency of the right beam is blueshifted and increases to $\omega'' = \omega + kv$. As a result of these Dopper shifts, the atom will feel increased radiation pressure from the right beam and decreased radiation pressure from the left beam. The resulting radiation pressure force acts in the opposite direction of the velocity. Furthermore, the atom will absorb a photon from the right beam, then emit the photon at a later time and pick up a random recoil velocity. In an optical molasses setup, there are three pairs of counter-propagating beams along orthogonal directions, and this process of absorption and emission repeats until the RMS velocity of the atoms drops to nearly zero.

like BECs, additional cooling mechanisms such as RF knives and evaporative cooling need to be implemented. The Doppler limit temperature is given by the following expression:

$$k_B T_D = \frac{\hbar \Gamma}{2} \tag{2.1.1}$$

Here, k_B is Boltzmann's constant, T_D is the Doppler limit temperature, $\hbar$ is the reduced Planck's constant, and Γ is the decay rate of the excited state. In order to reach this temperature, the detuning of the cooling lasers from resonance must be $\delta = -\frac{\Gamma}{2}$. As an example, for a rubidium-85 optical molasses operating on the $5S_{1/2} \rightarrow 5P_{3/2}$ transition, $\Gamma = 2\pi \times 6.0666$ MHz, so the Doppler limit temperature in this case is $T_D \approx 150$ μK.

Drag force from optical molasses can slow atoms down, but it cannot trap them. The trapping capabilities of a MOT come from the addition of the quadrupole magnetic field, usually supplied by two current coils in an anti-Helmholtz configuration. It is a common misconception to think that the atoms are trapped in place by magnetic force, but in reality the applied magnetic field is too weak to confine the atoms. What the magnetic field does, though, is split the cooling transition through the Zeeman effect. For example, in the $S \rightarrow P$ cooling transition for alkali metals, the upper level splits into three for the three values of m_ℓ $(0, \pm 1)$. The Zeeman effect and induced splitting become stronger as atoms move further away from from the field zero and into regions of stronger magnetic field.

While the magnetic quadrupole field and resulting Zeeman splitting establish the conditions for trapping, the actual trapping itself is done by the cooling beams. To do this, the beams are circularly polarized in a specific manner before being sent into the trap center. This beam polarization, along with the presence of the magnetic field, is the main difference between a MOT and pure optical molasses, where the beam polarization is unimportant. The light polarization, along with the line splitting, results in the cooling beams only cycling on one of the Zeeman sublevels. This in turn causes the beams to exert radiative pressure of the atoms, pushing them back into the trap center. It is this radiative pressure that provides the trapping mechanism. The exact polarizations of the beams, σ^+ and σ^-, depends on the polarity of the quadrupole field. Regardless of the field polarity, the general rule is that the beam pair along the magnetic field's axis of symmetry has one helicity, while the two beam pairs along the radial direction of the field have the other helicity. Figure 2.2 shows an example configuration of a MOT, as well as an energy level diagram with cycling transitions.

The overall force that a MOT applies to an atom takes into account both the molasses cooling effect and the Zeeman-induced radiation pressure. F_{MOT} follows the approximate form:

$$F_{MOT} \simeq -2\frac{\partial F}{\partial \omega} k v - 2\frac{\partial F}{\partial \omega} \beta z \tag{2.1.2}$$

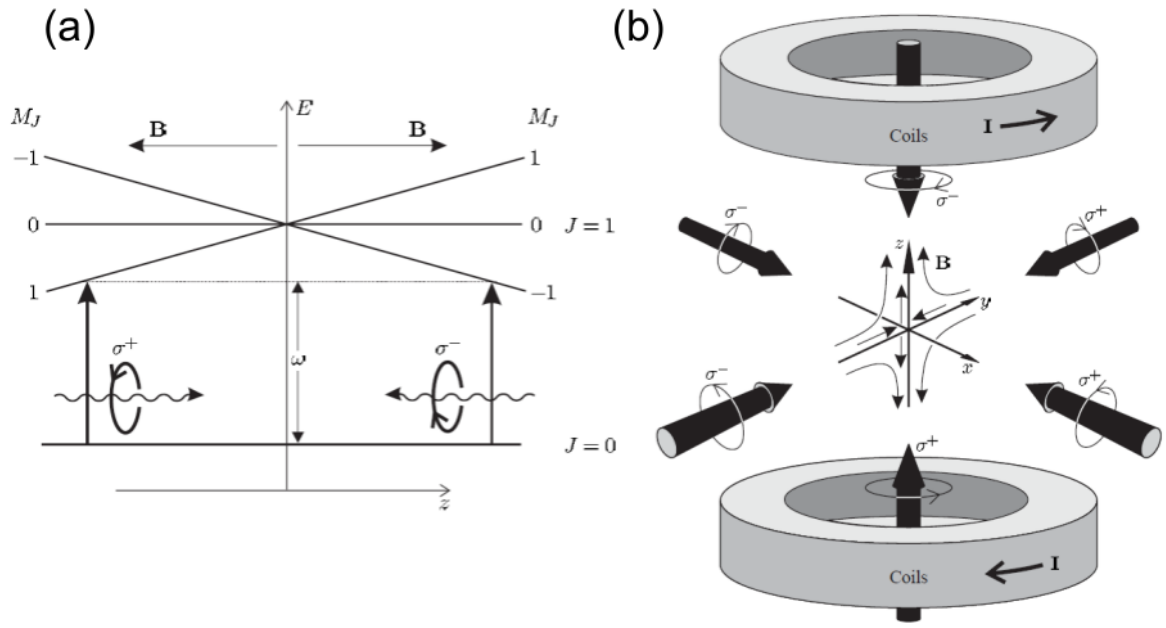

Figure 2.2: (a) Energy level diagram of a MOT cooling transition with Zeeman-induced line splitting. The Zeeman splitting and circular polarization of the light means that only certain magnetic sublevels are driven, which creates the radiation pressure force. (b) Illustration of a MOT setup, complete with current coils, the resulting quadrupole field, and circuplarly polarized beams. The two beams along the magnetic field axis of symmetry have one helicity, while the remaining four beams have the other helicity. Image credit: Foot, *Atomic Physics*, pg. 192 [1]

The first force term is the molasses cooling effect, and the second term is the radiative pressure from the Zeeman effect. Here, z and v are position and velocity coordinates along a beam propagation direction, and $z = 0$ at the center of the trap. $\frac{\partial F}{\partial \omega}$ represents the effect of photon frequency on the resultant force; in this context, it can simply be treated as a constant. k is the wave number of the photon, and β is the Zeeman splitting per displacement from the trap center, defined as

$$\beta = \frac{g\mu_B}{\hbar}\frac{dB}{dz} \tag{2.1.3}$$

Here, g is the g-factor of the electron, μ_B is the Bohr magneton, $\hbar$ is Planck's constant, and $\frac{dB}{dz}$ is the magnetic field gradient along z.

The form of F_{MOT} in Eq. 2.1.2 shows exactly how the molasses component and Zeeman component differ from each other dynamically. The molasses component, as mentioned earlier, behaves like linear drag force in classical mechanics and causes the atom to slow down. The Zeeman component, meanwhile, is proportional to $-z$, so it is ultimately a restoring force like spring force. Between the two, only the Zeeman force is capable of confining atoms spatially.

These calculations are based on the assumption that the cooling beams are collimated and longitudinally symmetric. While this is the case for the classic MOT design, this is no longer true in Chapter 6, where I discuss the physics of making a MOT with diverging beams.

2.1.2 Rubidium MOT

Rubidium, an alkali metal, is the most popular choice of atom for trapping and cooling. It is typically cooled on the $5S_{1/2} \rightarrow 5P_{3/2}$ (D2) cycling transition, much like other alkali metals. There is an added layer of complexity, though, that results from rubidium's nuclear spin. Rubidium has two stable isotopes, 85 and 87. Technically, rubidium-87 is radioactive, but with a half-life of about 40 billion years, it is stable as far as humans are concerned. Both of these isotopes have non-zero nuclear spins: $I = \frac{5}{2}$ for rubidium-85, and $I = \frac{3}{2}$ for rubidium-87. Thus, for P-state atoms ($J = \frac{3}{2}$), rubidium-85 can have hyperfine quantum numbers of $F' = 1, 2, 3, 4$, and rubidium-87 can have hyperfine quantum numbers of $F' = 0, 1, 2, 3$.

These hyperfine states can cause problems when cooling rubidium with only one laser. When cooling rubidium-85(87), the cooling laser, or main laser, is usually tuned to cool on the $5S_{1/2}, F = 3(2) \rightarrow 5P_{3/2}, F' = 4(3)$ cycling transition. Most of the time, the atom returns to the $F = 3(2)$ hyperfine state after undergoing spontaneous emission, and the cooling process begins anew. Sometimes, though, atoms will end up in the $F = 2(1)$ hyperfine state after spontaneous emission. This happens because the different hyperfine energy levels are fairly close to each other. Should this occur, the atom will become insensitive to the laser; this is often referred to

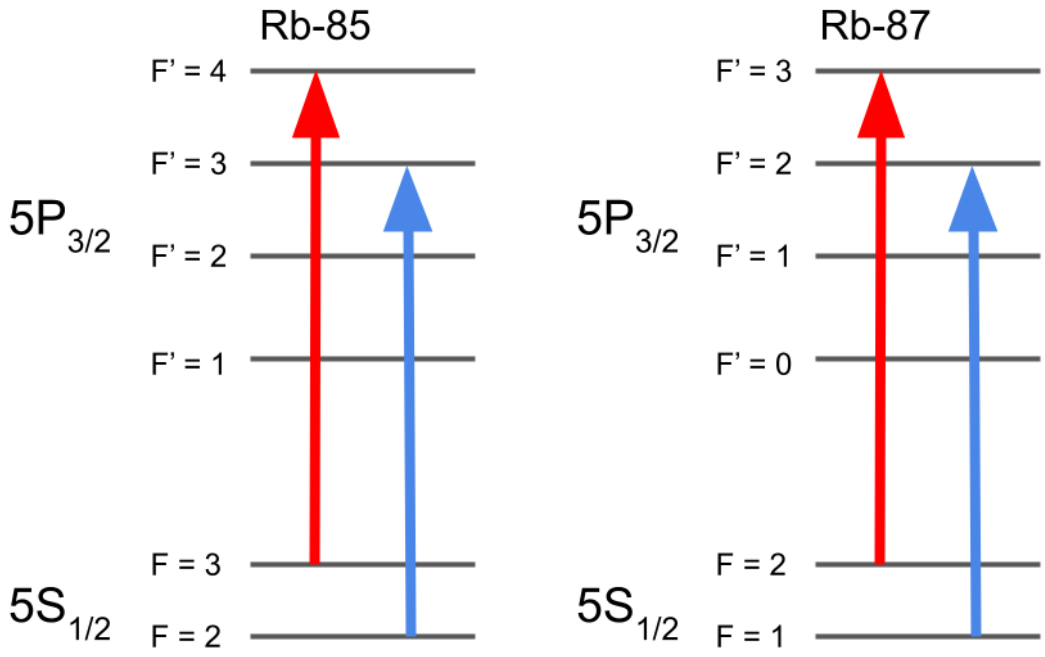

Figure 2.3: Hyperfine level diagrams for the $5S_{1/2} \rightarrow 5P_{3/2}$ MOT cooling transition in both stable isotopes of rubidium. The red arrows are the master cooling transition, while the blue arrows are the repumper transition.

as the atom falling into a "dark state." If, over time, enough atoms fall into this dark state, the MOT will cease to function properly. This problem can be remedied by incorporating a second laser into the MOT setup called the "repumper". The repumper's sole purpose is to drive the $5S_{1/2}, F = 2(1) \rightarrow 5P_{3/2}, F' = 3(2)$ transition, thereby bringing the atoms out of the dark state. The repumper is run at a lower power than the cooling laser and does not significantly contribute to the cooling itself. Figure 2.3 shows hyperfine-structure level diagrams for rubidium 85 and 87 with the master and repumper transitions.

As an aside, in experimental setups where a MOT is exposed to a high magnetic field, the repumper is no longer necessary [67, 68]. At high magnetic field strengths, the Zeeman effect separates the hyperfine states to the point where a rubidium-85(87) atom will always remain in the $5S_{1/2}, F = 3(2) \rightarrow 5P_{3/2}, F' = 4(3)$ cycle and will never fall into the $F = 2(1)$ dark state.

2.2 Rydberg Atoms

Rydberg atoms are atoms that have been excited to high-energy states, or high principal quantum number n. The minimum quantum number for Rydberg states is $n \sim 10$. Many physical properties of atoms, such as radius and electric dipole moment, scale with n raised to a power, so Rydberg-state atoms have highly exaggerated physical characteristics compared to their low-lying

counterparts. Table 2.1 features a list of several atomic traits, along with their n-scaling.

Property	n Scaling
Binding energy	n^{-2}
Energy between adjacent n states	n^{-3}
Orbital radius	n^2
Geometric cross section	n^4
Dipole moment	n^2
Polarizability	n^7
Radiative lifetime	n^3
Fine-structure interval	n^3

Table 2.1: A list of atomic traits, and how they scale with principal quantum number n. Source: Gallagher, *Rydberg Atoms*, pg. 25 [2].

There are several properties in Table 2.1 that are particularly important for PI and plasma studies. The n^{-2} scaling of the binding energy, which can be derived from both the Bohr model and from solutions to the radial Schrödinger equation, states that the excited electrons in Rydberg atoms are loosely bound to the atom. Therefore, Rydberg atoms can be photoionized by a wide spectrum of photons. As I will discuss further in Chapter 5, this quality makes Rydberg atoms better than low-lying atoms for pure PI studies. The wide PI spectrum makes it easier to find wavelength-specific phenomena such as Cooper minima and shape resonances. Additionally, Rydberg atoms are easily photoionized by visible and near-infrared (NIR) light, which are accessible to most labs. In contrast, atoms in the ground state require photons with UVC wavelengths or shorter, which are far less readily available. The most well-known example of this is the photoionization of ground-state hydrogen. This process requires a minimum photon energy of 13.6 eV, which corresponds to a wavelength of 91 nm.

The dipole moment and polarizability of Rydberg atoms are foundational for atom-based field sensing. The n^2 and n^7 scalings of these respective properties indicate that Rydberg atoms are highly sensitive to external electric fields. This means that when a Rydberg-EIT signal is exposed to an external electric field, the signal is significantly perturbed by the Stark effect from said field. One can then measure the amount of Stark shift/splitting and use that to determine the strength of the external field. This technique can be used to measure a variety of electric fields, including fields in plasmas.

In Rydberg-EIT field measurements, the dipole moment is relevant for measuring the Autler-Townes effect, which is when the frequency of the external AC field is close to an atomic resonance. In Rydberg atoms, applied RF and microwave fields can drive Rydberg-Rydberg transitions, leading to Autler-Townes splitting of the Rydberg-EIT signal. The dipole moment is essential for determining the magnitude of the applied field from the measured A-T splitting. The polarizability, meanwhile, is the relevant quantity for off-resonant AC fields and for all DC fields, including plasma electric fields. More on this will be discussed in Chapter 7.

CHAPTER 3

Plasma Physics Background

Plasma physics is a vast field, and this chapter will focus on the aspects most relevant to cold tabletop plasmas in AMO laboratories. More complete descriptions of plasma physics can be found in books such as *Introduction to Plasma Physics* by Goldston and Rutherford [69], *High-Energy-Density Physics* by Drake [51] and *Introduction to Plasma Physics and Controlled Fusion* by Chen [70].

3.1 Basic Plasma Parameters

3.1.1 Debye Length

Plasma is often described qualitatively as an ionized, gaseous substance. While this definition is adequate for differentiating plasma from other states of matter, it is not rigorous; not all ion clusters can be considered plasmas. The rigorous, quantitative definition of plasma is given by a physical parameter called the Debye length, λ_D. The general definition of the Debye length for a mixed plasma is:

$$\lambda_D = \sqrt{\frac{\varepsilon_0 k_B / q_e^2}{n_e/T_e + \Sigma_j z_j^2 n_j / T_i}} \tag{3.1.1}$$

Here, ε_0 is the permittivity of free space and k_B is the Boltzmann constant. q_e, n_e, and T_e are electron charge, number density, and temperature. The summation term is the contribution from ions: z_j and n_j are the atomic number and number density of the j-th ion, and T_i is the ion temperature, which is assumed to be the same for all ions. The Debye length is a measure of how far a single charge carrier's electrostatic effect persists. Whether a specific electron/ion cluster is a plasma or not depends on how the Debye length compares to the size of the cluster itself. If the

Debye length is shorter than the smallest physical dimension of the cluster, then the cluster can be considered a plasma.

In mixed plasmas with both electrons and ions, the electrons typically have a much higher temperature than the ions. Looking at Eq. 3.1.1, it is fair to assume that the higher electron temperature causes the electron component to go to zero and become negligible. In a somewhat counterintuitive twist, though, it is the ion term that is usually dropped from Eq. 3.1.1, despite having a lower temperature. The rationale here is that because the electrons have a higher temperature, they have a faster thermal speed and ultimately govern the plasma dynamics moreso than the ions do. Therefore, the ion term is often dropped. Without the ion term, the Debye length becomes a single-component expression and simplifies to:

$$\lambda_{D,\text{neutral}} = \sqrt{\frac{\varepsilon_0 k_B T_e}{n_e q_e^2}} \tag{3.1.2}$$

Of course, for pure ion plasmas without electrons, the electron term in Eq. 3.1.1 is dropped completely. For a non-neutral, single-ion plasma like the one discussed in Chapter 4, the Debye length is:

$$\lambda_{D,\text{ionic}} = \sqrt{\frac{\varepsilon_0 k_B T_i}{n_i q_i^2}} \tag{3.1.3}$$

In the context of atomic physics, plasmas are usually either neutral (electrons and a single ionic species) or non-neutral (ions only), so Eq. 3.1.1 is adjusted accordingly. One-component and two-component plasmas will be discussed in greater detail in Sec. 3.2. λ_D shortens at higher densities and lengthens at higher temperatures, so cold, high-density conditions are favorable for plasma formation.

3.1.2 Plasma Frequency

The plasma frequency is the other fundamental physical parameter of any given plasma. Going back to the earlier discussion of plasmas versus charged gaseous clusters, another physical characteristic that differentiates plasma from charged clusters is the presence of collective effects and/or motions beyond simple binary collisions. One of the most important examples of this is plasma oscillations. Plasma oscillations, as the name suggests, are oscillations in the density, caused by the plasma's inherent electrical conductivity. There are many different types of plasma oscillations, each corresponding to different physical situations. Some oscillations are specifically for the electron component, while others are specifically for the ion component. Similarly, oscillations can be divided into unmagnetized versus magnetized effects. To give a few examples,

Langmuir waves are longitudal electron density waves in unmagnetized plasmas, and ion acoustic oscillations are ion acoustic waves in unmagnetized plasmas; these waves are equivalent to sound waves in their respective media.

While a comprehensive discussion on all possible plasma oscillations is outside the scope of this thesis, the physical parameter that relates all oscillations to each other is the plasma frequency. Similar to Debye length, the plasma frequency in neutral and non-neutral plasmas differs based on the thermodynamics of the different components. In a neutral plasma, the electron component governs the overall plasma dynamics and timescales. Therefore, the plasma frequency for neutral plasmas solely depends on the electron component. The expression for electron plasma frequency is given below:

$$\omega_{p,e} = \sqrt{\frac{n_e q_e^2}{\varepsilon_0 m_e}} \tag{3.1.4}$$

The plasma frequency here is given in units of angular frequency, and it can be converted to Hz by dividing Eq. 3.1.4 by 2π. Similarly, in a one-component ion plasma, the electron quantities in Eq. 3.1.4 are replaced with ion quantities. The plasma frequency is found in almost all oscillation dispersion relations, and it can also be inverted, giving a value with units of time. This is the particle interaction time, and it is especially important for freely-expanding plasmas. As a plasma expands, its density drops, causing the plasma frequency to decrease and the interaction time to increase. If the interaction time becomes greater than the lifetime of the plasma, then from that point on plasma particles are no longer colliding or interacting with each other. It is at this point that the plasma is said to be "collisionally decoupled" and is now just ballistically expanding.

To conclude this discussion on plasma frequency, I will give the dispersion relations for a few examples of plasma oscillations. For Langmuir waves, the dispersion relation is:

$$\omega^2 = \omega_p^2 + 3k^2 v_{th}^2 \tag{3.1.5}$$

k here is the wave number, and v_{th} is the thermal velocity of the electrons. For ion acoustic waves, the dispersion relation is:

$$\omega^2 = k^2 \frac{Z k_B T_e + 3 k_B T_i}{m_i} \tag{3.1.6}$$

k_B here is the Boltzmann constant. Finally, because plasmas are conductive, they can maintain electromagnetic waves. The dispersion relation for electromagnetic waves in a plasma is:

$$\omega^2 = \omega_p^2 + k^2c^2 \tag{3.1.7}$$

3.2 Neutral vs. Non-Neutral Plasmas

Plasmas generated in atomic physics laboratories are usually either non-neutral and one-component (ions only) or neutral and two-component (ions and electrons). The type of plasma that is created is determined in part by the wavelength of the PI laser. If the PI laser emits photons with energy greater than the minimum PI energy of the atom, then the excess energy is imparted to the free electron as kinetic energy. Mathematically, this is given by the following expression:

$$K = \frac{hc}{\lambda} - \Phi \tag{3.2.1}$$

Here, K is the electron kinetic energy post-ionization, h is Planck's constant, c is the speed of light, λ is the wavelength of the PI laser, and Φ is the minimum photoionization energy of the atom, also known as the work function. As the energy of the ionizing photon increases, so to does the electron's velocity. The electron velocity is given from simple classical mechanics:

$$v_e = \sqrt{\frac{2K}{m_e}} \tag{3.2.2}$$

The corresponding ion recoil velocity is then determined through conservation of momentum:

$$m_i v_i = m_e v_e \Rightarrow v_i = \frac{m_e}{m_i} v_e \tag{3.2.3}$$

Because the ions are much more massive than the electrons, the ion velocity is negigible, and the ions are assumed to be motionless. Plasmas that are formed with higher-energy photons are more likely to be one-component plasmas because the electrons are traveling at higher speeds and are more likely to exit the plasmas. On the other hand, plasmas that are formed with lasers running at just above threshold are almost certainly going to be two-component plasmas, as the electrons have very little recoil velocity and cannot leave the plasma.

The PI laser wavelength (and subsequent electron recoil velocity) is one major factor in determining whether a photoionized plasma will be one-component or two-component. The other factor is the density of the resulting ion cloud immediately after photoionization. These ions produce a positive electric potential that increases in strength at higher densities and ion numbers. Just like with gravitational potentials, these electrostatic potentials have escape velocities that are dependent on the overall strength of the potential. Thus, it is possible to have a scenario where the

photon energy of the PI laser is well above threshold, but the resulting plasma is two-component because the ion electric potential is strong enough to keep the electrons within the plasma.

3.3 Plasma Dynamics

3.3.1 Coupling Strength

The concept of plasma coupling strength was briefly discussed in Sec. 1.1 of Chapter 1. In this section, I will expand upon the material presented in Chapter 1 and provide more details on coupling strength.

The coupling strength of a plasma is an indicator of how a plasma's electrostatic energy compares to its thermal energy. It is described quantitatively by the Coulomb coupling parameter, Γ, which is defined below:

$$\Gamma = \frac{q^2/(4\pi\varepsilon_0 r_{WS})}{k_B T} \tag{3.3.1}$$

Note that this is the same equation as Eq. 1.1.1. Here, q is the plasma particle charge, ε_0 is the permittivity of free space, k_B is the Boltzmann constant, T is the temperature, and r_{WS} is the Wigner-Seitz radius, which is given by Eq. 1.1.2. This equation gives the ratio of the plasma's electrostatic energy to its thermal energy (it is worth noting that this equation omits the degree of freedom factor typically included with thermal energy; for example, the thermal energy of a three-dimensional system of particles without rovibrational degrees of freedom is actually $\frac{3}{2}k_B T$, but the $\frac{3}{2}$ factor is never included in Γ.) A plasma with $\Gamma \gtrsim 1$ is considered strongly-coupled, whereas a plasma with $\Gamma < 1$ is considered weakly-coupled. It is worth noting here that in a neutral plasma, the electron component is usually at a higher temperature and is not as strongly coupled as the ion component. In most contexts, people refer to Γ_{ion} when talking about the coupling strength of neutral plasmas.

When a plasma is cold enough or dense enough to be in the strong-coupling regime, the particles begin to interact with each other electrostatically, leading to interesting results. Microfield interactions between particles of like charge can lead to pair correlations. Specifically, pair correlation calculations can reveal regions of anti-correlation around a plasma particle. These anti-correlation regions signify the typical spacing between plasma particles, and the regions become larger and more pronounced at higher Γ values due to increased electrostatic repulsion [71]. The shape of the anti-correlation region also depends greatly on the initial plasma distribution and expansion behavior; Sec. 4.4 contains experimental findings on anisotropic pair correlations in cylindrical plasmas.

A phenomenon called Wigner crystallization emerges at extremely high values of Γ ($\Gamma \sim 150$). At this degree of coupling strength, the microfield interactions between like-charged particles becomes so strong that the particles become "frozen" in place in a spatially periodic pattern. Pair correlations of plasmas that have reached Wigner crystallization show periodic regions of anti-correlation and enhanced correlation. Wigner crystallization is difficult to obtain, even in AMO laboratory settings where strongly-coupled plasmas are relatively easy to create. The scaling law between coupling strength and density is $\Gamma \propto n_V^{1/3}$, so coupling strength grows quite slowly with density. Coupling strength and temperature have a more favorable scaling law ($\Gamma \propto T^{-1}$), but there are certain heating processes in cold plasmas that hinder Wigner crystallization (these processes will be described in detail in the next section). The most pertinent and most obvious issue, though, is that it is difficult for Wigner crystallization to form in freely-expanding plasmas. This can be remedied by containing the plasma in one of the wide variety of ion traps available (see Sec. 1.2). Ion MOTs for species such as Ca^+ and Sr^+ particularly excel here, as they have the ability to cool the plasmas and counteract some of the heating effects.

3.3.2 Time-Evolved Behavior

Plasmas created in free space are inherently unstable systems due to repulsive electrostatic charges. Non-neutral plasmas expand more rapidly than neutral plasmas of equal ion density due to mutual repulsion among every single particle. Neutral plasmas are able to somewhat suppress their expansion because of their net charge neutrality, but they too blow up eventually due to electron pressure. As plasmas expand, they are subject to both structural and thermodynamic changes. This section will be dedicated to some of the time-evolving processes that plasmas can undergo.

One structural phenomenon that can occur is the formation of shock shells, also commonly called shock fronts. These are defined by a drastic redistribution of density. As the plasma expands, particles begin to pile up at the edge of the plasma's profile, leading to high-density outer fringes and low-density wakes. The "shock" part of the name comes from the fact that these fringes typically move faster than the speed of sound in the plasma. Shock shells cannot form in all plasmas; the initial density distribution must be some kind of non-uniform distribution with a higher-density core in order for shock shells to form in the first place [51]. Additionally, shock shells become less distinct in lower-density plasmas. Photoionized plasmas typically have initial density distributions that are Gaussian thanks to the Gaussian profiles of laser beams, making them well-suited for developing shock shells. Section 4.3 will discuss experimental findings of shock shells in cold rubidium plasmas.

Moving from structural to thermodynamic effects, photoionized plasmas can experience a variety of heating and cooling effects (some of the cooling effects relevant to expanding plasmas will be discussed in Sec. 4.3). One of these processes that is particularly important is disorder-

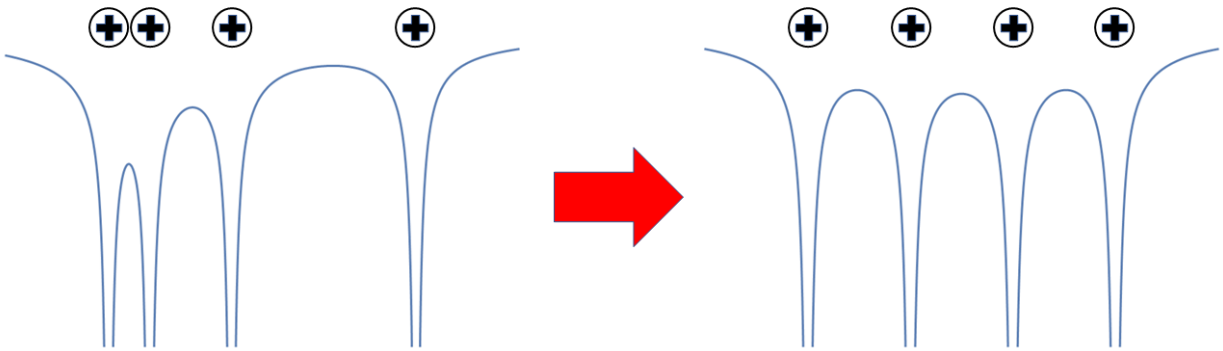

Figure 3.1: Illustration of ions undergoing disorder-induced heating. The two panels feature four ions overtop of their combined electrostatic potential. In the left panel, the ions are arranged in a disordered manner, and the resulting electrostatic potential is unstable. In the right panel, the ions have rearranged into an ordered configuration with a stable potential. This process is exothermic, and the plasma is heated as a result.

induced heating (DIH). DIH is important because it occurs in varying degrees in all photoionized plasmas, be they neutral or non-neutral, or freely expanding or trapped. It is also particularly troublesome because it can significantly heat the plasma and ruin the coupling strength. DIH is ultimately a consequence of photoionization, which is a process that is both inherently random and not 100% efficient. While the overall density distribution of the plasma will follow the Gaussian distribution of the excitation lasers, the spatial orientation of the plasma ions will be random within the excitation region. This random placement of ions can be seen in pair correlations of newly-formed plasmas; immediately after PI, pair correlation calculations show no signs of enhanced correlation or anti-correlation. After the plasma has been formed, the ion microfields will cause the plasma to rearrange from its random, disordered distribution to an ordered distribution. This process ends up heating the plasma, hence the name "disorder-induced heating." Figure 3.1 gives insight into how DIH works.

In addition to DIH, neutral plasmas can experience another heating process called three-body recombination (TBR). As the name suggests, TBR involves the interaction of three particles: specifically, two electrons and an ion. The process begins with the three particles colliding with each other at the same time. Upon collision, the ion will absorb one of the electrons and become a neutral atom again. After one of the electrons has been absorbed, the remaining electron and

resultant atom scatter off of each other. The process is exothermic, and the electron and atom will each carry kinetic energy after the collision.

The mathematics of TBR were formalized in 1969 by Mansbach and Keck [72]. In their formalism, the process is described by the phenomenological rate equation:

$$\frac{\partial[A]}{\partial t} = a[e][A^+] - aK_e[A] \tag{3.3.2}$$

Square brackets indicate density of whatever is inside; A, e, and A^+ are neutral atoms, electrons, and ions. K_e is the Saha equilibrium constant. Overall, the expression describes the time-evolution of the neutral atom density, and a is the rate of steady-state recombination-rate constant. Mansbach and Keck found a to be:

$$a = 2.0 \times 10^{-27}[e][k_B T(\text{eV})]^{-9/2} \text{ cm}^3 \text{ s}^{-1} \tag{3.3.3}$$

If TBR happens on a large scale with many ions and electrons, then the neutral plasma will not only lose ions, but it will also become heated. TBR is not an issue for one-component ionic plasmas, as there are no electrons to interact with.

CHAPTER 4

Coulomb Explosion of Cold Non-Neutral Plasmas

The work discussed in this chapter consists of material published in Ref. [73], as well as unpublished material presented in Ref. [74].

As mentioned in Chapters 1 and 3, non-neutral plasmas develop features such as shock shells and particle correlations as they expand. For non-neutral plasmas created from cold atom sources, these expansion dynamics play out on the order of a few microseconds. This time scale means that, by using ion imaging, these cold plasma clouds can be imaged over the duration of their expansion. With this technique, I am able to create stop motion clips of expanding plasmas and observe shock shells and correlations through data analysis.

In this chapter, I present an experimental and theoretical study of the expansion of a cold, cylindrically-shaped plasma of rubidium atoms. The experimental tool used to probe this plasma is the tip ionization probe (TIP) ion imaging system, which has been discussed in prior group member theses [75–77] and has been used in the past to investigate Rydberg blockade radii [6], van der Waals interactions [7], and dipole-dipole interactions [8]. Ion imaging has also been used by other groups to study ionization spectra [9, 10], tunnel ionization rates [11], and quantum gases [12].

4.1 Experimental Setup

4.1.1 TIP-2 Ion Imaging Chamber

The plasma expansion experiment is conducted in the TIP-2 vacuum chamber, whose design is described in detail in [78]. This chamber is named TIP-2 because it contains the second iteration of the TIP ion imaging system from our research group. This chamber was assembled a few years after TIP-1 was built, and it was originally designed for BEC studies. Although there are notable

design differences between the two chambers, both have the same basic function of imaging ions sourced from cold atoms trapped in MOTs.

The key component of the TIP imaging system in both chambers is a needle-shaped, beryllium-copper electrode which is positioned ~ 2 mm away from the ions of interest. To take an image, a high voltage step pulse with a 90% rise time of 76 ns is applied to the electrode, producing a divergent strong electric field. The ions are accelerated by this electric field through ion optics towards an MCP. Upon impact on the MCP, the ions produce bright spots on a phosphor screen which give the two-dimensional plasma ion positions at the time of extraction. The MCP detection efficiency is 30-50%, according to manufacturer's specifications. A CCD camera takes a picture of the phosphor screen for each experimental cycle. The magnification factor of the imaging setup can be varied by adjusting the distance between the TIP and the excitation region and can be calibrated by translating the excitation region by known distances. The TIP-2 chamber particularly excels over the TIP-1 chamber for magnification adjustments because the TIP-2's needle electrode is mounted onto an actuator. The actuator can move the needle electrode closer or farther away from the ions, allowing for quick adjustment of the magnification. Meanwhile, the needle electrode in TIP-1 is at a fixed position, so adjusting the magnification in this system involves moving the ions, a more difficult task than simply moving the needle.

As a quick aside on semantics, TIP stands for "tip *ionization* probe" because this imaging setup was originally used for imaging systems of Rydberg atoms. When the needle electrode was engaged, the resulting electric field would ionize Rydberg atoms first, and then accelerate them toward the MCP. With plasmas, the particles are already ionized, so the needle electric field simply accelerates the ions to the MCP with no further ionization. Regardless, the name "TIP" has stuck.

The TIP-2 chamber features a two-MOT setup: the primary MOT that contains a reservoir of trapped rubidium atoms, and a secondary MOT from which the plasma is formed. The MOTs in this chamber trap and cool rubidium-87, in part because rubidium-87 is better suited for BEC experiments (in plasma experiments, there is no functional difference between using either rubidium-87 or rubidium-85). The MOTs trap and cool rubidium-87 atoms on the $5^2S_{1/2} \rightarrow 5^2P_{3/2}$ transition ($\sim$780 nm). Because of rubidium's hyperfine structure, the MOT requires two lasers that drive two different hyperfine transitions. Otherwise, atoms will fall into dark states and become insensitive to the cooling transition, and the MOT will eventually fail. To that end, the setup contains two homebuilt distributed Bragg reflector (DBR) lasers that run at 780 nm. The master laser, the more powerful of the two, drives the $F = 2 \rightarrow F' = 3$ hyperfine transition, while the repumper laser drives the $F = 1 \rightarrow F' = 2$ hyperfine transition. The lasers are locked onto these hyperfine transitions with PID circuits and reference lines from saturated absorption spectroscopy setups.

The master laser in this setup is further split into two additional branches, known as the pusher beam and the probe beam. The pusher laser, which is pulsed at 10 Hz with duty cycle of 10% by an acousto-optic modulator (AOM), is responsible for moving atoms from the primary MOT to the secondary MOT. It has a peak power of 1.5 mW, with a 1 mm FWHM beam diameter. The probe beam, on the other hand, is a continuous wave (cw) beam that is sent through the secondary MOT and into a CCD camera. The probe beam can be used to measure both the atom number and the density of the secondary MOT cloud via a technique known as "absorption imaging," or "shadow imaging." Basically, if the intensity of the probe beam is on the order of an I_{sat} or weaker, then one can measure the absorption of the beam by the MOT cloud and consequently determine the atom number/density. When the pusher laser is at maximum power, the secondary MOT is able to trap clouds of up to $\sim 10^7$ rubidium-87 atoms at densities of up to $\sim 4 \times 10^{10}$ cm^{-3}.

4.1.2 Plasma Formation and Experimental Timing

The plasma is formed from atoms trapped in the secondary MOT using a two-step photoionization process. This requires two additional lasers, separate from the lasers used to create the MOTs. The first laser, a diode laser, runs at the same wavelength as the master MOT laser (780 nm, $5^2S_{1/2} \rightarrow 5^2P_{3/2}, F = 2 \rightarrow F' = 3$) and is referred to as the lower excitation laser. This laser has the narrower beam profile of the two, so it establishes the shape of the plasma. Additionally, by bringing the atoms to an excited state, this beam lowers the threshold photoionization energy of the atoms from 296.8 nm^{-1} to 479.1 nm^{-1}.

The second laser is a Q-switched, frequency-tripled Nd:YAG laser. This laser produces 10 ns pulses of 335 nm ultraviolet (UV) light that ionize the excited atoms. The energy of the UV photons is well above threshold, and the liberated electrons have a kinetic energy of 0.9 eV. Computer simulations have verified that 0.9 eV is more than enough energy for the electrons to escape the ions' electric potential and leave the plasma, so this plasma is only composed of positive ions. The Nd:YAG laser is linearly polarized, which does affect the recoil velocity distribution of the plasma ions. However, subsequent computer simulations have shown that this makes no discernible difference in plasmas as high in density as the ones investigated here. Rather, this is only a significant effect in extremely low-density plasmas.

The entire process of plasma formation and ion imaging runs at a repetition rate of 10 Hz. Prior to plasma formation, the MOT light is turned off to prevent unwanted plasma outside the intended initial volume. The MOT magnetic field is left on because it does not have a significant effect on the experiment. A fraction of the cold atoms is driven by an 18 μs long pulse of the lower excitation laser to the $5P_{3/2}$ state. This laser beam has a Gaussian profile, with a waist w_0 of 9 microns, Rayleigh range of 326 microns, and central intensity of $105I_{sat}$. Five microseconds

after the 780-nm pulse is turned on, the $5P_{3/2}$ atoms are ionized with a pulse from the Nd:YAG laser. The initial temperature of the trapped atoms is roughly 100 μK, but the photoionization is accompanied with recoil heating to ≈44 mK, the initial temperature of our plasmas. The 355-nm pulse has a diameter of $\sim$ 2 mm, which is much larger than the size of the 780-nm beam. Hence, the initial geometry of the plasma column is determined by the 780-nm beam size and its central intensity, and the MOT size. Further, the fluence of the 355-nm pulse is $\lesssim 10^{16}$ cm^2, corresponding to a photoionization probability of the $5P_{3/2}$ atoms of $\lesssim 10$ percent, leading to up to several hundred ions in the initial plasma volume.

After the plasma has been formed, it is allowed to expand for a variable wait time τ. Once the wait time has elapsed, the ion imaging process begins. The TIP electrode is pulsed at a high voltage, the plasma ions are directed to the MCP, and the CCD camera records the resultant MCP bright spots. These single-ion resolving images represent the plasma ion distributions projected onto a plane transverse to the extraction trajectory, taken at time τ. Meanwhile, the spatial structure of the expanded plasma along the extraction trajectory is analyzed by measuring its time-of-flight distribution to the MCP using a multichannel scaler (SRS Model SR430).

In the following sections, I discuss the dynamics of non-neutral plasmas at two different densities. The density of the plasma was adjusted by adjusting the density and extent of the secondary MOT atom cloud. This in turn was adjusted by decreasing the power of the pusher laser with neutral-density (ND) filters. By weakening the power of the pusher laser with ND filters, I was able to get lower-density plasma. In these next sections, the "higher-density" plasma was made with no attenuation of the pusher beam, while the "lower-density" plasma was made with 0.2 and 0.3 ND filters in the path of the pusher. As I will demonstrate, different phenomena become more readily apparent at these different densities.

4.2 Computer Modeling

I use two approaches to model our system. In the molecular-dynamics simulations, I calculate trajectories of up to 1000 ions, accounting for all external and inter-particle Coulomb forces. A numerically generated map of the electrostatic potential along the ion-imaging path between the TIP and the MCP is implemented to model the ion imaging. While this approach is computationally expensive due to the need to account for binary forces, it has the strengths that (1) it is exact, limited in particle number only by computing power, that (2) the ion-extraction timing, the analysis of the ion images on the MCP, the ion time-of-flight data, and the pair correlation functions closely follow the experimental procedure, and that (3) valuable insights on macroscopic plasma parameters such as expansion velocity, density, temperature, coupling parameter etc. can be obtained on a grid of spatial domains as a function of time. The trajectory simulation

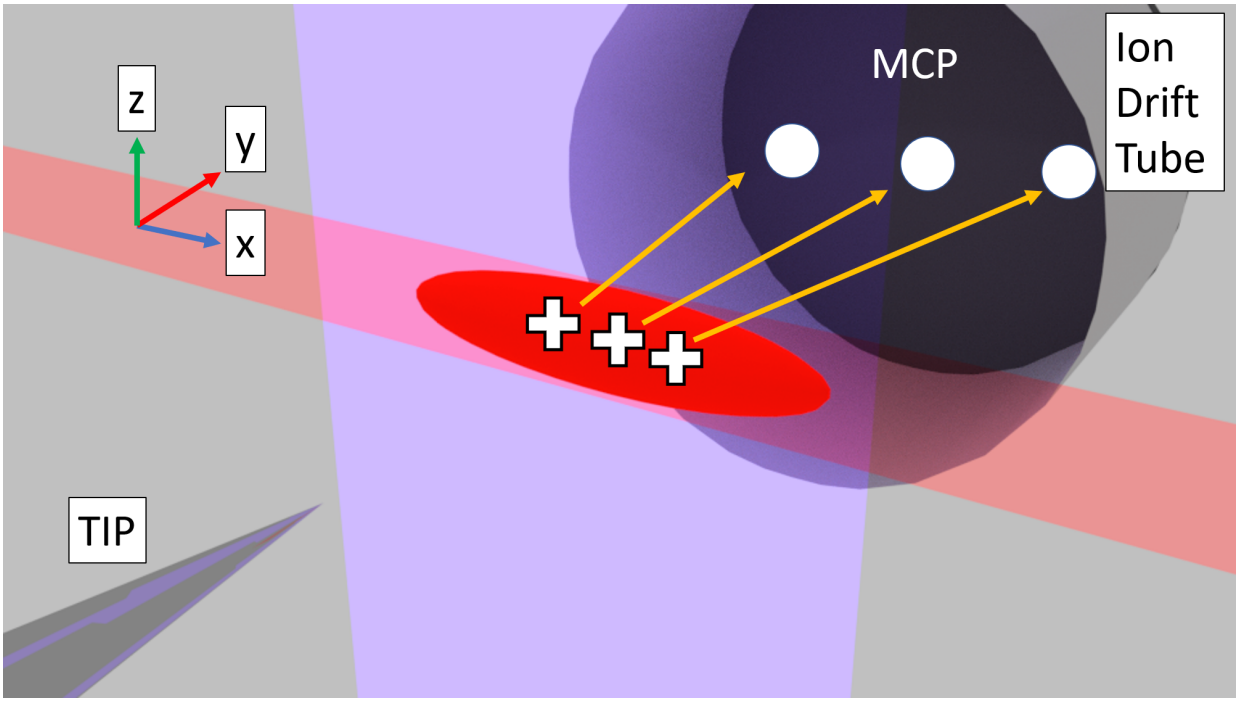

Figure 4.1: Rendering of experimental setup and process of plasma formation and imaging (not to scale). The positively charged rubidium ions are accelerated by the TIP electric field through the ion drift tube to the MCP, where they produce blips of a few-hundred ns decay time that are imaged with a camera.

is exact, because it accounts for microscopic and macroscopic electric fields (here, there are no significant magnetic fields), initial ion velocities and their angular distribution, initial spatial ion distributions, and Coulomb collisions during free expansion, ion extraction and imaging. The trajectory simulations are well-suited to model correlations and strong-coupling effects, in addition to modeling the overall expansion and imaging dynamics.

In the second approach, the plasma is modeled as a collision-less medium ("fluid") with a fixed charge/mass ratio that evolves under the influence of the macroscopic plasma electric field. In this collision-free, zero-temperature approach, the plasma is numerically treated as a discrete set of thin, inter-penetrable cylindrical or spherical shells. The initial photon-recoil-induced ion motion is ignored. The initial charges on the shells are given by the initial shell radii, shell thicknesses, and the initial charge distribution, which depends on ion excitation parameters and atom densities (chosen similar to those used in the experiment). The discrete radii of the shells are then propagated using Newton's equations. Gauss's law is employed to track the macroscopic electric field at the locations of the shells. The dynamical variables in this model are the shell radii and velocities, and the plasma electric field. This model ignores the effects of the microscopic fields and collisions; it can therefore not be used to model particle correlations. Also, in its present form the model does not allow for the inclusion of extraction and imaging electric fields that do not share the symmetry of the charge distribution. Nevertheless, the fluid model is numerically

inexpensive and suitable for the generation of qualitative plasma density maps versus time during the free-expansion time of the plasma. In the fluid model, shock fronts appear as singularities of the plasma density. Comparison between the fluid and the molecular-dynamics models then allows us to distinguish macroscopic from micro-field effects. A detailed analysis based on these models is given in Sec. 4.3.

4.3 Higher-Density Plasma Expansion

The experimental plasmas in this section are excited from a MOT containing 3.8×10^7 atoms at a density of 4.1×10^{11} atoms/cm^3, as determined by shadow imaging. The spatial profile of the initial ion clouds is given by the geometry described in Sec. 4.1 and the Appendix. The actual initial number of ions detected within the fixed field of view is 100 to 150, based on ion count and MCP detection efficiency. The initial central ion density is $n_c \approx 10^{10}$ cm^{-3}, as determined from ion number and excitation geometry. I observe this plasma for $\tau = 0$, 2, 4, 6, 8, and 10 μs of free expansion time. Ion-density images, time-of-flight data and pair correlation functions are averaged over 5000 experimental realizations. The linear image magnification factor for this data set is 54 times, with a diameter of the field of view on the MCP of 12 mm. Density and initial ion kinetic energy from photo-ionization recoil indicate an initial Debye length of $\lambda_D \sim 1$ μm, more than a factor of ten less than the short-axes initial diameter of the ion cloud, and an initial Coulomb coupling parameter of $\Gamma \approx 50$ (following Eq. 1.1.1).

4.3.1 Shock Shells

The most striking phenomenon occurring in these higher-density plasmas is the formation of shock shells. These shock shells form as a result of the non-uniform initial density, and they begin to appear several microseconds after the plasma is created. By the time the shells have formed, the plasma has expanded beyond the field-of-view of the ion imaging system, so the density spikes cannot be seen in the ion images alone. Fortunately, the shock shells along the extraction trajectory can be readily seen by observing the time-of-flight distribution of the plasma ions.

Figures 4.2 (a) and 4.2 (b) show the experimentally observed ion-count statistics and averaged images of plasma expansion. Starting from its initial cylindrical shape, seen at $\tau = 0$ μs, the plasma ions rapidly accelerate outward, leading to overall plasma expansion. At $\tau = 2$ μs, the plasma approximately fills the field of view along its initially short axis, with the average ion count still remaining approximately constant. For longer expansion times, the ions leave the field of view, and the average ion count monotonically decreases. Over the course of 10 μs of free

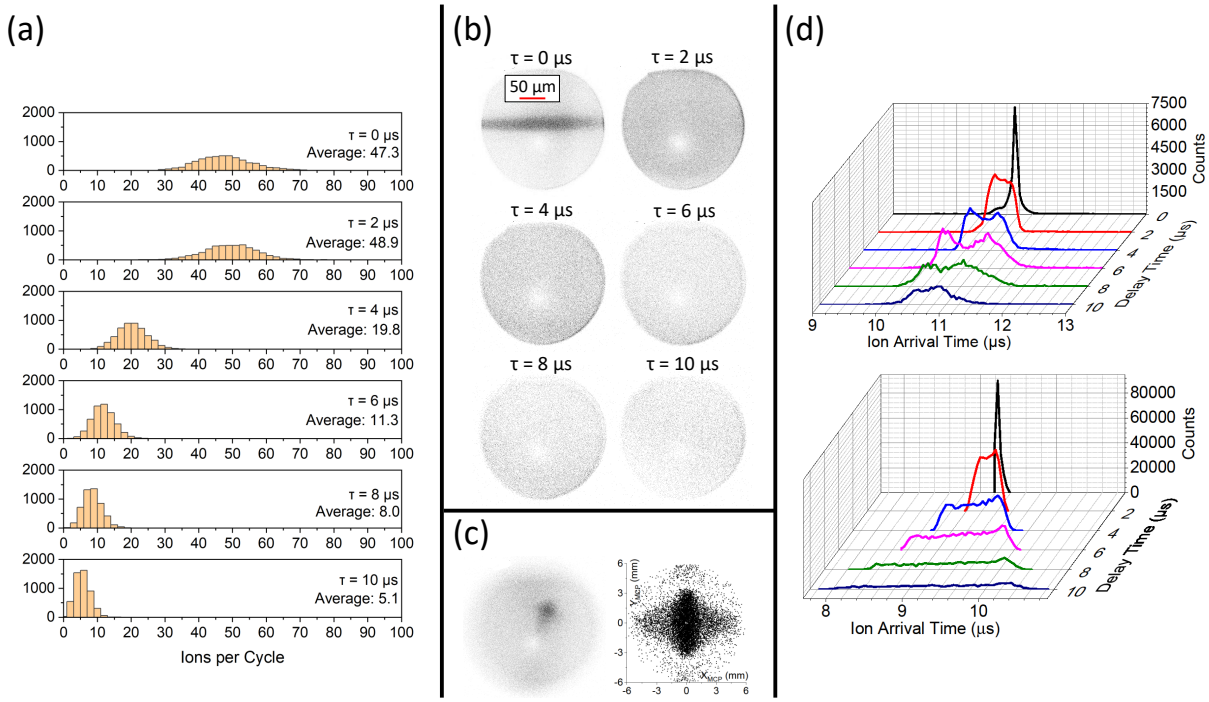

Figure 4.2: (a) Histograms of ion counts per cycle for the indicated expansion times τ . (b) Averaged pictures of the plasma images on the MCP plane for the indicated expansion times. The distance scale in the upper-left image corresponds to the distance in the object plane. The light spot is an area of reduced ion detection rate; its origin is under investigation. (c) Experimental (left) and computational (right) MCP images of plasma at τ = 10 μs in the presence of a quadrupole electric field. Instead of expanding outwards and leaving the field of view, the ions are refocused by the electric field and accumulate at a plasma focus, which maps onto a localized region on the MCP with well-above-average count density. (d) Experimental (top) and computational (bottom) distributions of ion MCP arrival times (horizontal axis) for different plasma expansion times (tilted axis). To enhance visibility, the count axes for the experimental data are magnified by factors of 1, 2, 4, 8, 8, and 8, in ascending order of expansion times. Likewise, the count axes for the computational data are magnified by factors of 1, 8, 32, 64, 64, and 64.

expansion time, the ion count decreases to about 10% of the initial value.

Figure 4.2 (d) shows experimental and simulated MCP arrival time distributions of the plasma ions for each expansion time τ. The arrival time traces have been aligned on the time axis so that the firing of the TIP imaging voltage pulse is at $t = 0$ (equivalent to the end of the expansion time τ). As τ increases, the ion arrival time distribution develops a leading and a lagging peak, signaling the formation of shock shells. As the plasma expands radially, a fraction of ions move toward the TIP, while another fraction of ions move in the opposite direction toward the MCP. When the TIP electric field is engaged, the ions closer to the TIP experience a stronger electric field than ions that are farther away. Hence, the longitudinal position distribution of the ions maps onto a time-of-flight distribution in which shorter times of flight correspond to ions closer to the TIP at the onset of the TIP imaging voltage pulse. The peaks in the time-of-flight distribution correspond to shells of enhanced plasma density, or shock fronts. In our data in

Fig. 4.2 (d), the shock fronts begin to form at $\tau = 4$ μs and are most prominent at $\tau = 6$ μs. While this scenario is well-supported by the simulations that underlie the numerical data in Fig. 4.2, it is noted that experimental and simulated arrival time distributions begin to differ from each other at about $\tau = 6$ μs and onward. These differences are attributed to details of the ion-imaging electric field in the chamber that come to bear once the plasma has significantly expanded off-axis. These fields may, in part, be the result of unknown higher-order multipoles of the TIP electric field, geometrical imperfections and stray potentials.

Additional experimental evidence for the importance of higher-order multipole electric fields is found in that it is not sufficient to zero the leading (dipolar) background electric field at the location of the initial plasma cloud. It is critical to zero the linear (quadrupolar) components of the field in order to achieve undistorted plasmas at long expansion times τ. This is possible in our setup because it has nine electric-field compensation electrodes. Incomplete field-zeroing results in a quadrupole field with a field zero inside the initial plasma cloud that typically causes the expanding plasma to refocus along certain directions of space, while defocusing along other (orthogonal) directions. Figure 4.2 (c) shows experimental and computational MCP images of a plasma at $\tau = 10$ μs in the presence of a quadrupole field that focuses the ions in the xz-plane and defocuses along the y-direction (coordinates defined in Fig. 4.1). In this case, the plasma focus generated by the quadrupole field manifests in a localized, kite-shaped region on the MCP of enhanced ion count density. The kite shape arises from astigmatism caused by the azimuthal dependence of the initial plasma cloud around the y-direction (see Fig. 4.1). In the present work, I have thoroughly field-zeroed the dipolar and quadrupolar field components to avoid this plasma focus effect. Nevertheless, remaining higher-order multipolar and other field perturbations are suspected as the main cause of deviations between experimental and simulated data at long expansion times.

4.3.2 Computational Thermodynamics

In the following I study the expanding plasma by tracking the spatio-temporal evolution of a set of macroscopic parameters. Most of this computational work is done with a molecular-dynamics simulation that accounts for all Coulomb and external forces. Here I describe the simulation method in some detail. In order to highlight the essential physics, I mostly model the expansion of spherically symmetric plasmas into field-free space. The molecular-dynamics simulation is quite flexible, though; it has been employed, for instance, to generate Figs. 4.2 (c), 4.2 (d) (lower panel), and Fig. 4.8 (right panel) to model the experiment in considerable detail.

4.3.2.1 Defining Temperature in a Non-Equilibrium Plasma

The particle system is large enough to describe its dynamics via time- and position-dependent macroscopic parameters in sub-volumes of the plasma that are close to a local equilibrium. To arrive at a suitable size and simple shape of the sub-volumes in the expanding plasma, in this section I restrict the study to a spherically symmetric system without external forces, so as to maintain macroscopic spherical symmetry. This allows us to break up the plasma into spherical partitions (shells) with a certain thickness, within which I find the localized thermodynamic parameters versus time.

As a guide for what constitutes a suitable shell number, I note that the correlation length evident from the above discussed correlation functions is on the order of 10% of the typical system diameter. Based on this, the plasma is divided into ten partitions: the core and nine shells. Each partition contains a tenth of all plasma particles. Further, for computation of the temperature and Coulomb coupling parameter I dynamically adjust the shell radii and thicknesses so that there always are 10% of the ions in each of the ten shells. For instance, for a plasma of 150 particles the outer radius of the innermost shell, $i = 1$, is the average of the radial coordinates of the 15-th and the 16-th particle, after sorting the particles in ascending order of their radii, and so on. Radial coordinates are measured relative to the symmetry center of the plasma. The dynamic variables in each simulation include the inner and outer radii of the shells, $r_{in,i}(t)$ and $r_{out,i}(t)$, with shell index $i = 1, 2, ..., 10$, and the ion-averaged shell radii, $r_i(t)$, and velocities $v_i(t)$. As the plasma expands, all shell radii expand. Ions are allowed to switch between adjacent shells so as to maintain a fixed number of ions in the shells.

From $r_{in,i}(t)$ and $r_{out,i}(t)$ I directly get the time-dependent shell volumes. The ion densities $n_{V,i}(t)$ of the shells are then given by the fixed ion numbers in the shells divided by the shell volumes. To find temperatures and coupling parameters, it is important to first obtain the continuous macroscopic velocity function of the ions as a function of position. By symmetry, the macroscopic velocity function only has a radial component, $\bar{v}_r(r, t)$. For each of the ten shells, $\bar{v}_r(r, t)$ is taken to be identical with a quadratic fit to the actual (microscopic) radial velocities of all ions in the shell. Since each of the shells i has its own time-dependent velocity fit parameters, I add an index i to the velocity fit functions, $\bar{v}_{r,i}(r, t)$. During the course of the up to 10000 individual simulations, the accuracy of the fits $\bar{v}_{r,i}(r, t)$ is continually improved by taking the particle velocities of all earlier individual simulations into account when finding the fit functions $\bar{v}_{r,i}(r, t)$. The temperature of the i-th shell, $T_i(t)$, is then given by the root-mean-square deviation of the particle velocities from the macroscopic average, $\bar{v}_{r,i}(r, t)\hat{\mathbf{r}}$, with radial unit vector $\hat{\mathbf{r}}$. While the accuracy of the fits $\bar{v}_{r,i}(r, t)$ is critical in the described model, I note that a poor model for $\bar{v}_{r,i}(r, t)$ would result in higher temperatures and lower Coulomb coupling parameters. The results I show are understood to be close upper bounds for the actual macroscopic temperatures $T_i(t)$ and close

lower bounds for the Coulomb coupling parameters, $\Gamma_i(t)$.

Once temperatures and densities are known, in the simulation one can readily calculate other macroscopic parameters such as the Debye length, the ion acoustic velocity, and the ion plasma frequency. Each of these parameters depends on shell index i and time.

I typically conduct 1000 to 10000 simulations for a given set of initial macroscopic plasma conditions, and average the results for plasma density, temperature, etc. over these simulations.

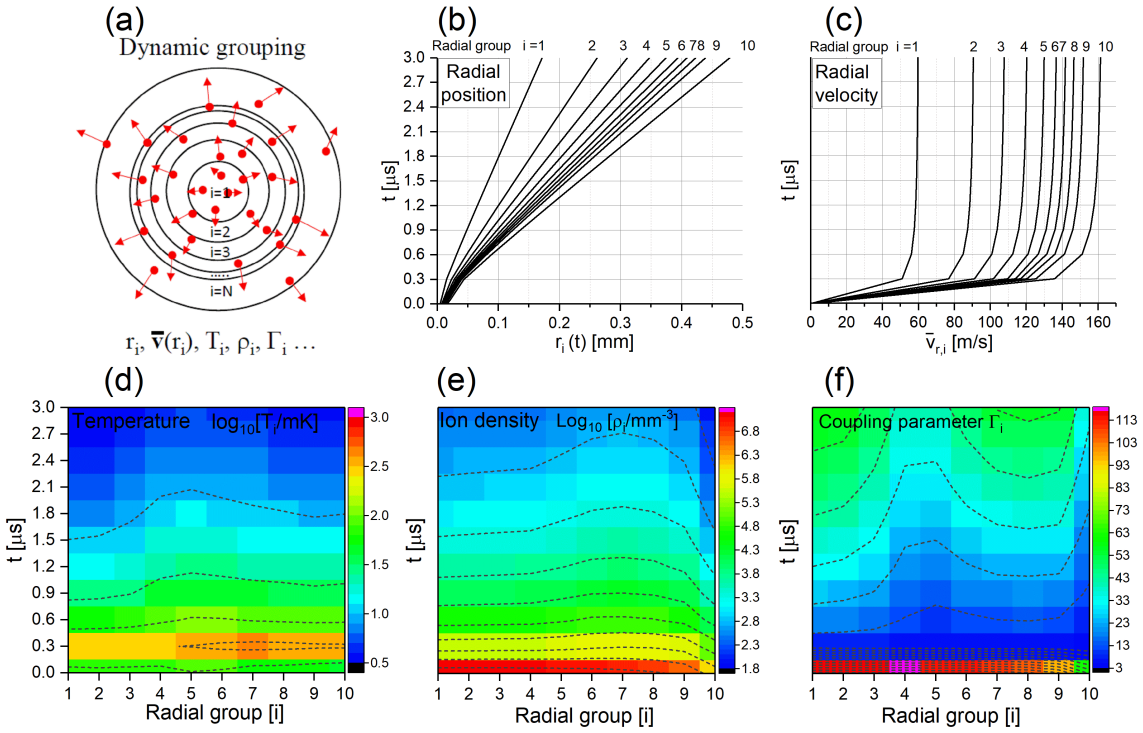

Figure 4.3: (a) Sketch of the radial-partition (shell) model explained in the text. The shell radii, the macroscopic velocity $\bar{v}_{r,i}(r,t)$ and other plasma parameters depend on shell index i and time. (b) Average shell radii (horizontal axis) obtained for 125 ions with an initial cloud radius of about 20 μm vs expansion time (vertical axis). Shell indices listed on top. (c) Corresponding average shell velocities. (d) Ion density vs shell index (horizontal axis) and expansion time (vertical axis), displayed on a logarithmic color map. (e) Temperature vs shell index (horizontal axis) and time (vertical axis), displayed on a logarithmic color map. (f) Coulomb coupling parameter Γ vs shell index (horizontal axis) and time (vertical axis), displayed on a linear color map.

4.3.2.2 Disorder-Induced Heating

In analogy with the experiment, in the simulation in Fig. 4.3 I choose (spherical) saturated Gaussians with radii of about 20 μm for the initial density profile. For the initial velocity distribution I use a fixed velocity magnitude given by the recoil that occurs in photo-ionization. Photo-ionization of the Rb $5P_{3/2}$ state with 355-nm laser light has a kinetic-energy release of 0.9 eV, of which 5.8 μeV is picked up by the ions. The initial distribution of ion velocity angles is given by

the linear polarization direction of the photo-ionization laser and spherical harmonics. I choose an ion number of 125, which leads to conditions similar to our experiment. The plasma is then dense enough that the velocity distribution locally thermalizes quickly enough so that details of the photo-ionization are negligible (only the initial velocity-magnitude has a small effect). Also, the depth of the space-charge potential well for electrons after plasma excitation is only 13 meV, *i.e.* in the plasmas generated by photo-ionizing Rb $5P_{3/2}$ atoms with 355-nm laser light all photo-electrons (energy 0.9 eV) near-instantaneously escape from the ion plasma and do not contribute to its dynamics.

Fig. 4.3 shows density, temperature, and coupling parameter. The system is, initially, very far away from any type of equilibrium, because the initial Coulomb potential energy of the disordered ion cloud, after the electrons have escaped, exceeds the photo-ionization recoil energy of the ions by a factor near 1000. This implies that the initial kinetic energy of the ions does not play an important role, and that its initial Coulomb coupling parameter of near 100, computed from initial density and kinetic energy, does not have much physical meaning. I see from the temperature plot in Fig. 4.3 that the plasma as a whole heats up from tens of mK to near 1 K within a fraction of a microsecond; this is due to disorder-induced heating, a concept discussed in Chapter 3. During that time the plasma reaches a dynamic steady-state, and temperatures and coupling parameters computed for the 10 radial partitions become physically meaningful. The ion plasma frequency, $f_{p,i}$, drops from several MHz to about 0.5 MHz during that time, and the Debye length increases from sub-μm to several μm. In this phase, the coupling parameter Γ traverses a low point of about six, *i.e.* even in this hottest phase the plasma is strongly coupled.

4.3.2.3 Adiabatic Cooling and Shock Fronts

After a few hundred ns, the plasma transitions from heating into an adiabatic expansion phase of about one microsecond. During that phase the particles are still collisionally coupled while the overall acceleration caused by the Coulomb explosion fades and the spherical partitions approach a radially dependent terminal velocity. During this time, much of the initial plasma energy gets converted into the directed (non-thermal) kinetic energy of the expanding spherical partitions. Near the end of the expansion time in Fig. 4.3 the directed kinetic energy outweighs the thermal kinetic energy by a factor of about 10^4, and the potential energy vanishes. This further implies that during the adiabatic expansion the outer spherical partitions of the plasma turn highly supersonic, reaching Mach numbers of about 40 in the outermost partitions.

In the course of adiabatic expansion the shock front develops, as seen in a relative rise in particle density in the outer radial partitions and a radial bunching of a few radial partitions around the partition $i = 8$. Within the shock region, other macroscopic plasma parameters differ from their values in the intermediate radial region of the plasma. For instance, the temperature

is about 20% lower and the coupling parameter is about 30% higher. Importantly, the coupling parameter increases, overall, and approaches ~ 20 at about 1 μs (within the shock region). Later into the expansion, the particles collisionally mostly de-couple, but the system continues to ballistically cool. After 3 μs of expansion time, the Coulomb coupling parameter exceeds 50, and the temperature has dropped to about 4 mK (from an initial photo-ionization recoil energy equivalent to 44 mK).

For a further discussion of collisional de-coupling, in Fig. 4.4 I show the ion plasma frequency vs shell index i and free-expansion time t. For our conditions, f_p can be taken to be on the order of the collision frequency, because the time it takes to efficiently transfer potential into kinetic energy and vice versa is about a quarter of the ion plasma oscillation period, $1/f_{p,i}$. After its initial drop to ~ 0.5 MHz during the first few hundred ns, the plasma frequency $f_{p,i}$ is still sufficiently high to effectuate collisional coupling in the expanding plasma. The plasma oscillation period, $1/f_{p,i}$, rapidly drops to below $0.1t$ during an expansion time $t \approx 1$ μs. In comparison, the shock front becomes established as early as about 300 ns into the expansion. At times past $t \approx 1$ μs the expanding plasma collisionally decouples, as the plasma frequency continues to drop to several tens of kHz near the end of the simulated expansion. As the plasma collisionally decouples, the shock front becomes frozen into the ballistically expanding system.

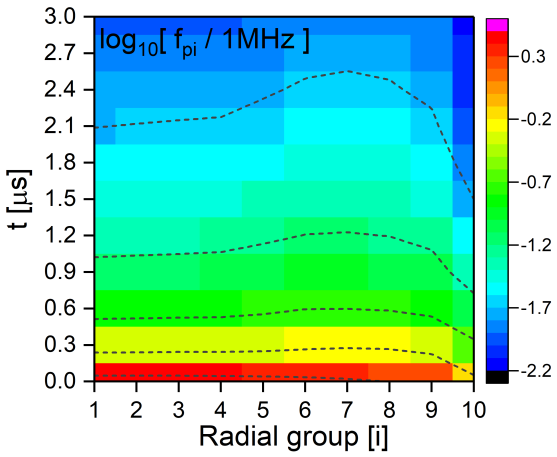

Figure 4.4: Ion plasma frequency, $f_{p,i}$, from the same simulation as in Fig. 4.3 vs shell index (horizontal axis) and expansion time (vertical axis), displayed on a logarithmic color map.

As the plasma collisonally decouples, the Coulomb coupling parameter Γ becomes ill-defined because the system increasingly departs from local thermal equilibrium (due to a lack of collisions). The coupling parameters Γ in Fig. 4.3, at times $t \gtrsim 1$ μs, are to be interpreted as effective values that measure the ratio of potential and kinetic energy.

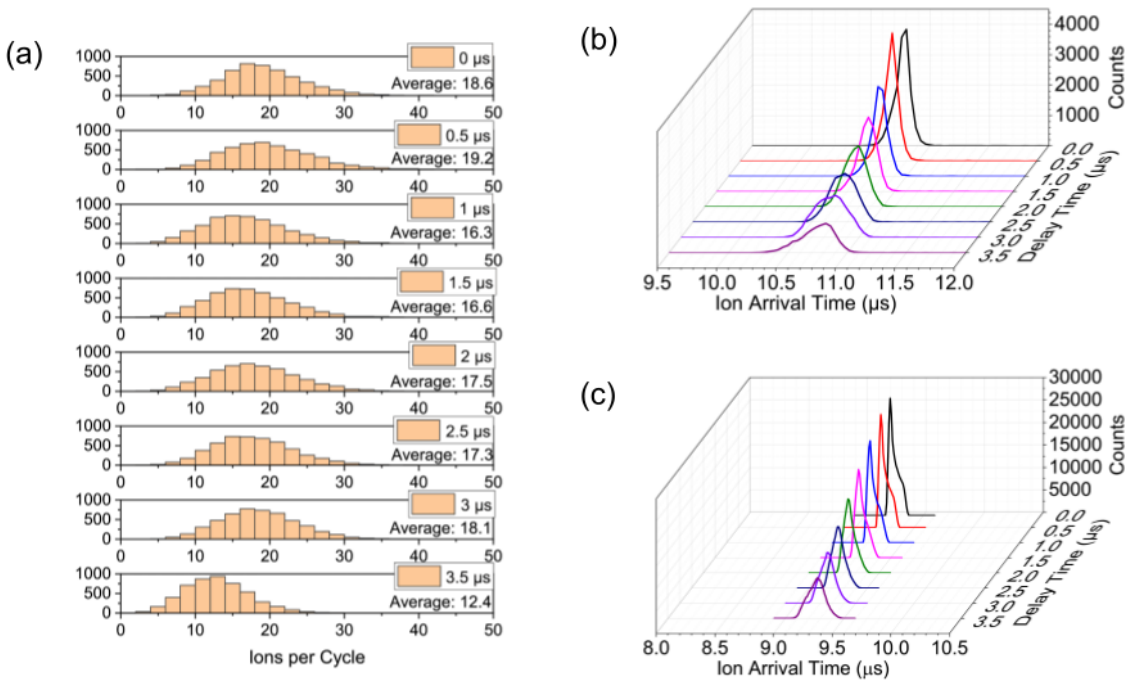

Figure 4.5: (a) Histograms of ion counts per cycle in the lower-density regime. (b) Experimental and (c) simulated distributions of ion arrival times for different plasma expansion times at lower density.

4.4 Lower-Density Plasma Expansion

The lower-density plasma is prepared from an atom cloud containing 1.3×10^6 atoms at a density of 7.7×10^{10} atoms/cm^3. The initial central ion density in this case is $n_{avg} \approx 10^9$ cm^{-3}, Due to the smaller number of counts, compared to the higher-density plasma case in Sec. 4.3, in the lower-density case I limit the expansion time τ to 3.5 μs, and I use shorter time steps of 0.5 μs. The most interesting expansion and correlation dynamics occur over that time scale. Again, I take 5000 shots at each of these expansion times. The magnification factor of the imaging for this data set is 60 times.

Figure 4.5 shows the ion count statistics and arrival time distributions. Because this plasma is lower in density and smaller in size, it exhibits a less forceful Coulomb expansion. As a result, the average ion count remains fairly constant for $\tau < 3.5$ μs; even at $\tau = 3.5$ μs only a small fraction of ions leaves the field of view (see Figs. and). I also no longer observe a bifurcation of ion arrival times, though the arrival time distribution does broaden with longer expansion times. These observations indicate that the lower-density plasma does not produce pronounced shock shells over the course of its expansion. Because of the lack of observed shock shells, this plasma was only modeled with the molecular dynamics trajectory simulation, and not with the fluid simulation.

4.4.1 Ion Pair Correlations

Between the two density regimes investigated in this chapter, the lower-density plasmas are better-suited to study correlation effects that develop on a timescale of several microseconds. Because of its higher overall ion count and larger size along the projection direction, the higher-density plasma is plagued with ion projection issues which distort the pair correlation measurements. The higher-density plasma also expands and leaves the field of view faster, leaving few ions for pair correlation calculations. The lower-density plasma, on the other hand, is relatively free of these issues. Additionally, the lower-density plasma retains its initial cylindrical shape longer, which gives rise to asymmetric correlation lengths between the axial and radial directions of expansion.

I calculate ion pair correlations at each expansion time τ by first processing the raw images with a peak finder algorithm, obtaining the pair correlation of the peaks, and normalizing the repetition-averaged pair correlation such that a value of one corresponds to an absence of correlations. In Fig. 4.6, I show images that are averages over the 5000 repetitions for each delay time, along with the corresponding normalized pair correlations. On a macroscale (distances $\gtrsim 100$ μm), the pair-correlation functions expand in a manner that reflects the overall plasma expansion. This is seen in Fig. 4.6 for $\tau \leq 1$ μs; at later times, the pair correlations do not show any macroscale structure within the displayed field of view. The center regions (distances $\lesssim 100$ μm) of each pair correlation reveal the short-range correlations between ions with their nearest neighbors, as seen by the lighter region surrounding the center. These correlations are due to Coulomb repulsion. The range within which ion pairs are under-abundant (correlation < 1) increases over time, meaning that the minimum separation between repelling ion pairs increases with time. These correlations are a hallmark of strong coupling and are closely related with disorder-induced heating [79], which is observed in the present work by spatially-resolved ion imaging.

Furthermore, inspection of Fig. 4.6 shows that the ion separation increases faster in the vertical than it does in the horizontal direction. This is due to the overall geometry of our plasma. The axis of the plasma cylinder is aligned horizontally across the photos, and the comparatively smaller radius of the cylinder stretches out vertically. As ions pairs separate from each other axially, they eventually interact with initially distant ions that suppress further expansion. Conversely, in the radial directions the ions expand into free space, unimpeded by other ions.

To highlight the difference between radial and axial correlations, I produce angular integrals of the pair correlations. Figure 4.7 shows experimental and computational angular integrals, $I_{\text{ax}}(r)$ and $I_{\text{rad}}(r)$, along with the corresponding integration regions. Experimental and corresponding simulated results agree very well in terms of the triangular shape of the pair-correlation functions, their gradual expansion to larger distances, and the presence of enhanced correlation at $\tau \lesssim 1$ μs in a range 10 μm $\lesssim r \lesssim 20$ μm, where $I(r) > 1$. Just as the pair correlation images

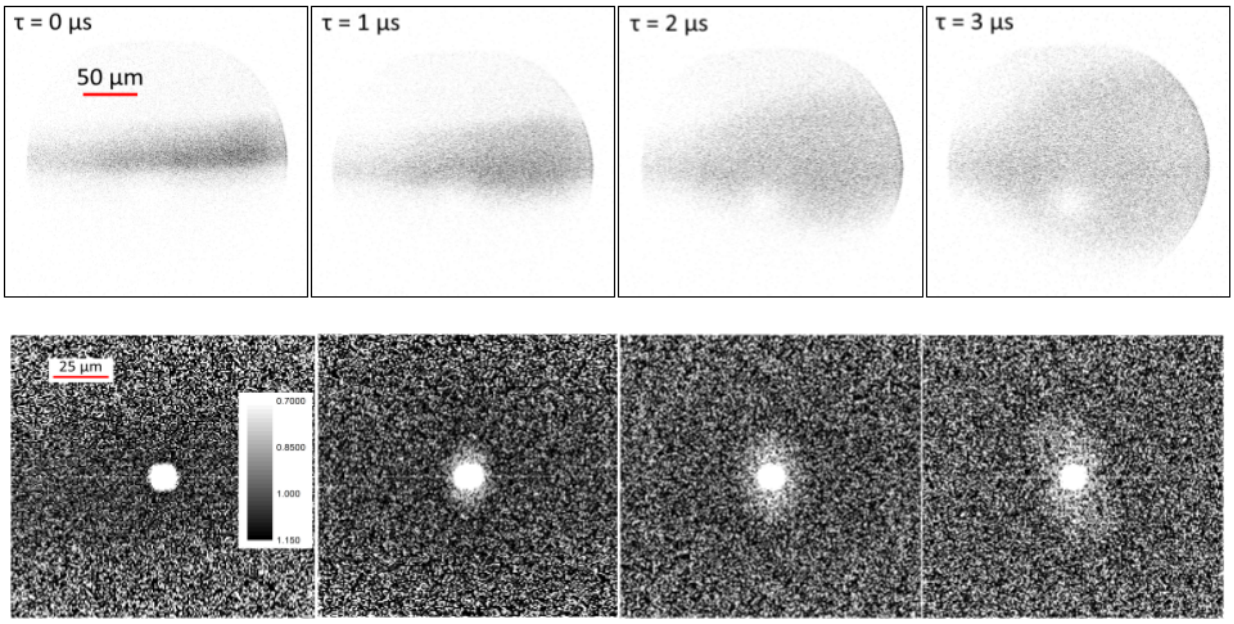

Figure 4.6: Images of lower-density plasma expansion. On the top row are averaged images of expansion at the indicated expansion times τ. On the bottom are pair correlations of the raw images at the same time steps. The grayscale is calibrated such that a value of 1 implies no correlation.

suggest, I find that the regions of anti-correlation ($I(r) < 1$) expand faster in the radial than the axial direction. To further quantify this, I apply two linear fits to each trace as illustrated in the inset image in Table 4.1. I then calculate the intersection point of the two linear fits to find the correlation lengths, ρ_{ax} and ρ_{rad}, for the axial and radial directions respectively. These lengths are listed in Table 4.1, along with their ratios.

I note that the simulated correlation lengths, ρ_{axc} and ρ_{radc}, are greater than the measured correlation lengths by up to 30% before the last time step. This discrepancy is most likely a result of image distortion due to higher-order multipole field effects in the ion-imaging system. I also see that the measured and computed correlation functions $I(r)$ drop below 0.4 as $r \to 0$. These drop-offs are artifacts that occur at different distances. In the experimental plots, the drop-off occurs at ≈ 6 μm because of the ion blip size on the MCP (in the object plane). In the simulated plots, the drop-off occurs at ≈ 2 μm, which is the bin size in the simulation.

Pair correlation integrals for the higher-density plasma are presented in Fig. 4.8. The $I_{2D}(r)$ reveal anti-correlation, $I_{2D}(r) < 1$, out to a distance that increases with τ, reaching $\approx$ 50 μm at $\tau = 6$ μs. At $\tau \gtrsim 0$ μs there is a region of enhanced correlation $I_{2D}(r) > 1$, at $r \sim 10$ μm. While these pair correlation integrals comport with the strong coupling presented in Sec. 4.3.2, I note that these correlation data are not as clean as the correlation data for lower-density plasma.

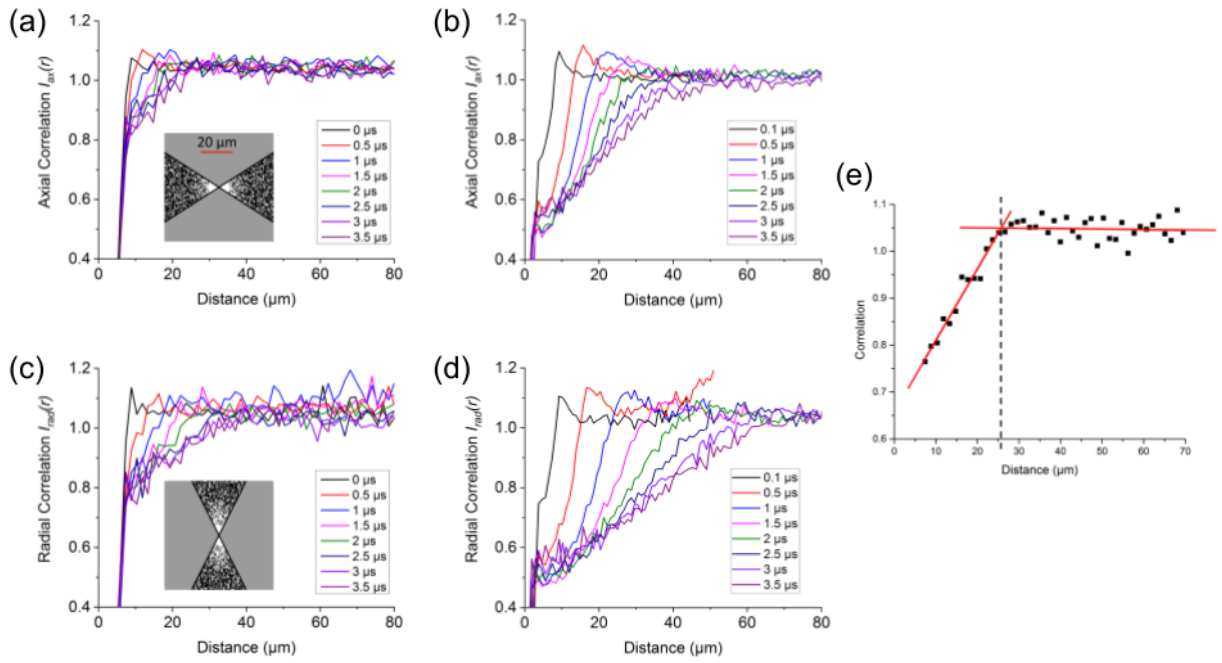

Figure 4.7: Experimental (a and c) and computational (b and d) axial and radial angular integrals of the pair correlation functions for each time step. The inset images are the integration regions. Each integral was performed over the specified region to show the difference in pair correlations in the radial and axial directions. (e) Sample data set with lines demonstrating how correlations lengths are measured.

Expansion Time [μs]	Axial [μm]		Radial [μm]		Radial/Axial Ratio	
	ρ_{ax}	ρ_{axc}	ρ_{rad}	ρ_{radc}	Exp.	Comp.
0.0	7.70	–	8.37	–	1.09	–
0.1	–	8.66	–	8.62	–	1.00
0.5	10.10	13.68	13.95	15.19	1.38	1.11
1.0	14.98	18.31	19.76	24.13	1.32	1.32
1.5	16.37	21.74	25.21	32.11	1.54	1.48
2.0	19.70	25.68	28.15	38.73	1.43	1.51
2.5	23.09	30.02	35.53	50.64	1.54	1.69
3.0	25.36	35.28	38.16	59.27	1.50	1.68
3.5	26.76	38.71	42.76	67.17	1.60	1.74

Table 4.1: Measured axial and radial correlation lengths, ρ_{ax} and ρ_{rad}, vs. time, and respective simulated values, ρ_{axc} and ρ_{radc}, obtained from the angular integrals in Fig. 4.7, using the method shown in Fig. 4.7 (e). The last two columns show the measured and simulated ratios between the correlation lengths.

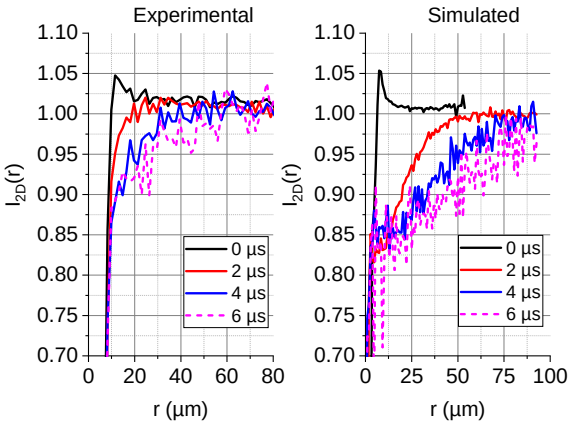

Figure 4.8: Projected, two-dimensional ion pair correlations $I_{2D}(r)$ for the indicated expansion times, measured vs radial coordinate in the xz object plane. The left panel is for experimental and the right one for simulated data. Pair correlations for $\tau > 6$ μs are not shown because they are too noisy, as a result of the diminishing ion number in the images. The steep drop in the data at distances $\lesssim 8$ μm is an experimental artifact caused by the finite blip size of the ion counts on the MCP.

4.5 Conclusion

In this chapter, I have presented observations of cold-ion plasma expansion by time-delayed ion extraction and ion imaging on a position-resolving particle detector. This plasma has been explored at two different density regimes, and results have been compared with two models: a particle model and a fluid model.

From the experimental data, I have seen that as the higher-density plasma expands, shock fronts of high ion density form at the plasma-vacuum interface (the outer layers of the expanding plasma). Computer simulations verify that these density build-ups are shock shells, which are accompanied by variations in other macroscopic plasma parameters (temperature, Coulomb coupling parameter). Computer simulations also show that the higher-density plasma is strongly coupled over its entire lifetime, even during disorder-induced heating when the plasma is at its hottest. The lower-density plasma does not exhibit shock shells, but it produces clean pair correlation integrals that show asymmetric correlation lengths, a result of the initial cylindrical plasma shape. The higher-density plasma also yields pair correlations that, while not quite as good as the lower-density pair correlations, give some evidence of the strong coupling of the system.

CHAPTER 5

Photoionization of Rydberg Atoms Across the Optical Spectrum

The work discussed in this chapter contains material published in Ref. [80].

Photoionization, or the photoelectric effect, is the act of liberating a bound electron from an atom with a photon. It should be abundantly clear at this point that PI is vital to entire field of small-scale, tabletop plasmas, both room-temperature and cold. Without PI, we would not be able to make atomic-based plasmas with relative ease, much less reach the strong-coupling regime in a lab environment.

PI is one of the many physical phenomena that can be described by the minimal coupling Hamiltonian. Minimal coupling in general is a coupling between fields and charged particles that only involves the charge distribution; things like higher multipole moments and particle spin are ignored in this formalism. Thus, minimal coupling can describe all electrodynamic processes, including PI. The minimal coupling Hamiltonian in SI units is given by the following expression:

$$H = \sum_i \frac{(p_i - qA_i)^2}{2m} + q\varphi \tag{5.0.1}$$

In this expression, p is momentum, and φ and A are the scalar and vector potentials from electromagnetism. These potentials account for the **E** and **B**-field configurations. The term in the numerator of the fraction is squared, and cross-multiplication yields p^2, A^2, and $\hat{\mathbf{A}} \cdot \hat{\mathbf{p}}$ terms. The p^2 term is the regular momentum term in any Hamiltonian. The other two terms are the contributions of the vector potential to the Hamiltonian, and they each govern different effects. The $\hat{\mathbf{A}} \cdot \hat{\mathbf{p}}$ term describes cases where the photon is absorbed; PI is an example of an $\hat{\mathbf{A}} \cdot \hat{\mathbf{p}}$ interaction. The A^2 term, or $|A|^2$ term, is responsible for photon scattering. Photon scattering can be further subdivided into two categories: the low photon energy case, where the collision is elastic and the photon energy remains constant (Thomson scattering), and the high photon energy

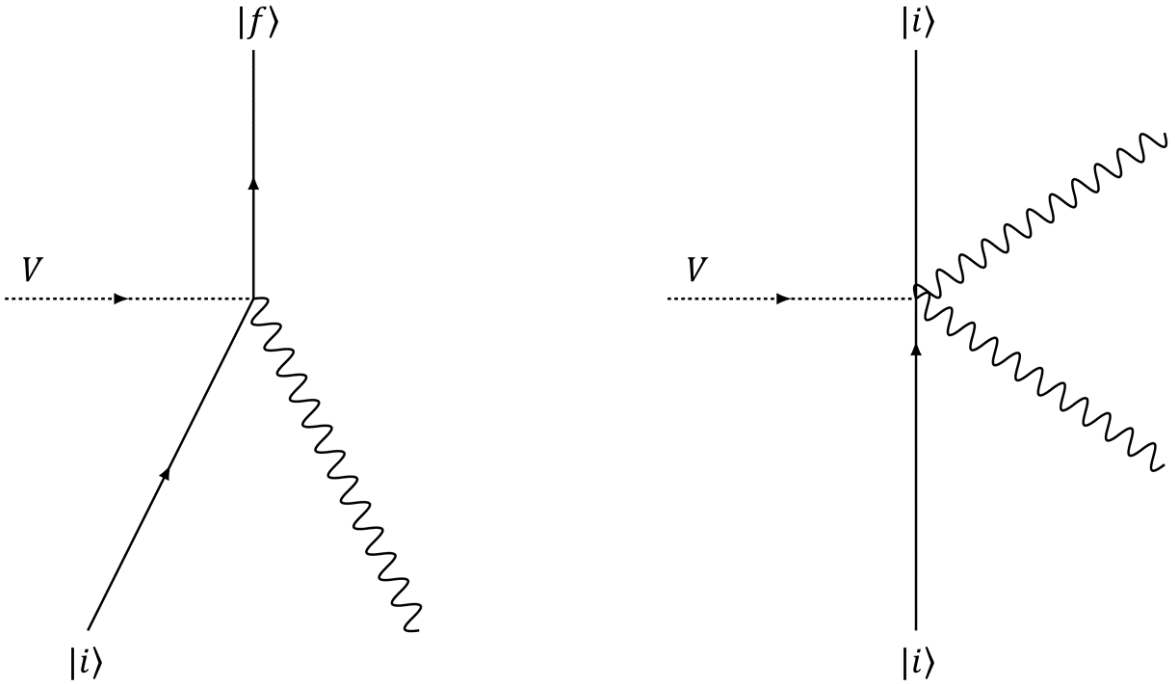

Figure 5.1: Feynman diagrams illustrating the $\hat{\mathbf{A}} \cdot \hat{\mathbf{p}}$ (left) and $|A|^2$ (right) interactions. Here, both processes are drawn with the atomic potential V included. In the $\hat{\mathbf{A}} \cdot \hat{\mathbf{p}}$ interaction, the photon is absorbed and the atomic state changes. In the $|A|^2$ interaction, the photon scatters, and the atomic state remains unchanged.

case, where the collision is inelastic and the photon loses energy from the collision (Compton scattering). Figure 5.1 shows Feynman diagrams for the $\hat{\mathbf{A}} \cdot \hat{\mathbf{p}}$ and $|A|^2$ interactions.

The energy balance of PI is described by the following equation:

$$K = h\nu - \Phi \tag{5.0.2}$$

Here, K is the kinetic energy of the free electron, h is Planck's constant, ν is the frequency of the incident photon, and Φ is the work function, or photoionization threshold energy, of the atom. If the energy of the incident photon is less than the work function, the atom will not be ionized. As an example of this, consider the plasma system from Chapter 4. Rubidium atoms in the intermediate $5P_{3/2}$ state have a work function of 2.588 eV, so the minimum length ionizing wavelength is 479.1 nm. The ionizing laser, meanwhile, emits 355 nm light, producing photons with 3.49 eV of energy each. Therefore, the electrons after PI have excess kinetic energy of 0.902 eV each.

In general, as the energy of the incident photon increases, the atom becomes less sensitive to PI at that particular wavelength. This sensitivity is quantitatively described by the photoionization cross section, σ, which is usually given in units of either cm^2 or barns (1 barn $= 10^{-24}$ cm^2). The greater the cross section, the more likely PI is to occur. However, in certain PI channels this

general trend is interrupted by pronounced minima in the cross sections as a function of wavelength λ of the ionizing field. These minima are caused by Cooper minima and shape resonance, both of which will be explained in detail in Sec. 5.1. Photoionization minima are also accessible in Rydberg-state atoms, which have broad PI spectra in the UV, visible, and NIR regimes due to their loosely-bound electrons and low work functions.

In this chapter, I present a computational study on PI of rubidium and cesium in Rydberg states. Calculations of wavelength-dependent PI cross sections reveal Cooper minima and shape resonances at various ionization channels and UV/visual wavelengths. The atoms were simulated using model potentials sourced from [M. Marinescu, H. R. Sadeghpour, and A. Dalgarno, Phys. Rev. A **49**, 982 (1994)]. At the end of the chapter, I discuss potential experimental investigations of these findings.

As an aside, it is worth mentioning that PI of Rydberg atoms is not a good way to produce a plasma. Compared to the two-photon ionization process discussed in Chapter 4, Rydberg photoionization requires three photons, and therefore three lasers. The additional excitation step also reduces the overall efficiency of the PI process, leading to fewer overall ions compared to a two-step ionization process in an identical source of atoms. This in turn leads to lower ion cloud densities, meaning that you may not even reach the threshold density and minimum Debye length required to consider the ion cloud a plasma.

5.1 Background

5.1.1 Cooper Minima and Shape Resonances

As mentioned in the beginning of the chapter, PI minima are caused by two distinct physical mechanisms: Cooper minima, and shape resonances. These mechanisms are caused by different underlying physics, and they can be differentiated experimentally.

Cooper minima were first reported by John Cooper in 1962, in a paper titled "Photoionization from Outer Atomic Subshells. A Model Study." [81]. In this paper, Cooper used the Hartree-Fock equations and central field models for the potentials to calculate wavelength-dependent PI cross sections of several species, including sodium, silver and copper ions, and several noble gases. He noted that while the central potential models were somewhat crude approximations, they were sufficient enough to predict the spectral shape of the cross sections. Once he determined the wavefunctions, he calculated the PI matrix elements by integrating over products of initial- and final-state electron wavefunctions. Cooper noticed that the wavefunctions were quasi-periodic with different spatial periods and phases, but at certain values of λ, the matrix-element integral would vanish, causing the PI cross section to vanish as well. While he did not give these

vanishing points a specific name in this paper, they would come to be known as Cooper minima.

Because Cooper minima are caused by initial- and final-state wavefunctions and the resulting PI matrix element, they are a purely quantum mechanical phenomenon and have no classical analogue. Additionally, the free-state wavefunction on its own does not exhibit any special behavior at a Cooper minimum. The associated dips in the PI cross sections as a function of λ can be hundreds of nm wide. Various experiments and theoretical investigations have been performed over the years to find Cooper minima. Aymar et. al. investigated Cooper minima of one-electron systems (Li, Na, K, Rb, Sr^+) using quantum defect theory [82, 83], and Msezane and Manson found Cooper minima in a wide range of atomic species (fluoride, $Z = 9$, to cesium, $Z = 55$) at lower-lying, non-Rydberg excited states ($3d, 4d, 5d$) [84]. More recently, Zatsarinny and Tayal numerically calculated Cooper minima in potassium [85], which were later verified experimentally by Yar, Ali, and Baig [86]. Beterov et. al. calculated transition probabilities and PI cross sections of alkali metals using a Coulomb approximation and a quasiclassical model [87]. Additionally, there have been measurements of the Cooper minimum of atoms in a plasma background [88–90].

Shape resonances, on the other hand, are due in part to centrifugal potentials, which also appear in classical mechanics. At certain ℓ-values, potential barriers can form from the sum of a short-range attractive potential with a repulsive core and the long-range centrifugal potential, $\hbar^2\ell(\ell+1)/(2m_e r^2)$, with electron angular momentum ℓ, electron mass m_e, and electron radial coordinate r. These potential barriers can result in an inner well which can maintain quasi-bound scattering states. The centrifugal term is the quantum variant of the classical centrifugal term, $L^2/(2I)$, where L is the angular momentum and I is the moment of inertia of the Rydberg atom. In the quantum variant, $L^2 = \hbar^2\ell(\ell+1)$. The moment of inertia for a Rydberg atom is $I = \mu r^2$, where μ is the reduced mass of the system. For most atomic systems, $\mu = m_e$ since the atomic mass is much greater than the electron mass. The reduced mass only really matters for special cases such as muonic hydrogen or positronium where the masses of the two bodies are within the same order of magnitude.

As λ of the ionizing photon is varied, the free-electron wavefunction can pass through a narrow resonance in the inner well, characterized by a large-amplitude quasi-bound scattering state inside the barrier and a π phase shift outside the barrier. In certain Rydberg-atom PI channels, shape resonances cause minima in the PI cross sections; these tend to be narrower as a function of λ than Cooper minima. Shape resonances have been seen in photoionization calculations for francium [91], observed in positronium [92] and in atom collisions [93–95], and used to form Rydberg molecules [96, 97]. It must be said that shape resonances cannot occur without short-range core potentials that establish the potential barrier; the centrifugal potential on its own does not produce a suitable potential well for quasi-bound scattering states. Furthermore, these short-range core potentials must fall off faster than $1/r^2$ to form a well with the centrifugal

potential.

5.1.2 Atomic Model Potentials and Wavefunctions

The PI cross sections cannot be calculated without initial-state and final-state electron wavefunctions, and the wavefunctions themselves cannot be determined without corresponding atomic potentials. Furthermore, these calculations must account for quantum defects such as charge screening and core penetration, so one cannot use simple Coulombic potentials to simulate rubidium and cesium. Instead, these calculations require atomic model potentials that include quantum defects. In this work, rubidium and cesium atoms were simulated using model potentials written by M. Marinsecu, H. R. Sadeghpour, and A. Dalgarno in the early 1990's. These model potentials were used to investigate dispersion coefficients in alkali-metal dimers, atom excitation rates, and dipole polarizabilities [98–100]. All three of these studies strongly depended on quantum defects in the atomic potentials, so the model potential codes were carefully written to include all possible perturbations. The model potentials are still widely used, decades after they were first written.

The model potentials $V_{0,\ell}(r)$ include correction terms to the Coulomb potential that yield the correct core-penetration and ion-core polarization quantum defects of the atomic energy levels for various angular momenta ℓ. The model potentials depend on atomic species and on ℓ, with the potentials of any one species being the same for all $\ell \geq 3$ [98]. Including the (species-independent) centrifugal term yields effective potentials:

$$V_\ell(r) = V_{0,\ell}(r) + \frac{\hbar^2 \ell(\ell+1)}{2m_e r^2} \quad . \tag{5.1.1}$$

$V_{0,\ell}(r)$ follows the form:

$$V_{0,\ell}(r) = -\frac{Z_\ell(r)}{r} - \frac{\alpha_c}{2r^4}\left[1 - \exp\left[-\left(\frac{r}{r_c}\right)^6\right]\right] \quad . \tag{5.1.2}$$

The first term is a modified Coulomb potential, and the second term is a fast-decaying term that covers additional core effects. α_c is the ℓ-independent core polarizability, $Z_\ell(r)$ is an ℓ-dependent function, and r_c an ℓ-dependent parameter. There are five ℓ-dependent fit parameters, which are provided in Eq. 18 and Table I in [98]. The potentials depend on atomic species. Also, for Rb and Cs, $V_{0,\ell>3}(r) = V_{0,\ell=3}$.

The wavefunctions are calculated using these potentials with a numerical method outlined by Reinhard et. al. [101]. This method features an algorithm that can continuously adjust the integration step size, which is useful for calculating free-electron wavefunctions. As for notation, I denote the initial Rydberg states $|i\rangle = |n, \ell, m_\ell\rangle$ with principal, angular-momentum

and magnetic quantum numbers n, ℓ and m_ℓ, respectively, and the photo-ionized free-electron states $|f\rangle = |\epsilon', \ell', m'_\ell\rangle$ with free-electron energy ϵ', and angular-momentum and magnetic quantum numbers ℓ' and m'_ℓ, respectively. The wavefunctions are then given by $\psi_i(\mathbf{r}) = \langle \mathbf{r}|i\rangle$ and $\psi_f(\mathbf{r}) = \langle \mathbf{r}|f\rangle$, with $\mathbf{r}$ being the relative electron position.

5.2 Calculating Photoionization Cross Sections

5.2.1 Matrix Elements and Cross Sections

PI is an effect of the $\hat{\mathbf{A}} \cdot \hat{\mathbf{p}}$-interaction of the minimal-coupling Hamiltonian [102] in first order. Given a linearly polarized plane wave with polarization unit vector $\hat{\mathbf{n}}$, wave vector $\mathbf{k}$ and angular frequency ω, the partial PI cross section is

$$\sigma = \frac{\pi e^2 \hbar^2}{\varepsilon_0 m_e^2 \omega c} \left| \hat{\mathbf{n}} \cdot \int \psi_f^* e^{i\mathbf{k}\cdot\mathbf{r}} \nabla \psi_i d^3 r \right|^2 \left(\frac{1}{E_H a_0^2} \right) , \tag{5.2.1}$$

Here I have the atomic energy unit $E_H \approx 27.2$ eV, and standard identifiers for other physical constants. The result is in SI units, m^2. The matrix element is computed in atomic units, with free states normalized in units of energy, i.e. $\langle \epsilon', \ell', m'_\ell | \epsilon'', \ell'', m''_\ell \rangle = \delta(\epsilon' - \epsilon'') \delta_{\ell'',\ell'} \delta_{m''_\ell, m'_\ell}$, and the term in parentheses within Eq. 5.2.1 converting the matrix-element square from atomic into SI units.

It is shown in Ref. [103] that for light-induced PI of Rydberg atoms the electric dipole approximation (EDA), $e^{i\mathbf{k}\cdot\mathbf{r}} = 1$, is valid at a level better than 10^{-4}, *i. e.* electric-dipole-forbidden transitions have cross sections that are smaller than those of the dipole-allowed ones by a factor of at least ten thousand. Making the EDA simplifies the integral in Eq. 5.2.1. Integrating and averaging the cross sections over the initial-state magnetic quantum number, m_ℓ, yields the shell-averaged partial cross section,

$$\bar{\sigma}_{n,\ell}^{\epsilon',\ell'} = \frac{\pi e^2 \hbar^2}{3\epsilon_0 m_e^2 \omega c} \frac{\ell_>}{(2\ell+1)} |M|^2 \left(\frac{1}{E_H a_0^2} \right) , \tag{5.2.2}$$

where M is the radial PI matrix element in atomic units,

$$M = \int_0^\infty u_{\epsilon',\ell'}(r) \left[u'_{n,\ell}(r) \mp \frac{u_{n,\ell}(r)}{r} \ell_> \right] dr. \tag{5.2.3}$$

There, the upper sign is for $\ell_> = \ell' = \ell + 1$ and the bottom sign for $\ell_> = \ell = \ell' + 1$. The functions $u_{*,\ell}(r)$ are given by $u_{*,\ell}(r) = r R_{*,\ell}(r)$, with the usual radial wavefunction $R_{*,\ell}(r)$,

and $* = n$ and $* = \epsilon'$ denoting the principal quantum number of the bound- and the energy of the free-electron state, respectively. The free-state energy follows from the wavelength of the PI light, λ, and the binding energy of the Rydberg atom. The free-state energy in atomic units is $\epsilon' = 2\pi a_0/(\alpha\lambda) - 1/(2n^{*2})$, where λ is entered in meters, the fine structure constant α, the effective quantum number $n^* = n - \delta_{n,\ell}$, and the quantum defect $\delta_{n,\ell}$.

For linearly polarized light, m_ℓ is conserved, and the m_ℓ-dependent PI cross sections follow from the shell-averaged ones via

$$\sigma^{\epsilon',\ell'}_{z,n,\ell,m_\ell} = \frac{3(\ell_>^2 - m_\ell^2)}{(2\ell_> + 1)(2\ell_> - 1)} \frac{(2\ell+1)}{\ell_>} \bar{\sigma}^{\epsilon',\ell'}_{n,\ell} \quad , \tag{5.2.4}$$

with similar expressions applicable to other light polarizations. Therefore, it is sufficient to discuss the PI behavior in terms of the shell-averaged $\bar{\sigma}^{\epsilon',\ell'}_{n,\ell}$.

5.2.2 Velocity and Length Gauges

The matrix element in Eq. 5.2.3 follows directly from the $\hat{\mathbf{A}}\cdot\hat{\mathbf{p}}$-interaction in the minimal coupling Hamiltonian (Eq. 5.0.1), along with the EDA. The matrix-element form in Eq. 5.2.3 is known as velocity form [102, 104]. In the case that the atomic potential is velocity-independent (not including the centrifugal term), the matrix elements can be converted into length form [102, 104], allowing an alternate, commonly used method to compute electric-dipole matrix elements. The matrix elements can be converted from the velocity gauge to the length gauge using the commutator $\hat{\mathbf{p}} = i[\hat{H}_0, \hat{\mathbf{r}}]$, where $\hat{H}_0$ is the field-free Hamiltonian. If the potentials are ℓ-dependent, though, then the conversion to length form is no longer valid, and the velocity form must be used.

This distinction between the velocity and length gauges is of utmost importance for the PI cross section calculations, particularly with the locations of the minima. Over the course of calculating these cross sections, I found that the PI matrix elements calculated in velocity and length forms are identical for $\ell \geq 4$, where a single ℓ-independent potential, $V_{0,\ell>3} = V_{0,\ell=3}$, applies to compute both the bound- and free-state wavefunctions. For $\ell < 4$, however, the model potentials are ℓ-dependent. Noting that the PI matrix elements involve wavefunctions with $\ell-$values differing by 1, PI channels with the smaller of the involved $\ell-$values, $\ell_<$, being less or equal 2 involve a set of two different model potentials. Consequently, the length-form results should be expected to become inaccurate (*i.e.*, to deviate from the velocity form). Indeed, for $\ell_< \leq 2$ the PI cross sections calculated in length form are typically off by $\sim 20\%$, with considerably larger relative deviations near the PI minima. Also, the λ-values of the Cooper minima differ by ~ 50 nm between the two forms. It is important to state that the velocity-form PI matrix elements are valid for all ℓ, because they do not require the commutator $\hat{\mathbf{p}} = \mathrm{i}[\hat{H}_0, \hat{\mathbf{r}}]$ to hold. For the PI cross-section calculations presented here, I have chosen $\ell = 0$ and $\ell = 2$, because these are experimentally

relevant cases. For these ℓ-values one must use the velocity-form expressions given in Eqs. 5.2.2 and 5.2.3.

As a side note, the difference between electric-dipole matrix elements calculated in length and velocity forms is orders of magnitude lower for bound-bound transitions between Rydberg states than it is for Rydberg-atom PI. For bound-bound Rydberg transitions, which are in the microwave to THz range, the length-form matrix elements are accurate enough for most purposes. However, the length form is not generally applicable to bound-free transitions, particularly in the optical regime. This finding can be explained, qualitatively, through the fact that the lower the transition energy is the more the matrix-element integral becomes dominated by contributions from the outer reaches of the electron configuration space, where all model potentials converge into an ℓ-independent Coulomb potential.

5.3 Rubidium Cross Sections

Figure 5.2(a) shows shell-averaged cross sections of three PI channels of Rb Rydberg atoms, namely $\bar{\sigma}^{\epsilon',\ell'=1}_{n=35,\ell=0}(\lambda)$, $\bar{\sigma}^{\epsilon',\ell'=1}_{n=35,\ell=2}(\lambda)$, and $\bar{\sigma}^{\epsilon',\ell'=3}_{n=35,\ell=2}(\lambda)$, for wavelengths ranging from the deep UV to the near-IR regime. The free-electron energy in atomic units is $\epsilon' = 2\pi a_0/(\alpha\lambda) - 1/(2n^{*2})$. Aside from the resonant features discussed later, it is seen that the $S \rightarrow P$ cross sections are fairly small over the entire range, topping out at only about 20 times the Thomson cross section, $\sigma_T = 0.665$ barn. In the near-IR spectral range, nS-type Rydberg atoms have PI cross sections that are lower than those of other low-ℓ PI channels by up to about three orders of magnitude. In contrast, the $D \rightarrow P$ and $D \rightarrow F$ channels in Fig. 5.2(a) follow the generic trend that PI rates rapidly increase at longer wavelengths. Between $\lambda = 200$ nm and 700 nm, the PI cross sections of those channels increase by one to two orders of magnitude. Typically, the PI threshold will peak at the PI threshold, which depends on n and ℓ and is in the far-IR regime.

The plot $\bar{\sigma}^{\epsilon',\ell'=1}_{n=35,\ell=0}(\lambda)$ in Fig. 5.2(a) shows a minimum centered at $\lambda = 536$ nm. As the $S \rightarrow P$ channel is the only PI channel of S-type Rydberg atoms, the total PI cross section equals the partial cross section $\bar{\sigma}^{\epsilon',\ell'=1}_{n=35,\ell=0}(\lambda)$, and is below σ_T over a range 490 nm $\lesssim \lambda \lesssim$ 570 nm. Taking into account the asymmetry of the PI minimum in $\bar{\sigma}^{\epsilon',\ell'=1}_{n=35,\ell=0}(\lambda)$, I define the full width at half depth (FWHD) of the minimum as the range over which the cross section dips below half of the PI maximum seen in the UV range. For the Rb Cooper minimum, the PI maximum in the UV range is 10 barns, so the FWHD is the range over which the cross section dips below 5 barns. The FWHD is ≈ 240 nm, with the FWHD-range covering the spectral region $400 \lesssim \lambda \lesssim 640$ nm. The large width of the PI minimum in the $S \rightarrow P$ channel serves as an indicator that this is a Cooper minimum, as will be proven below.

The $D \rightarrow F$ channel shows a minimum centered at $\lambda = 366$ nm with a FWHD of only

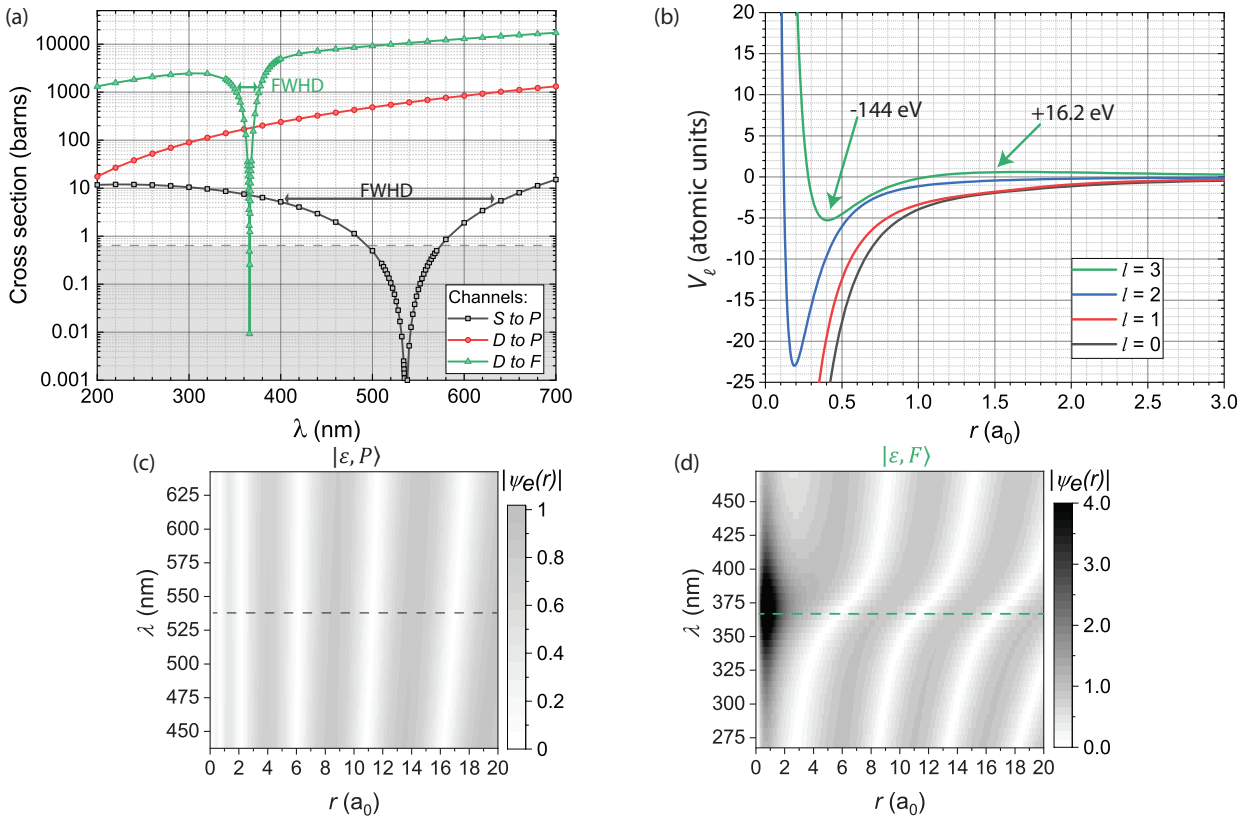

Figure 5.2: Rubidium: (a) Partial PI cross sections of $35S$ and $35D$ Rb Rydberg atoms vs PI wavelength λ: $S \rightarrow P$ (black squares), $D \rightarrow P$ (red circles), and $D \rightarrow F$ (green triangles). The dashed line shows the Thomson scattering cross section ($\sigma_T = 0.665$ barn), which is the elastic photon scattering cross section of the Rydberg atoms. In the gray region, elastic scattering exceeds PI. (b) Core region of the potentials $V_\ell(r)$ for $\ell = 0, 1, 2, 3$ in atomic units. (c) P-state free-electron wavefunction vs λ, with the Cooper minimum of the PI cross section indicated as a dashed line. The free-electron wavefunction exhibits an oscillatory pattern with a smooth, gradual phase shift as a function of λ, with no marked behavior at the Cooper minimum. (d) D-state free-electron wavefunction vs λ, with the shape resonance in the $D \rightarrow F$ PI cross section indicated as a dashed line. The plot shows a quasi-bound state centered at the shape resonance.

about 10 nm. The narrow width of this minimum is a first indicator that this minimum is different in nature from the minimum in the $S \rightarrow P$ channel; below I will show that the minimum in the $D \rightarrow F$ channel is due to a shape resonance. The $D \rightarrow P$ channel has no PI minimum within the range displayed in Fig. 5.2(a). I also did not find any minimum over an extended search across a wider range from 100 nm to 2 μm (not shown). The total shell-averaged PI cross section of Rb $35D$ is given by the sum of the partial cross sections, $\bar{\sigma}^{\epsilon',\ell'=1}_{n=35,\ell=2}(\lambda) + \bar{\sigma}^{\epsilon',\ell'=3}_{n=35,\ell=2}(\lambda)$. Hence, the observable cross section of the $35D$-state is the sum of two of the curves in Fig. 5.2(a). The total $35D$ PI cross section therefore has a minimum of about 200 barns at 366 nm, and rises to about 3000 barns several tens of nm away.

The physical differences between the PI minima in the Rb $S \rightarrow P$ and $D \rightarrow F$ channels become apparent when looking at the inner regions of the relevant free-electron model potentials, $V_\ell(r)$, and the free-electron wavefunctions. In Fig. 5.2(b) I show $V_\ell(r)$ for $\ell = 0$ to 3 and over the range $r \leq 3\ a_0$, and in Figs. 5.2(c) and (d) free-electron wave-function moduli for the $S \rightarrow P$ and $D \rightarrow F$ ionization channels, respectively, over the range $r \leq 20\ a_0$. Figs. 5.2(b)-(d) are focused on the central atomic region, where phase shifts and shape resonances determine the PI behavior. In Fig. 5.2(c), the free-electron wavefunction does not exhibit any noteworthy feature, as λ passes through the PI minimum. There merely is a gradual phase shift of the wavefunction due the slightly changing de-Broglie wavelength of the free electron. Hence, the PI minimum is due to incidental near-perfect destructive interference between bound-state and free-electron wavefunctions (where the bound-state function shows up in a modified form; see Eq. 5.2.3). This fact makes the PI minimum in the Rb $S \rightarrow P$ channel a Cooper minimum. Due to the rather gradual change of the free-state wavefunction, the Cooper minimum is comparatively wide in PI wavelength and free-electron energy. The Cooper minimum relates to the fact that the bound-state and free-state quantum defects differ by about 1/2 in Rb (the quantum defects are near 3.13 for S and 2.65 for P).

The free-state wavefunction of the $D \rightarrow F$ channel exhibits a resonant structure at the PI minimum, which manifests in the region of high wavefunction amplitude near $r \approx 1a_0$, as well as a phase change of $\approx \pi$ in the outer, oscillatory region of the wavefunction. The phase change is spread out over a few tens of nm in λ. The resonance occurs at the λ-value of the PI minimum, and it has a width in λ of only a few tens of nm. Another piece of insight follows from the $V_\ell(r)$, plotted in Fig. 5.2(b). There, it is seen that $V_{\ell=3}(r)$ exhibits an inner well formed by the centrifugal potential and the core region of the model potential $V_{0,\ell=3}(r)$ for $r \lesssim 1.5a_0$. (Note Eq.5.1.1 regarding the definition of $V_{0,\ell=3}$ and $V_{\ell=3}$). Of the four potentials shown, the $\ell = 3$ potential is the only one with an inner potential well and a centrifugal barrier. The potential barrier peaks at an energy of about $+16.2$ eV, and the inner well reaches a minimal value of about -144 eV. It is apparent that the resonance, which is at about $\epsilon' = 3.37$ eV, is the lowest and only quasi-bound state in the inner potential well of $V_{\ell=3}(r)$. These findings sum up to the statement

that the PI minimum in the $D \to F$ channel is due to a shape resonance. The phase shift of π of the scattering wavefunction across the resonance, seen in Fig. 5.2(c), is another telltale sign of a shape resonance [105].

It may seem counter-intuitive that the shape resonance manifests as a minimum in the PI cross section of the D to F channel (see Fig. 5.2(a)), while the free-state wavefunction exhibits the expected enhancement in the inner potential well (see Figs. 5.2(b) and (e)). This behavior results from destructive interference of the product under the integral in Eq. 5.2.3. While the free wavefunction displays only a single pronounced maximum inside the potential barrier, it is multiplied with the quasi-periodic term in the square bracket in Eq. 5.2.3. Here it happens to be the case that the PI matrix-element integral, $M(\lambda)$, passes through a zero crossing at $\lambda \approx 365$ nm, where it exhibits perfect destructive interference (and flips sign). The zero is almost exactly at the center of the free-state wavefunction's shape resonance peak (also located at $\lambda \approx 365$ nm). The coincidence leads to a near-symmetric dip in the D to F PI cross section versus λ. The corresponding PI shape resonance in the case of Cs, discussed in Section5.4, is less symmetric.

After identifying the physical origins of the PI minima, I wish to comment on a length-form calculation of the PI cross sections, which has yielded qualitatively similar behaviors with quantitatively notable differences (not shown). For instance, the Cooper minimum in the length-form result for Rb $\bar{\sigma}^{\epsilon',\ell'=1}_{n=35,\ell=0}(\lambda)$ is shifted up in wavelength by about 50 nm relative to the velocity-form result. While the (unphysical) shift in the length-form result is less than the width of the minimum, it is large enough to be of significance. The shift represents a case in which the length-form calculation exhibits a significant error relative to the velocity-form calculation. It is important to reiterate here that the velocity-form calculation is correct, while the length-form is expected to show an error because of the ℓ-dependence of the model potentials $V_{0,\ell}$. For $\ell \geq 4$ the PI cross sections obtained with the two forms agree, because the model potentials to be used for the bound (ℓ) and free-electron ($\ell' = \ell \pm 1$) states are identical (namely, $V_{0,\ell=3}$).

It is also worth commenting on free-electron photon scattering due to the A^2-term in the atom-field interaction [102]. Since the λ-range discussed in our work exceeds the atomic energy scale by orders of magnitude, the photon scattering has a cross section given by the Thomson scattering cross section, $\sigma_T = 0.665$ barn. For a truly free electron, the Compton (recoil) energy would be in the range of $h \times 10$ GHz. This recoil energy would be too small to cause atomic bound-bound transitions, nor does it cause photo-ionization of the atom (as in typical instances of the Compton effect). Therefore, the Thomson scattering of a Rydberg electron is perfectly recoil-free and elastic (except for a very small recoil of the entire atom). In the gray regions in Figs. 5.2 and 5.3, the elastic (Thomson) scattering rate exceeds the PI rate, and it may be measurable. Comparing the two effects, I further note that the Thomson scattering is due to the A^2-term in the atom-field interaction, and it occurs in the outer reaches of the Rydberg atom, $r \gtrsim 10\ a_0$, where the Rydberg electron resides with near-unity probability, whereas PI (photo-electric effect) is due

to the $\mathbf{A} \cdot \mathbf{p}$-term and occurs in the atomic core, $r \lesssim 10\ a_0$.

The dependence of elastic photon scattering and PI on principal quantum number n also is of interest. The elastic cross section, σ_T, is independent of n. In contrast, the PI cross sections, away from the resonances, have a generic scaling close to $\propto n^{*-3}$, with $n^* = n - \delta_\ell$ denoting the effective quantum number, and δ_ℓ the leading term of the quantum defect. I have verified this scaling in additional calculations (which are not presented in detail).

5.4 Cesium Cross Sections

Figure 5.3 (a) shows partial PI cross sections for Cs $35S$ and $35D$, for the $S \rightarrow P$, $D \rightarrow P$, and $D \rightarrow F$ ionization channels. This figure, which is organized analogous to Fig. 5.2, shows that all three partial PI cross section channels have minima, namely Cooper minima for $S \rightarrow P$ and $D \rightarrow P$, and a shape resonance for $D \rightarrow F$. The PI minima are 100 to 200 nm deeper in the UV than in Rb. The PI cross section of the $35S$ state barely rises above the elastic scattering cross section, σ_T, across the displayed range, making S-type Rydberg atoms of Cs essentially PI-free at all wavelengths shorter than about 500 nm. Otherwise the trends observed in Fig. 5.3 (a) follow those of Rb. As in Rb, in Cs the shape resonance is considerably narrower than the Cooper minima. The Cooper minimum in the $D \rightarrow P$ channel is of little relevance, because in the total PI cross section it will be near-invisible against PI on the $D \rightarrow F$ channel.

The potential curves and free-state wavefunction maps for Cs, shown in Fig 5.3 (b) and Fig 5.3 (c-e), respectively, present a situation that is similar to that in Rb. The Cooper minima in the $S \rightarrow P$ and $D \rightarrow P$ channels have a FWHD of about 100 nm and are characterized by free-state wavefunctions with smooth, λ-dependent phase changes and without any resonant behavior. The $\ell = 3$ potential is the only one that features a relevant barrier, which is located at $r \approx 1\ a_0$ and peaks at 39.2 eV. The potential well inside the barrier bottoms out at -335 eV. The lowest electron "state" in the well is a quasi-bound positive-energy resonance associated with the shape resonance at $\lambda = 150$ nm in the partial PI cross section on the $D \rightarrow F$ channel.

5.5 Experimental Considerations

The PI cross sections warrant an experimental investigation because of the importance of optical traps of Rb and Cs Rydberg atoms in the applications mentioned near the end of Sec. 5.3, where atom loss and decoherence must be avoided. In running these calculations, I find that the model potentials used play a central role in determining the characteristics of the PI cross sections, including the positions of the minima. It is apparent that the positions of the minima are very sensitive to the potentials and the resultant phase shifts and quasi-bound states near and inside

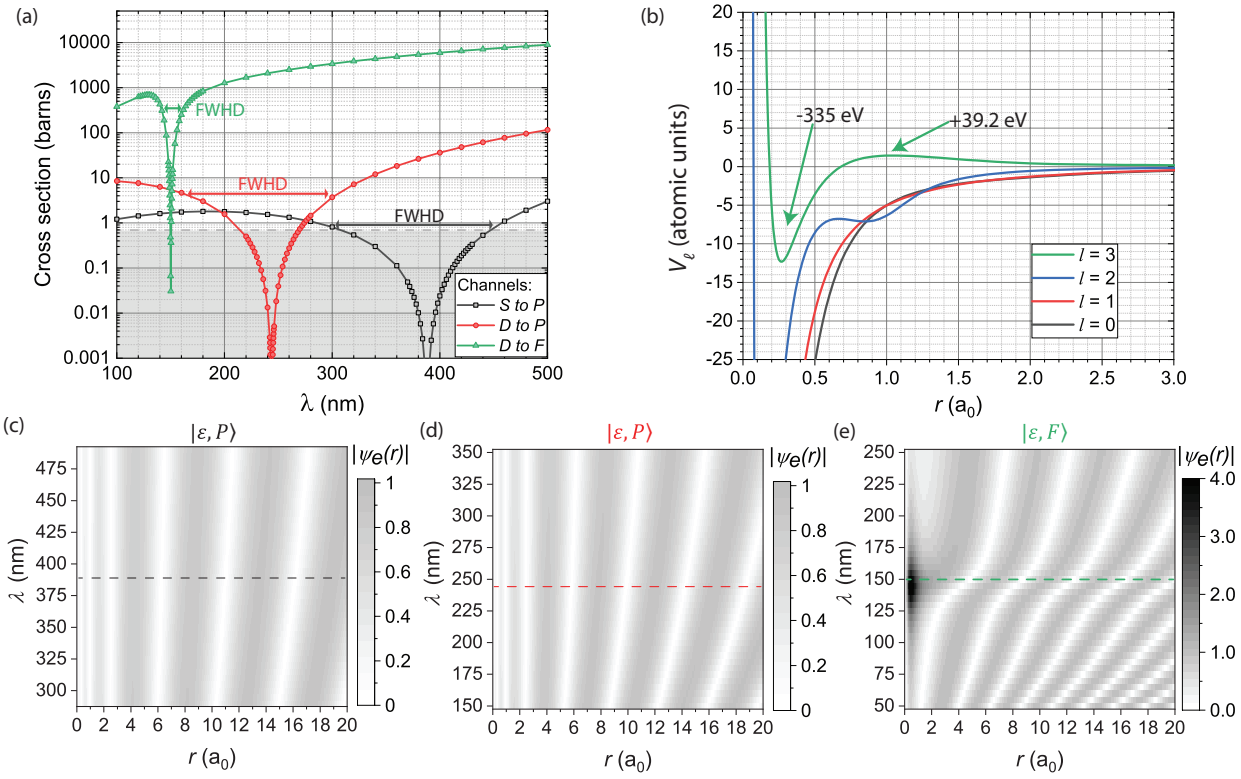

Figure 5.3: Cesium: (a) Partial PI cross sections of $35S$ and $35D$ Cs Rydberg atoms vs PI wavelength λ: $S \rightarrow P$ (black squares), $D \rightarrow P$ (red circles), and $D \rightarrow F$ (green triangles). The Thomson scattering cross section, σ_T, is indicated as in Fig. 5.2. (b) Potential curves $V_\ell(r)$ for $\ell = 0, 1, 2, 3$ in atomic units. (c) P-state free-electron wavefunction vs λ, with the $S \rightarrow P$ Cooper minimum of the PI cross section indicated as a dashed line. (d) Same as (c), with the $D \rightarrow P$ Cooper minimum of the PI cross section indicated as a dashed line. (e) D-state free-electron wavefunction vs λ, with the shape resonance in the $D \rightarrow F$ PI cross section indicated as a dashed line.

the Rydberg atoms' ionic cores. Noting the large depth and the small range of the inner wells of the $\ell = 3$ potentials, one may expect that a measurement of the shape resonances will present a particularly sensitive test for the $\ell = 3$ model potentials.

Considering the widths of the PI minima, one fruitful experimental approach is to use a tunable pulsed laser to photo-ionize a sample of N cold Rydberg atoms and to count the ions using a single-particle counter. The latter may utilize, for instance, a micro-channel plate or a channeltron, which are capable of single-ion counting with efficiencies of $\gtrsim 30\%$. Considering that it will typically be desired to count at least one ion per laser pulse, so as to build up sufficient statistics, but fewer than $\sim N/2$ to avoid saturation, at a given σ the fluence F of the pulse should be in the range

$$\frac{hc}{2\sigma\lambda} \gtrsim F \gtrsim \frac{hc}{N\sigma\lambda} \tag{5.5.1}$$

To measure the shape resonance of $35D$ in Rb, this relation would have to be satisfied for σ ranging between $\sigma_{min} \sim 200$ barn and $\sigma_{max} \sim 10000$ barn, the range of the total PI cross section of that state [see Fig. 5.3 (a)]. For an assumed number of $N = 10^7$ Rydberg atoms, Eq. 5.5.1 translates into

$$\begin{aligned} \frac{hc}{2\sigma_{max}\lambda} &\gtrsim F \gtrsim \frac{hc}{N\sigma_{min}\lambda} \\ 3 \times 10^3 \frac{\mathrm{mJ}}{\mathrm{mm}^2} &\gtrsim F \gtrsim 2.7 \times 10^{-3} \frac{\mathrm{mJ}}{\mathrm{mm}^2} \quad . \end{aligned} \tag{5.5.2}$$

Noting that the PI laser could have an area of several mm^2, it is seen that the pulse fluence F required to measure the shape resonance of Rb $35D$ lies within fairly comfortable limits. A pulse energy of a few tens of μJ per pulse could be sufficient to map out the shape resonances.

To measure the Cooper minimum of Rb $35S$, I set $\sigma_{min} = \sigma_T = 0.67$ barn, the elastic photon scattering rate, and $\sigma_{max} = 20$ barn. In this case, the limiting experimental requirement is

$$F \gtrsim \frac{hc}{N\sigma_{min}\lambda}, \quad \text{or,} \quad F \gtrsim 0.6 \frac{\mathrm{mJ}}{\mathrm{mm}^2} \quad . \tag{5.5.3}$$

It is seen that for a beam with several mm^2 in cross section a pulse energy of a few mJ per pulse could be sufficient to map out the Cooper minimum. This pulse energy could be delivered, for instance, by a nanosecond pulsed dye laser, pumped with a harmonic of a pulsed YAG laser. Noting that with decreasing n the PI cross sections generally increase as n^{*-3}, additional experimental flexibility would be afforded by lowering n.

A main issue with measuring the PI minima is the lasers that would be required to run these experiments. The cesium shape resonance, for example, is centered at 150 nm, which is not an easily accessible wavelength. This wavelength could be reached by running a 600 nm laser through two frequency-doubling crystals, but the setup would be expensive and inefficient.

Additionally, 150 nm light is readily scattered in air, so the laser beam paths must be short to avoid significant beam attenuation.

Of the five PI minima I found, the easiest one to experimentally investigate is the Rb shape resonance (see Eq. 5.5.2). This minimum is centered at 366 nm, which can be accessed by running a pulsed dye laser (PDL) with a dye such as LDS-720, and then sending the PDL beam through a doubling crystal. The Rb and Cs $S \rightarrow P$ Cooper minima are the second-best candidates for measurement because of their accessible wavelengths, but the cross sections expected for these channels are generally low. The resultant condition on the fluence (see Eq. 5.5.3) will make this effort more challenging.

The small total PI cross sections of Rb and Cs nS Rydberg states makes these states ideal for applications of optically excitable, laser-trapped Rydberg atoms. The Cooper minimum in Rb $\bar{\sigma}_{n,\ell=0}^{\epsilon',\ell'=1}(\lambda)$ is near 532 nm, the second harmonic of YAG and similar lasers, which can deliver sufficient power for dipole and optical-lattice traps for Rydberg atoms [106–109]. Laser-trapped, practically PI- and decoherence-free Rydberg atoms can be useful in applications in which atomic decay and decoherence must be minimized, such as in quantum simulation, quantum information processing and high-precision spectroscopy.

5.6 Conclusion

I have calculated the partial PI cross sections of S- and D-type Rydberg atoms of Rb and Cs from the UV into the NIR spectral regime. I identified one Cooper minimum and one shape resonance in Rb, and two Cooper minima and one shape resonance in Cs. Unlike in photon scattering and PI of ground-state atoms by light, the photon energy in PI of Rydberg atoms by light exceeds the electron binding energy by several orders of magnitude, and the atoms are very large compared to the PI wavelength. Similarly unusual energy and size scaling parameters can apply in X-ray PI of regular atoms.

Similar calculations can be performed for any element, as long as there is a model potential to use. In this vein, the same study could be conducted for other alkali metals such as potassium and sodium. While there have been articles in the past that have reported on Cooper minima in these elements, there may be other Cooper minima and shape resonances that are unknown. The studies could also be expanded out of the alkali metal group into other commonly studied species, such as Sr, Yb and Ca, which may have interesting PI behavior due to the presence of two valence electrons. The elastic photon scattering of Rydberg atoms, which has a cross section equivalent to the Thomson scattering cross section, may also deserve a future study.

CHAPTER 6

Magneto-Optical Trap with Divergent Beams

The work discussed in this chapter contains material published in Ref. [110].

The cold plasmas discussed in Chapter 4 were created from atoms trapped in a MOT. This experiment, like the majority of MOT-based experiments, used the standard MOT design: three pairs of counterpropagating laser beams, intersecting at the zero of a magnetic quadrupole field, in free space with no additional structures. This base design, which led to the Nobel Prize in Physics in 1997 [5], is sufficient for the majority of cold atom experiments. That being said, multiple groups have created MOT designs that use the same tangible principles but feature different optical configurations, often for the sake of miniaturization, portability, and/or ease of setup. These include grating MOTs [111, 112], pyramidal MOTs [113–116], low-velocity intense source (LVIS)-MOTs [117], and five-beam MOTs [118]. While implementations of the classic six-beam MOT design suffice for many cold-atom experiments, some applications require electromagnetic boundary conditions that are better defined than what is afforded by the broadly optically accessible structure of a standard MOT.

In this chapter, I discuss a successful realization of a MOT design that uses divergent laser beams. Specifically, the divergent beams were made by sending narrow laser beams through millimeter-sized ball lenses. The conical MOT beams differ from collimated beams in that they exhibit longitudinal intensity gradients and position-dependent $\mathbf{k}$-vectors. Over the course of this chapter, I will discuss the construction and experimental characterization of the MOT setup. I will also present computational analysis that quantifies the effects of divergent MOT beams and highlights the key differences between this setup and a traditional MOT. Finally, I will discuss the practical advantages and disadvantages of this kind of MOT, as well as how this design may be used in future experiments, including plasma studies.

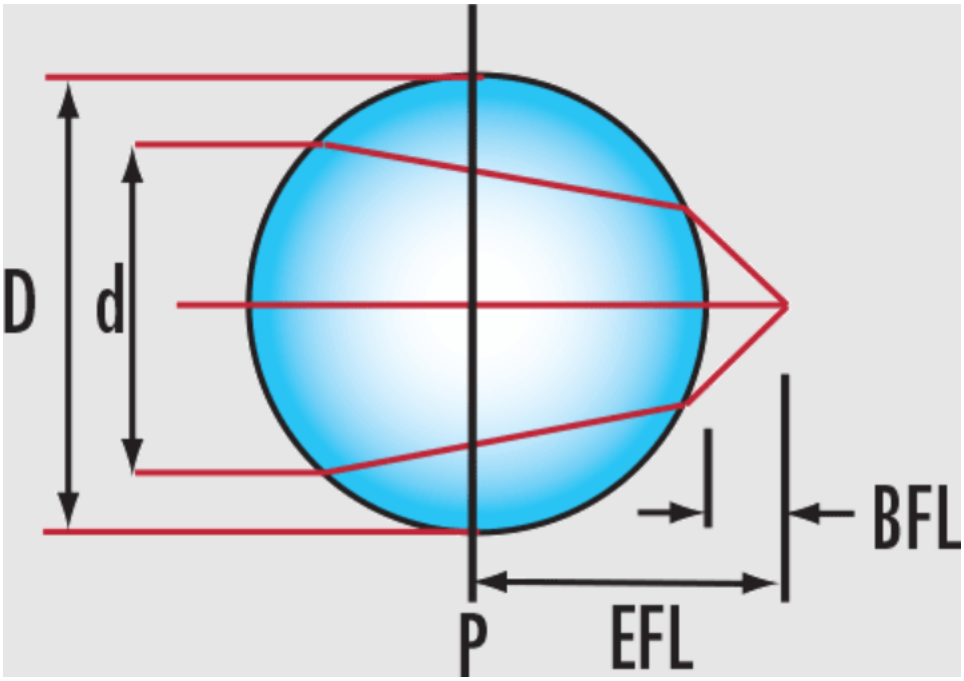

Figure 6.1: Drawing of a ball lens with a collimated beam entering the lens and focusing after it exits. The effective focal length (EFL) and back focal length (BFL) are shown here. Image credit: https://www.edmundoptics.com/knowledge-center/application-notes/optics/understanding-ball-lenses/

6.1 Design

6.1.1 Ball Lenses

As mentioned at the beginning of this chapter, the divergent beams are made with millimeter-sized ball lenses. Ball lenses are different from traditional lenses in that they are completely spherical. They have well-known optical properties [119, 120] and are typically used for fiber coupling and optical tweezers [121, 122]. Notably, ball lenses have short focal lengths. In fact, because ball lenses focus beams so quickly, there are two definitions of focal length that are often used. The effective focal length, or EFL, is the distance from the center of the lens to the focal point. The Back Focal Length, meanwhile, is the distance from the back edge of the lens to the focal point. Figure. 6.1 shows a mock-up of a ball lens with the EFL and BFL labeled.

A ball lens with diameter D and index of refraction n has an EFL of:

$$EFL = \frac{nD}{4(n-1)} \tag{6.1.1}$$

The BFL then is simply the EFL minus the radius of the ball lens:

$$BFL = EFL - \frac{D}{2} \tag{6.1.2}$$

A ball lens made with standard crown glass ($n \sim 1.5$) has an EFL of roughly 75% of its diameter. This means that collimated beams focus and subsequently diverge rapidly after passing through a ball lens. MOTs are typically made with centimeter-sized laser beams, so a millimeter-sized beam sent through a ball lens will expand to a MOT-appropriate size shortly after passing through the ball lens.

The specific model of ball lens used to create this MOT is the Edmund Optics #43-709. This ball lens is made from N-BK7 glass and has diameter of 1.5 mm and focal length of 1.1 mm. Figure 6.2 shows the results of a ray tracing simulation done in Zemax OpticStudio with this exact model ball lens. The beam profiles are observed 9.5 mm away from the center of the ball lens. The simulation results demonstrate that ball lenses have short focal lengths, and that collimated beams sent into these lenses quickly focus before diverging. The simulation also shows how input angle affects the shape and location of the divergent light cone. In Fig. 6.2, the green and red rays represent beams with incident angles of ± 45 degrees respectively. The simulation shows that sending in beams at an angle results in distortion of the beam shape, as well as displacement of the beam from the center.

One way in which the ball lens MOT immediately differs from the classic design is the number of unique laser beams required for operation. Both designs require six beams, but the traditional design usually only has three unique beams. Because the traditional MOT uses collimated beams, each beam can be sent through the trap center, reflected off a mirror, and sent back through the trap, creating a counter-propagating pair. This retro-reflection technique is not possible with diverging beams, so the ball lens design requires six unique beams, one for each lens.

6.1.2 Experimental Setup

The centerpiece of the experimental setup is a structure called the BLOB. The BLOB is a hollow steel cube that holds the ball lenses in place and houses the MOT trap center. It was made with spot welded sheets of 1.6 mm thick steel, and it has inner side length of 16 mm. Each face of the cube has counterbores with inner and outer diameters of 1.3 mm and 2.0 mm, respectively. The ball lenses sit in the 2.0 mm holes, which have a depth of 0.5 mm, and are held in place with flaps made of steel shim shock. The flaps have 1.3 mm diameter holes overtop the ball lenses that allow the laser beams to pass through. The cube also has several 4 mm holes on its faces and edges for observing the MOT. Figure 6.3 shows computer illustrations of the BLOB and laser beams, along with a picture of the actual part.

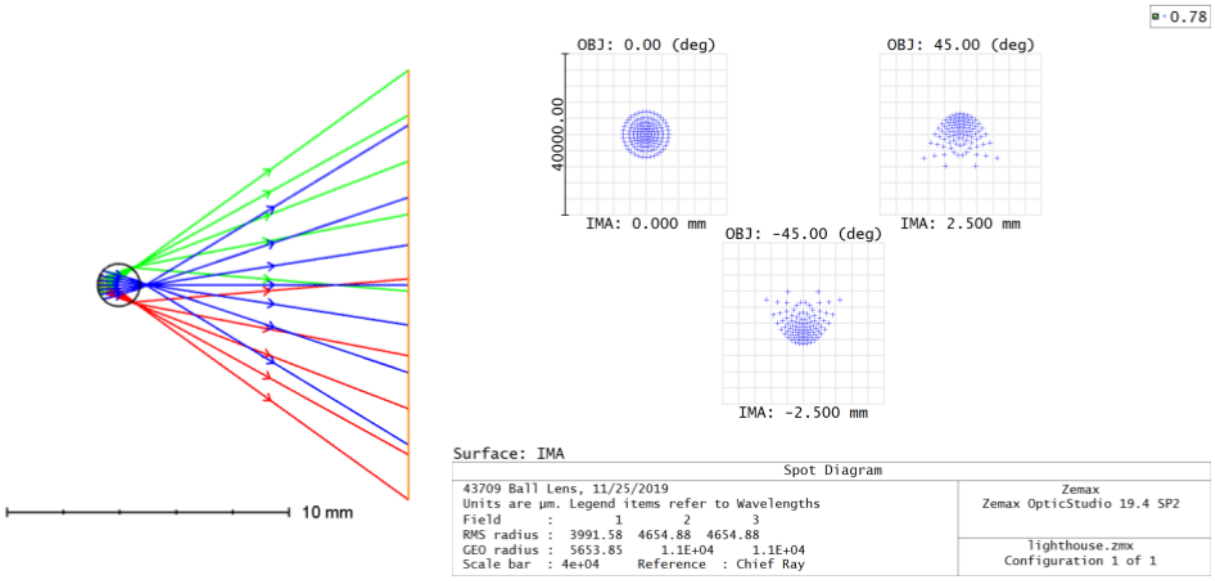

Figure 6.2: Ray tracing analysis of a 1.5 mm N-BK7 ball lens, done in Zemax OpticStudio. Three Gaussian beams with wavelength of 780 nm and waist of 1 mm are sent into the lens at 0 and ± 45 degrees. The beam profiles are observed at a distance of 9.5 mm from the center of the lens; the observation plane is denoted by the orange line. The profiles show that the ball lens cause the incident beams to diverge rapidly, and that the shape and orientation of the divergent light cone depends on the incident angle of the beam. Thus, in order to make a MOT with ball lenses, it is critical that all the cooling beams enter the ball lenses at 0 degrees.

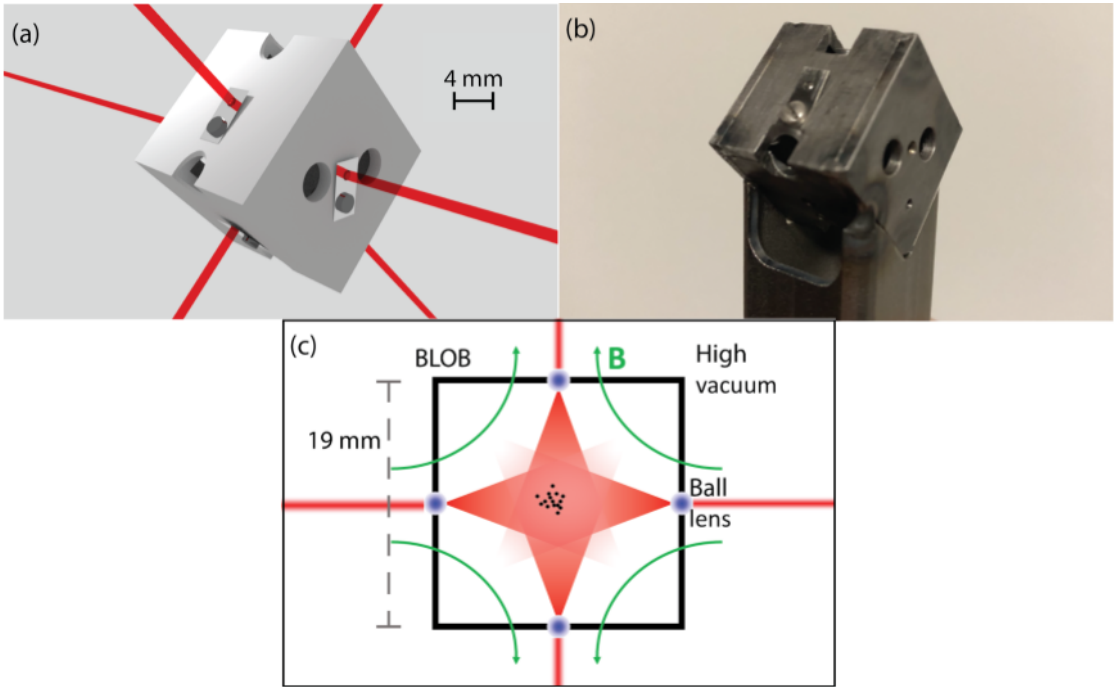

Figure 6.3: (a) Computer rendering of the ball-lens MOT design, including the incident cooling beams. The ball lenses are located at the centers of the cube faces. The larger holes are for additional optical access. (b) Picture of the physical ball-lens optical box (BLOB). The right-facing side shows the exposed milled holes before insertion of a ball lens, while the upward-facing side shows an installed ball lens and retaining flap. (c) Cross-sectional sketch of fields within the ball-lens MOT.

In addition to holding the ball lenses in place, the BLOB provides some additional features not included in the traditional MOT design. For one thing, because the MOT center is encased within a metal box, the trapped atoms are Faraday-shielded from external electric fields. This feature is relatively unimportant for neutral atoms, but it greatly aids ions and plasmas, which are sensitive to stray electric fields. This design also gives protection from blackbody radiation, unlike traditional MOTs which are in free space and exposed to blackbody radiation. This feature would be especially useful for precision measurements and atomic clock experiments, which seek to minimize blackbody perturbations. Lastly, the interior of the enclosed structure can be outfitted with electrodes or other structures that can establish fields and boundary conditions. These electrodes could be used for cold-atom-loaded Penning and Paul traps, among other uses.

The BLOB is welded to a piece of square tubing which holds it at the right height in the vacuum chamber. This square tube is held in place with aluminum rings that fit in place with the chamber wall and also provide electrical contact for grounding. The BLOB fits snugly between two large-diameter re-entrant vacuum windows. Before installation, the BLOB and other metal parts were washed with a chemical solution to remove fingerprints, machine oil, and other impurities. Then, after installation, the chamber was baked out and pumped down to a pressure of approximately 10^{-8} Torr.

6.2 Experimental Implementation

6.2.1 MOT Transition

The ball-lens MOT is tested with ^{85}Rb. Either isotope of rubidium could have been trapped and cooled, but ^{85}Rb was chosen because of its higher natural abundance. The MOT beams have a wavelength of 780 nm and are detuned from the $5S_{1/2}\ F = 3 \rightarrow 5P_{3/2}\ F' = 4$ hyperfine cycling transition by -14 MHz, with an uncertainty on the order of 1 MHz. The power of each of the six cooling beams before entering the vacuum chamber is $\lesssim 5$ mW. With the above value of w_B, the upper limit of the peak intensity of the individual beams at the MOT center is $\sim 12\ I_{sat}$ (the saturation intensity $I_{sat} = 1.6$ mW/cm^2 for the MOT cycling transition [123]). The true intensity is slightly less due to reflection and other losses (such as Rb absorption and possible beam clipping). Density images of the atom cloud in the MOT are obtained with a collimated MOT probe laser resonant with the $F = 3 \rightarrow F' = 4$ transition (FWHM of 2.5 mm and center intensity 0.23 mW/cm^2). The probe beam is directed through the center of the BLOB and the emerging output beam aligned into a CCD camera (Pixelfly Model 270 XS). The camera is used to take both shadow images with the probe beam on and MOT beams off, and fluorescence images with the probe beam off and MOT beams on. An additional camera, mounted on an axis perpendicular to that of the Pixelfly camera, is used to ensure that the trapped-atom cloud is approximately

spherical.

6.2.2 Atom Count and Number Density

The atom number, the most important metric in our comparison with our theoretical model in Sec. 6.3, and the number density of the MOT are measured using shadow imaging (also known as absorption imaging). In this configuration, the MOT cooling beams are briefly turned off, and a probe beam pulse is sent through the MOT and into the Pixelfly camera. The MOT and probe beams are switched with acousto-optic modulators (AOMs).

Three images are required for calculating atom count: a shadow image with the MOT atoms present, an image with the probe beam on but without MOT atoms, and a background image with the probe off but all other light sources left on. Once these are obtained, the atom number in the MOT, $N_{MOT,Exp}$, is found by evaluating the following integral:

$$N_{MOT,Exp} = \int \frac{1}{\sigma} \ln\left(\frac{I_0(x,y) - I_B(x,y)}{I(x,y) - I_B(x,y)}\right) dxdy \tag{6.2.1}$$

This integral is done over the MOT object plane. $I(x,y)$, $I_0(x,y)$, and $I_B(x,y)$ represent the MOT on, MOT off, and background images respectively. Since the probe light is unpolarized and the MOT magnetic field is left on, we use the isotropic absorption cross section $\sigma = 1.246 \times 10^{-9}$ cm^2 [123]. The integral is evaluated as a discrete sum over a two-dimensional array of CCD pixels, with the pixel area given by the CCD pixel area projected into the object (MOT) plane.

Figure 6.4(a) shows an area-density shadow image for a MOT single-beam intensity of $I \approx 8.5$ mW/cm^2 (5.1 I_{sat}), and Fig. 6.4(b) shows the corresponding timing details. With the probe beam carefully tuned on-resonance to the ^{85}Rb MOT cooling transition, we find the atom number in our MOT to be $N_{MOT,Exp} = 4.2 \times 10^5$. Assuming that the MOT fills a cubic volume with a side length of 0.5 mm, the typical linear size of the MOT observed with both of our perpendicularly mounted cameras, the atom density in the MOT is estimated to be 3.2×10^9 atoms/cm^3.

6.2.3 Loading Time

The loading time, required for calibration of the theoretical atom-number estimate in Sec. 6.3, is determined with fluorescence imaging. In this configuration, the MOT light is periodically switched on for 4.0 s to allow the trap to accumulate atoms, and then off for 1.0 s to empty the trap. The camera records images of the atom cloud, with exposure times of 10 ms and camera-gate starting times of $\tau_i = i \times 0.25$ s relative to the turn-on of the MOT light ($i = 0, 1, ..., 12$).

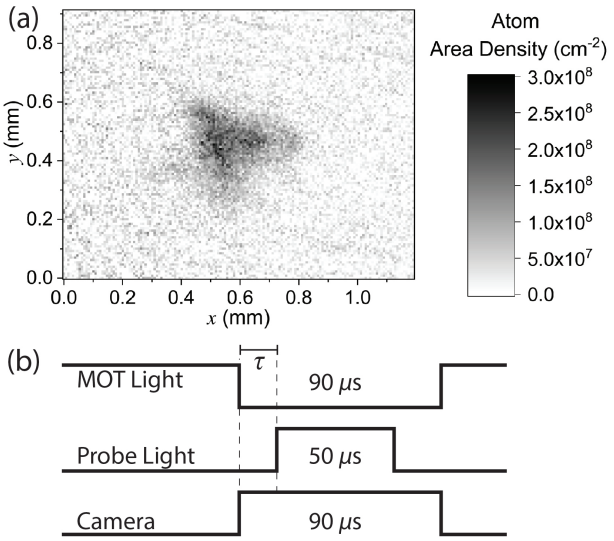

Figure 6.4: (a) A shadow image of the MOT showing area density (the integrand in Eq. 6.2.1) versus position in the MOT plane. (b) Timing diagram for the shadow imaging. When the MOT light is turned off, the camera is gated on for 90 μs. Following a wait time of $\tau = 20$ μs after the MOT light is turned off, the probe pulse is turned on for a duration of 50 μs.

Figure 6.5(a) shows a fluorescence image of the atom cloud after 3.0 s of loading, along with a timing diagram in Fig. 6.5(b) for the fluorescence imaging procedure. In our analysis, we fit the background-subtracted fluorescence images with two-dimensional Gaussians, whose pixel-sum areas are taken to be proportional to atom number. The conversion factor from pixel sum to atom count is obtained as follows. A collimated, 780-nm test laser test beam (power 1.134 nW) is passed in its entirety through the camera lens and is imaged into an out-of-focus, non-saturated disk with a diameter on the order of that of the MOT. The pixel sum of the test-beam image then corresponds to 1.134 nW, allowing us to convert MOT-image pixel sums into light power radiated from the MOT. The given camera geometry (lens aperture and distance from the MOT), the photon energy at 780 nm, and the photon scattering rate per atom in the MOT, $\gamma = 10^7$ s^{-1} (known from the model results in Sec. 6.3), then allow us to convert fluorescence into an atom count. I estimate the calibration uncertainty to be 30% due to the uncertainty in γ and in the geometrical parameters. The uncertainty in γ arises from the detuning uncertainty (a few MHz). I note that shadow imaging with a low-intensity, on-resonant probe beam (see Fig. 6.4) results in a more accurate atom count.

Figure 6.5(c) presents atom count obtained from fluorescence images versus loading time, along with error bars from the fits which represent the statistical error (the uncertainty of the fluorescence-to-atom-count scaling is not included). Applying an exponential rise time fit to the data gives a time constant of 1.3 ± 0.1 s. The residuals between the data and the fit can be attributed to the effects of intensity and frequency fluctuations of the cooling laser on the experimental data. The vacuum chamber pressure as read from the ion pump attached to the chamber is 10^{-8} Torr.

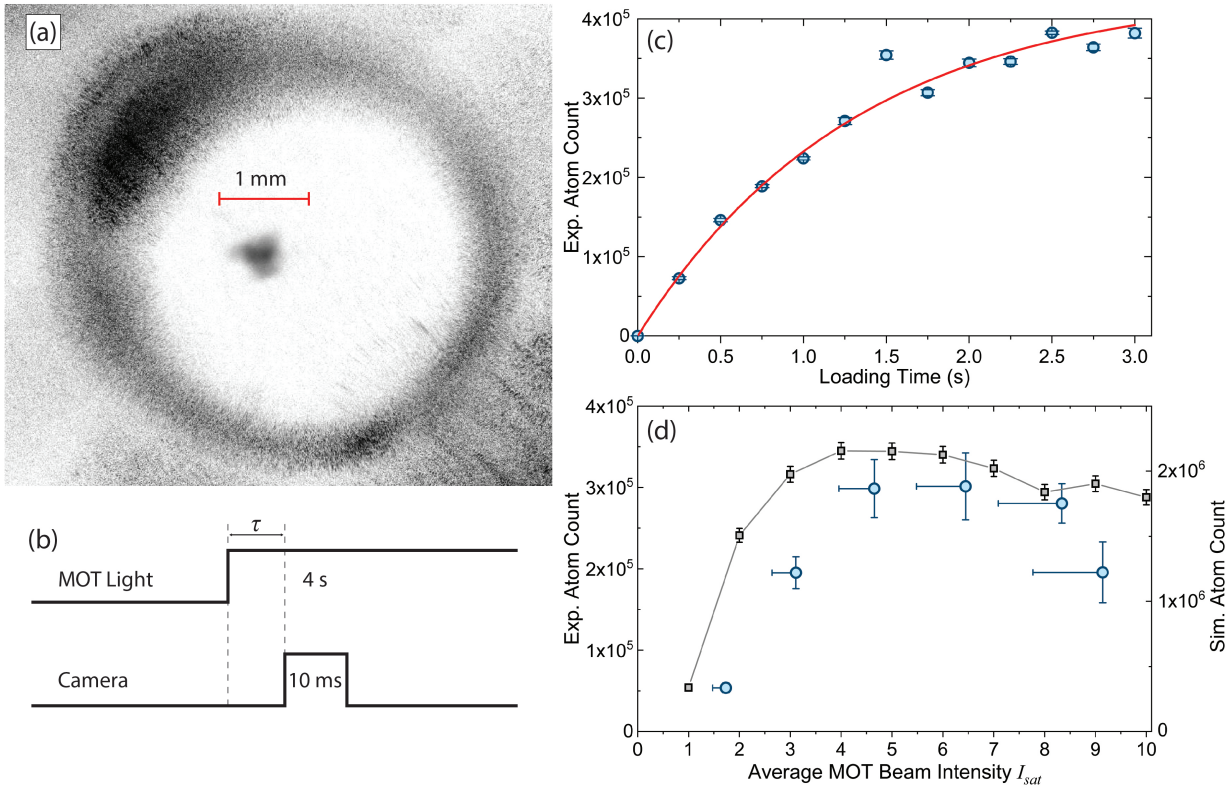

Figure 6.5: (a) Inverted fluorescence image of the MOT taken through one of the 4.0 mm viewports in the BLOB with length scale bar. (b) Timing diagram for the loading time measurements. The loading time τ is stepped in units of 0.25 s, and the camera exposure time is 10 ms. (c) Atom count versus loading time. Applying an exponential fit to the data yields a time constant of 1.3 ± 0.1 seconds. The atom count scales linearly with trap fluorescence. (d) Measured trap atom count (left axis, circles) and simulated trapped-atom number (right axis, linked squares) versus central single-beam intensity at the trap center location. The asymmetric horizontal error bars reflect a potential 15% reduction of beam intensity due to reflection and other losses, while the vertical error bars are the standard deviations of the data sets for each beam intensity. The variance in MOT atom counts is due to shot noise as well as non-statistical fluctuations such as radiation pressure effects.

The observed loading time is in line with values observed in conventional MOTs at that pressure.

6.2.4 Atom Count vs. MOT Beam Intensity

In the performance evaluation of this MOT, I have also studied the dependence of atom number on MOT beam intensity. Fig. 3(d) shows the atom count versus central beam intensity. The result indicates an optimal trap performance at an intensity of $\sim 6I_{sat}$; at higher intensities the atom number drops. This behavior contrasts with standard six-beam MOTs, in which the atom number keeps increasing to considerably higher intensities before reaching a plateau. The peculiar intensity dependence of the ball-lens MOT is reproduced by the model, as shown by the simulated data in Fig. 6.5(d). The simulated data are for $d = 7.5$ mm, MOT detuning of -15 MHz, a MOT

magnetic-field gradient of 15 Gauss/cm along the field's symmetry axis, and MOT beam diameter of 6 mm (FWHM of the intensity). The model is described in the following section.

6.3 Computer Simulation of Divergent Beam MOT

6.3.1 Overview

The objective of the model is to determine the dependence of the number of captured atoms in steady state on ball-lens MOT parameters. The model also reveals how the atom capture behavior differs from that of a standard six-beam MOT, and how that translates into differences in the steady-state trapped-atom number and into guidelines for best operating conditions for ball-lens MOTs.

The capture efficiency is studied by simulating atom trajectories that are propagated with a fourth order Runge-Kutta algorithm, where the six diverging ball-lens MOT beams give a spatially-varying radiation pressure. In addition to the usual transverse intensity variations in the beams, we also account for the longitudinal intensity gradients and the variation of the $\mathbf{k}$-vectors within the individual, highly divergent beams. The model establishes a spherical MOT cell volume at the center of the six beams of radius $R = 1.0$ cm, which has a volume similar to that of the BLOB used in the experiment. Thermal atoms are generated at a fixed rate F_{Sim} on the cell surface with fixed radial coordinate R and random polar and azimuthal angles (θ_0, ϕ_0), with the coordinate system defined by the magnetic-field symmetry axis ($\hat{\mathbf{z}}$) and the axes of the cooling beams. The inward velocity distribution is known from gas kinetics,

$$P(v, \theta, \phi) = \frac{1}{\pi} P(v) \sin(\theta) \cos(\theta) \tag{6.3.1}$$

with a normalized effusive Maxwell distribution $P(v)$ and spherical angular coordinates relative to the normal of the impingement surface (which depends on the position angles (θ_0, ϕ_0) of the atom). The trajectories of these atoms are propagated using the fourth order Runge-Kutta routine mentioned earlier, and time-incremented atom positions are tracked until the atoms either exit the simulation volume or suffer a collision with a fast background atom. The trapped atoms are counted and their phase-space parameters are recorded at user-defined times.

The MOT parameters for the simulation in Fig. 6.6 include a MOT magnetic field gradient of 15 G/cm along the field axis and a laser detuning of -15 MHz from the MOT transition, corresponding to typical Rb MOTs and close to our experimental value. We vary the distance d of the ball-lens focal spots from the MOT center from 6 mm to 50 mm. To study the transition between a regular and the ball-lens MOT, we assume that the transverse intensity distributions

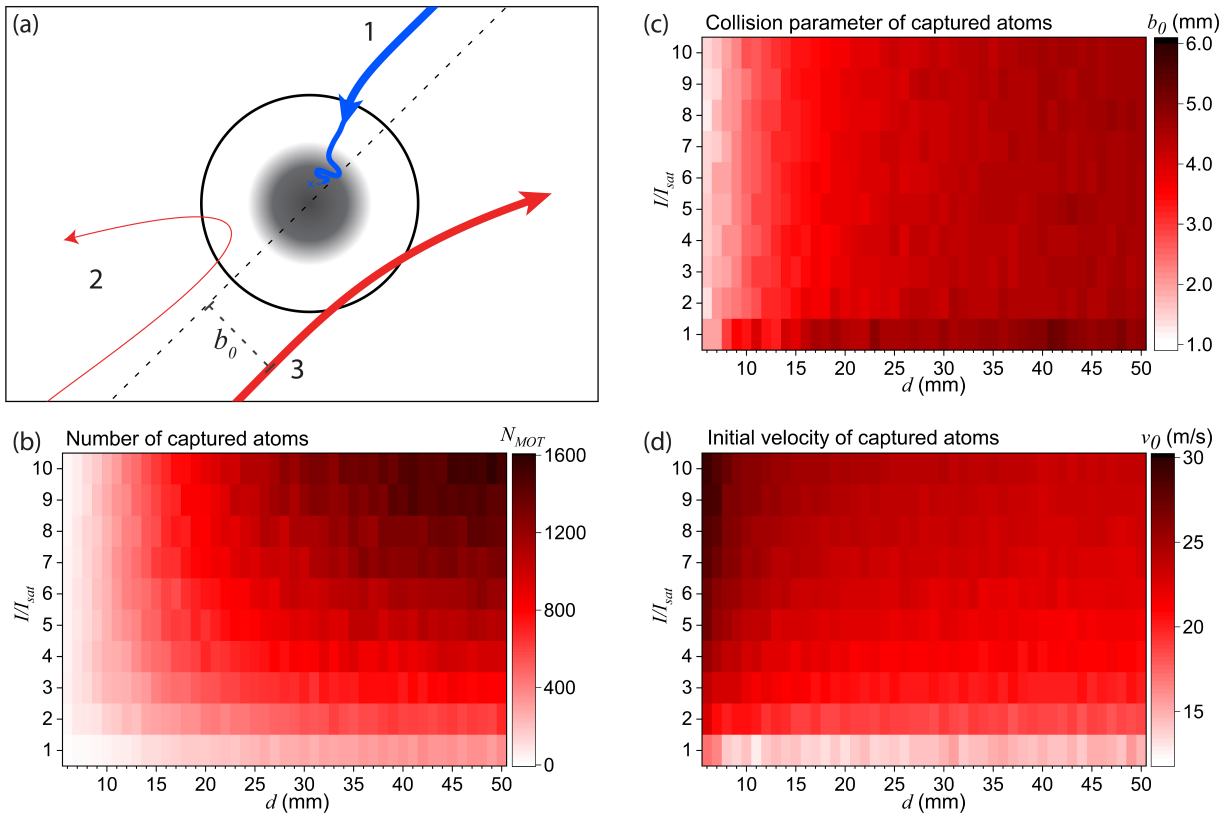

Figure 6.6: (a) Depiction of three atom trajectories. The relative speeds of the atoms are indicated by the thickness of the arrows. Atom 1 is successfully trapped in the MOT. Atom 2 is not trapped because it is moving too slowly, and atom 3 is not trapped because its collision parameter b_0 is too large. (b) The number of trapped atoms vs distance d of the ball lenses from the MOT center and I/I_{sat}. (c) Root-mean-square (RMS) value of the incident collision parameters b_0 of the captured atoms vs d and I/I_{sat}. (d) RMS value of the incident speed v_0 of the captured atoms vs d and I/I_{sat}.

of the beams are Gaussians with a *fixed, d-independent* FWHM of 6 mm at the MOT center, as measured for the ball lenses used in the experiment. The FWHM of the beams are proportional to the distance from their respective focal spots. For large d, the system approaches a regular 6-beam MOT with near-zero-NA, collimated beams. As d is reduced, the MOT gradually transitions into a ball-lens MOT with large-NA beams. The smaller d, the more the divergence and the longitudinal intensity gradient of the MOT-beam light cones affect MOT performance. Here we restrict ourselves to the case that all six optical axes pass through the center of the MOT, and that all lenses have the same distance from the MOT center.

For each set of parameters we evaluate the trajectories of 10^7 to 10^8 thermal atoms impinging into the MOT region. Every atom that enters gets tagged with its initial speed v_0 and collision parameter b_0 relative to the MOT center (see Fig. 6.6(a)). Most atoms do not become trapped (red trajectories), while some do (blue trajectory). Any atom whose speed drops below 1 m/s, within 2 mm from the MOT center, is considered trapped. We have verified that the exact

values of these trapping criteria are not important. We log the RMS velocity and RMS radius of the trapped-atom cloud in the MOT, the trapped-atom number, the average photon scattering rate of the atoms, and the RMS values of the initial speed v_0 and collision parameter b_0 of the atoms that become trapped.

6.3.2 Survey of Relative Performance

In Fig. 6.6, we present a survey of ball-lens MOT performance as a function of ball-lens focal-spot distance d and single-beam peak intensity I at the MOT center. In the simulation, the MOT loads for 0.9 s, the half-life for the collision time constant of 1.3 s measured in the experiment. The simulated impingement flux into the MOT cell, F_{Sim}, is taken to be 50 atoms per μs. (The trapping results can be scaled up to the actual impingement flux; see Eq. 6.3.2 below.) Figure 6.6(a) shows a diagram of typical atom trajectories in the MOT, two of which fail and one which is successful in becoming trapped. Figure 6.6(b) displays the number of captured atoms N_{MOT} vs d and I/I_{Sat}. From this simulation it is determined that in the experiment we are operating the MOT near the lower bound in d at which the ball-lens MOT becomes viable. At $d \lesssim 7$ mm the ball-lens MOT does not capture experimentally useful numbers of atoms. The usual six-beam MOT with collimated beams is near-equivalent with the right margins in Figs. 6.6(b)-(d), where $d = 50$ mm. The numerical data show that, at -15 MHz MOT detuning and other parameters as stated, our $d \approx 8$ mm ball-lens MOT captures approximately 6% to 14% of the number of atoms one would find in a regular six-beam MOT, with the highest ratio at $I = 4I_{sat}$. It is also noted that at small d-values the performance is best at lower intensities and degrades at high intensities. This accords with the trend measured in Fig. 6.5(d). For completeness we also report that the temperature of the trapped atoms is, universally for all cases in Fig. 6.6, near the Doppler limit (here 150 μK), and the diameter of the trapped-atom cloud near 0.25 mm.

In Fig. 6.6(c) it is seen that the RMS incident collision parameter b_0 of the trapped atoms drops from about 5 mm for the regular MOT ($d = 50$ mm) to about 1.5 mm for the case of extremely divergent beams ($d = 6$ mm), with a minor variation as a function of intensity. Figure 6.6(d) shows that for the standard MOT ($d = 50$ mm) the RMS capture velocity ranges between 15 m/s at low and 25 m/s at high intensity; this range generally is as expected. Interestingly, for extremely divergent beams ($d \lesssim 8$ mm) the RMS capture velocities increase to about 17 m/s at low and 30 m/s at high intensity.

To further exhibit the trapping behavior in MOTs with highly divergent beams, we have performed a study in which both the collision parameter, b_0, and the incident velocity, v_0, are kept fixed, while the polar and azimuthal angles of approach of the incident atoms relative to the z-axis, θ_{inc} and ϕ_{inc}, are chosen randomly. The results shown in Fig. 6.7 demonstrate that in the MOT with highly divergent laser beams, atoms with incident velocities $v_0 \lesssim 18$ m/s become repelled

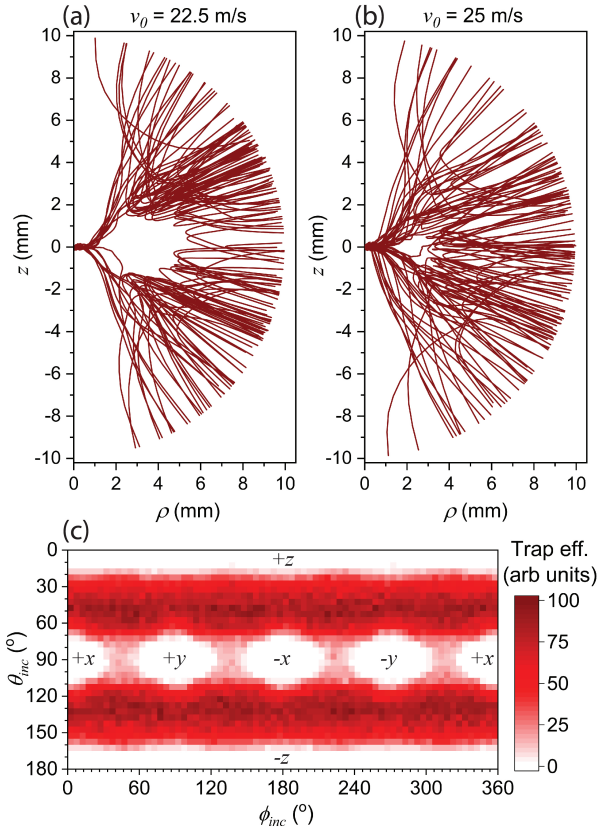

Figure 6.7: (a) and (b) Trajectory samples in cylindrical coordinates for $I = 6I_{sat}$, $d = 7$ mm, $b_0 = 1$ mm, MOT detuning of -15 MHz, and initial speeds of $v_0 = 22.5$ m/s and $v_0 = 25.0$ m/s respectively. Many trajectories that are strongly curved are associated with repulsion by radiation pressure, while trajectories that are approximately straight and end at the origin show trapping events. (c) Statistics of trapped-atom counts vs polar and azimuthal angles of approach, θ_{inc} and ϕ_{inc}, of the incident atoms, for the same parameters as in (b) and on a linear scale. The angular regions of no trapping (white) correspond with the directions of the MOT laser beams, indicated by coordinate axis labels.

and are not trapped due to radiation pressure. Atoms that do become trapped have velocities $v_0 \sim 25$ m/s and collision parameters $b_0 \lesssim 2$ mm. The trapping behavior as a function of angle of approach of the impinging atoms, θ_{inc} and ϕ_{inc}, displayed in Fig. 6.7(c), further shows that atoms approaching from directions that are in-between the MOT laser-beam directions have a much higher chance for trapping than atoms approaching from a direction that is close to one of the MOT-beam directions (see beam labels in Fig. 6.7(c)).

The above described features starkly differ from the case of a regular MOT, in which practically all atoms with $v_0 \lesssim 30$ m/s and $b_0 \lesssim 6$ mm are collected. The contrast in trapping behavior of MOTs with highly divergent and regular MOTs with collimated beams is shown quantitatively in Fig. 6.8, where we display the relative capture efficiencies versus b_0 and v_0 for the cases $d = 7$ mm (MOT with highly divergent beams) and $d = 50$ mm (near-ideal regular MOT). While both MOTs are capturing atoms up to about 30 m/s, the MOT with highly divergent

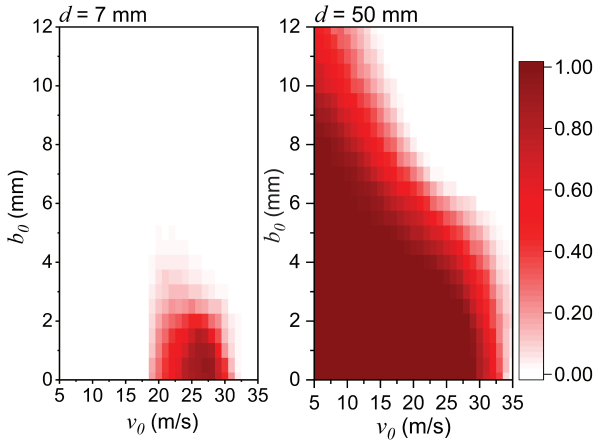

Figure 6.8: Probability of trapping on the indicated linear scale averaged over θ_{inc} and ϕ_{inc} vs incident atom velocity v_0 and collision parameter b_0 for a highly-divergent ball-lens MOT with $d = 7$ mm (left) and for an essentially regular MOT with $d = 50$ mm (right).

beams fails to capture slow atoms and atoms with collision parameters larger than about 2 mm. This behavior is due to repulsive radiation pressure at distances larger than about 2 mm (see Fig. 6.7).

6.3.3 Quantitative Model for Trapped Atom Number

Next we perform an order-of-magnitude comparison between experimentally observed and simulated trapped-atom numbers. The Rb vapor pressure inside the BLOB is assumed to be negligible; the atoms to be trapped impinge from the larger vacuum chamber ("outer vacuum chamber") via the apertures into the interior of the BLOB. The atom flux impinging from the outer vacuum chamber into the BLOB cell is given by $F_{Exp} = (A/4)n_V\bar{v}$, where A is the surface area of the cell that is exposed to impinging thermal atoms, n_V is the vapor volume density in the outer vacuum chamber, and $\bar{v} = \sqrt{8k_bT/(\pi M)}$ with vapor temperature $T = 293$ K and atom mass $M = 85$ amu is the average thermal speed. It is invalid to set n_V equal to the room-temperature equilibrium density of Rb, because the outer vacuum chamber is not saturated with Rb vapor. For a good comparison it is essential to perform an in-situ reference absorption measurement, from which n_V is inferred. For the necessary calibration of n_V, we have performed a reference absorption measurement with a Gaussian-profile test beam diameter < 1 mm (central intensity 11 mW/cm^2, tuned to the MOT transition) propagating through a 40-cm-long segment of the outer vacuum chamber, with the MOT magnetic field off. The observed absorption was $3.6 \pm 0.2\%$. Using a calculation described in Appendix , we find $n_V = 6.3 \times 10^{13}$ m^{-3}, which yields an experimental impingement flux $F_{Exp} = A\bar{v}n_V/4 = 4.3 \times 10^{11}$ s^{-1}.

In the simulation, the impingement flux into the MOT cell is assumed to be $F_{Sim} = 5 \times 10^7$ s^{-1}. Therefore, if the simulation shows a trapped-atom number $N_{MOT,Sim}$, the number of

trapped atoms expected for our experiment is

$$N_{MOT,Exp} = N_{MOT,Sim}\frac{F_{Exp}}{F_{Sim}} = 8600 N_{MOT,Sim} \tag{6.3.2}$$

We have run the simulation for a best estimate of our experimental conditions ($d = 7.5$ mm, beam FWHM of 6 mm, MOT decay time of 1.3 s, magnetic-field gradient along the field axis 15 G/cm). Over the parameter ranges and step sizes investigated in our simulations, best performance is seen for a MOT detuning of about -15 MHz and $I = 6I_{sat}$. Under these conditions, the simulated steady-state atom number is 220$\pm$4. The theoretically predicted value for the trapped atom number then becomes $N_{MOT,Sim} = 1.9 \times 10^6$. This number can be compared with the number of MOT atoms we have experimentally observed under good conditions, $N_{MOT,Exp} = 4.2 \times 10^5$.

6.4 Discussion

The picture that emerges from the combined results of the survey study is that ball-lens MOTs with highly divergent trapping beams ($d \lesssim 8$ mm, $NA \gtrsim 0.3$), only capture atoms that are pointing towards an "active" trapping center that is about 4 mm across (gray region in Fig. 6.6(a)). Atoms traversing through an outer belt of radiation pressure, ranging in diameter from about 4 mm to the outer reaches of the trapping beams, become blown out on their approach towards the MOT center (trajectory 3 in Fig. 6.6(a)). Ball-lens MOTs with highly divergent trapping beams therefore only captures atoms with velocities between 20 m/s and 30 m/s and collision parameters less than about 2 mm. It is particularly noteworthy that atoms slower than about 15 m/s and with collision parameters less than about 2 mm do not become trapped (trajectory 2 in Fig. 6.6(a)). For an atom to become trapped it has to be fast enough that its inertia carries it through the outer belt of radiation pressure, slow enough that it becomes trapped within the inner region of "good" radiation pressure, and the trajectory of the incident atom also has to point at the center of the MOT to within about 2 mm tolerance. In Fig. 6.6(a) only trajectory 1 meets all criteria.

The agreement between experimental and simulated trapped-atom numbers is within about a factor of four. Four of the eight 4-mm holes on the BLOB have a small clearance from the glass windows, which are part of the outer vacuum chamber, and one window is hidden in the BLOB's support tube. The accessible opening of the BLOB where Rb may effuse is only $3/8 = 1/2.7$ of the area assumed in comparison, leaving a disagreement in trapped-atom number of less than a factor of two. The remaining disagreement may, in part, be attributed to Rb vapor density variations near the BLOB caused by the complex molecular streaming behavior of the Rb vapor from the source, which is attached to the outer vacuum chamber, to the BLOB region. The ball-lens MOT's atom collection efficiency could also be reduced by MOT beam aberrations and imperfec-

tions that we are not able to quantify, but that are usually present in most MOT setups. Finally, there may be a small difference between the assumed $J = 0 \rightarrow J' = 1$ MOT transition and the actual ^{85}Rb $F = 3 \rightarrow F' = 4$ transition in terms of trapping efficiency. Studies into the detailed origins of the remaining factor of two of unaccounted-for disagreement are outside the scope of the present study. Regardless, we are confident that we have captured the essential physical principles of the ball-lens MOT, and that our work presents a valuable guide for research elsewhere towards implementation of this design.

6.5 Conclusion

This investigation marks the first ever reported case of a MOT made with highly-diverging laser beams made with ball lenses. Additionally, the kinetic model developed alongside the experiment does a good job of illustrating the physics of laser cooling and trapping with divergent light fields. Simulated results are in good agreement with our experimental observations and parametrize the range over which this MOT should work well.

While this design of the BLOB was successful in forming a MOT, there are several changes that should be implemented in subsequent versions. The simulations indicate that the ball-lens focal-spot distance d from the trap center was near the lower edge of viability. This distance, and the BLOB geometry for that matter, were limited by the vacuum chamber used for this experiment, and it was a stroke of luck that this distance happened to be just at the lower bound of functionality. In view of Fig. 6.6, in applications one might want to use d-values in the range of 2 cm, where the BLOB dimension is still conveniently small and the atom number is $\gtrsim 50\%$ of that of a similar-sized standard six-beam MOT.

I would be remiss if I did not mention the disadvantages of this MOT design. Unlike standard designs, it is difficult to counter-align the beams that lie along the same axis, making the initial alignment more difficult. Due to the dependence of the central intensity in the MOT region on the incident angle on the ball lens, the setup has a higher sensitivity to relative beam powers than a standard MOT. Nevertheless, once I observed trapped atoms within the ball-lens MOT, the design provided a sizable range of stability over both the relative beam powers and angles of incidence for each ball lens.

CHAPTER 7

Conclusion and Outlook

The work presented in Chapters 4-6 has laid the groundwork for many potential experiments in the coming years. In this chapter, I will discuss some of these experiments. I will also discuss some of the other projects I am involved with that were not related to the material in Chapters 4-6.

7.1 Plasma Expansion and Ion Imaging Studies

The rubidium ion imaging setup described in Chapter 4 can accommodate a myriad of plasma expansion and ion imaging experiments in addition to the non-neutral plasma expansion experiment discussed earlier. The next logical step would be to run the same experiment with neutral plasma instead of non-neutral plasma. This can be done by simply replacing the current ionization laser (pulsed, frequency-tripled, 355 nm Nd:YAG) with a pulsed laser operating at a near-threshold wavelength ($\sim$479.1 nm), such as a PDL. As it turns out, the laboratory owns two PDLs that can be filled with an appropriate dye like Coumarin 480 and used as the ionization laser. Figure 7.1 shows one of the PDLs running with Coumarin 480 dye. Coumarin 480 needs to be pumped with a 355 nm pulsed laser, which conveniently is what I currently have in place as the ionization laser. Switching to neutral plasma studies is a matter of integrating a PDL into the current setup, redirecting the 355 nm beam into the dye laser for pumping, and sending the resulting 479.1 nm beam into the chamber along the same beam path. This would take a non-trivial amount of work, but it would not be arduous. In fact, it is possible to create a beam path with an re-directable 355 nm beam that would allow the user to easily change the plasma from non-neutral to neutral and back on the fly.

The ionizing PDL can be further fine-tuned by using a technique called injection locking. Most PDLs use a mechanical grating oscillator to set the wavelength. These oscillators allow for a wide range of wavelengths and quick adjustment, but the downside is that the laser has a wide bandwidth, on the order of 30 GHz. Injection locking a PDL, meanwhile, involves removing

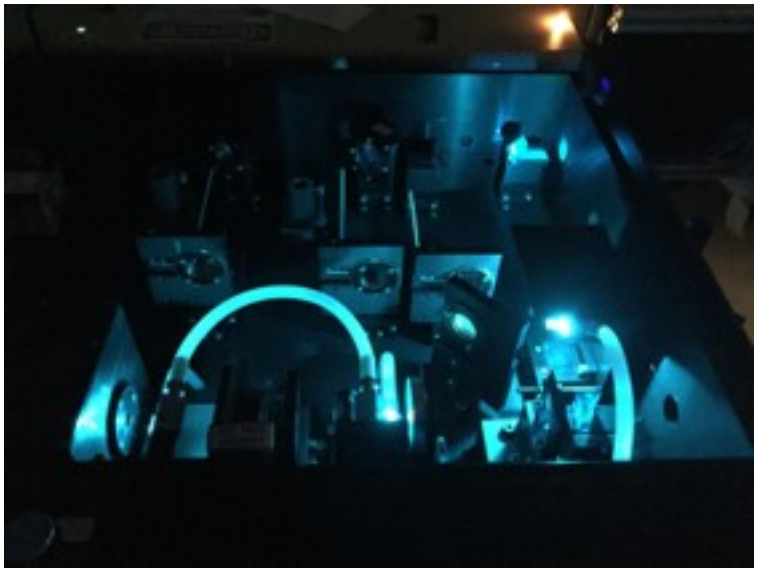

Figure 7.1: One of the laboratory's pulsed dye lasers in action. This laser has been filled with Coumarin 480 dye, which can lase at and above the wavelength of the ionization threshold of $5P_{3/2}$ state rubidium (479.1 nm). This particular dye is ideal for creating neutral plasma from rubidium atoms.

the internal oscillator and using an external laser as the reference point instead. This lowers the bandwidth of the PDL wavelength to about 100 MHz, which gives the user more control over the PI, ion recoil velocity, and initial plasma temperature. Our laboratory has two PDLs, one with an internal oscillator, and one without that can be injected locked. There are also several 480 nm cw blue lasers that can be used as the reference point, so injection locking is certainly possible given the current equipment. More information on injection locking can be found in Refs. [124–126].

There are several differences in the dynamics of neutral plasmas vs non-neutral plasmas, some of which were already discussed in Chapters 1 and 3. Neutral plasmas have lower initial temperatures than non-neutral plasmas due to the smaller electron and ion velocities post-PI, and they also expand at a slower rate because the charge neutrality suppresses Coulombic expansion. The presence of electrons also results in TBR while allowing additional oscillations, such as Langmuir waves, to occur. One particularly convenient aspect of neutral plasmas is that their temperature can be more easily ascertained using standard experimental techniques. Unlike non-neutral plasmas, which expand due to Coulomb force, neutral plasmas expand initially due to thermal effects. Therefore, the temperature of a neutral plasma can be determined through time-of-flight imaging [30]. This, along with pair correlation measurements, can give great insight into the time-evolved behavior of neutral plasmas, including the effects of DIH and TBR.

Another experiment idea that would only require minor changes to the setup is a study in plasma collision. The experiment in Chapter 4 centered around the expansion of a single cylindrical column of plasma, and it begs the question of what would happen if two plasma columns were

formed next to each other and were observed as they expanded and collided with each other. Making two, or potentially more, side-by-side plasma columns can be done by modifying the lower excitation (red) laser, and this can be done several different ways. The simplest option would be to place a screen, or even a double slit, along the path of the beam, creating fringes that would result in multiple plasma columns. A more complex approach would be to use diffraction optics to set the beam to a Hermite-Gaussian mode. The 01 and 10 Hermite-Gaussian modes, for instance, would make two plasma columns. The red beam could also be modified with Laguerre-Gaussian optics or a spatial light modulator, resulting in unusual plasma shapes [41].

The two aforementioned experiments do not require drastic changes to the experimental setup. This next experiment would require a good deal more time and effort to install, but the results would be worth the while. One major limitation of the current setup is that it can only observe two-dimensional ion pair correlations, a consequence of projecting the ions onto a 2D imaging plane. Plasmas naturally have three-dimensional pair correlations, so it would be worthwhile to modify the setup to enable observing these 3D correlations. One option would be to add another imaging system along an orthogonal direction, but this would be expensive and potentially not possible with space constraints. The other, easier option is to implement an imaging system that resolves each ion both temporally and spatially. In other words, the imaging system not only records the ion's position on the detector, but also its arrival time. With the arrival time for each ion, one can then use the arrival time along with the initial position to determine longitudinal pair correlations. Fortunately, there is a special type of MCP available called a "delay line detector" that is capable of this exact thing. Replacing the current MCP would take a considerable amount of time and would involve breaking vacuum, but the ability to measure three-dimensional ion pair correlations would be immensely powerful.

7.2 Rydberg Atom Photoionization Cross Sections

Future projects related to the photoionization studies in Chapter 5 can be split into two camps: experimental verification, and further computational offshoots.

Experimental verification has been discussed in Sec. 5.5, but to reiterate what was said there, the next logical step in this investigation is to explore these PI minima experimentally and see how the lab findings compare to the simulations. As mentioned earlier, of the five PI minima presented in Chapter 5, the easiest one to experimentally investigate would be the Rb shape resonance. This minimum is centered at a wavelength of 366 nm, and it has a high cross section compared to the other minima, resulting in an easier measurement in theory. The second-best candidates are the Rb and Cs $S \rightarrow P$ Cooper minima, whose minima are centered at wavelengths of 536 nm and 392 nm respectively. These minima have reasonably accessible wavelengths, but

they are less appealing than the Rb shape resonance because of their low overall cross sections and measurement difficulty. These PI cross-section scans can actually be performed in the ion/plasma imaging vacuum chamber. If the needle electrode were to be held at a low constant voltage, it would be able to direct photoionized ions to the MCP without field-ionizing any of the residual Rydberg atoms. The experiment would then involve scanning the PI laser over a suitable range at an adequate resolution; the PI minimum would be the wavelength at which ion production and detection are minimized.

Assuming this experiment successfully finds these PI minima, an interesting investigation would be to test these minima wavelengths in the context of optical lattices and optical dipole traps. This study would be particularly useful from a practical application perspective, as Rydberg atoms in optical traps are prone to photoionization. If Rydberg atoms in a specific ℓ-state were placed in an optical trap whose wavelength matched with a PI minimum, this would greatly increase the efficiency of the trap. For instance, traps for Rb nS Rydberg atoms could benefit from the Cooper minimum of Rb near $\lambda = 536$ nm, and traps for Rb nD Rydberg atoms could benefit from the shape resonance near $\lambda = 366$ nm. This Rb D-state, UV-based trap would be especially interesting in that, as of now, there are no recorded attempts of Rb optical traps using ultraviolet light. In general, UV dipole traps and lattices are uncommon, but there are known instances of using them to trap mercury [127]. It would be interesting to see how well a UV optical dipole trap would work for rubidium atoms in Rydberg D-states.

In Subsec. 5.2.2, I discussed how the PI cross sections could be calculated in the velocity form or the length form, but the velocity form is correct in this setting because the minimal-coupling Hamiltonian is velocity-dependent. This experimental measurement of PI cross section, in addition to providing valuable information for lattice and dipole trap applications, could also present an opportunity to compare the length and velocity forms. Opportunities like this are actually somewhat rare; even if the length and velocity forms provide different values for a given measurement, the difference is often not experimentally distinguishable. In these cross section calculations, though, the length-form and velocity-form locations of the minima differed by tens of nanometers. This is more than enough of a difference to detect experimentally, and it will be interesting to see which form is closer to the experimentally measured value.

Further computational offshoots can involve running similar calculations of PI cross sections for other atomic species. As long as a model potential exists for a certain element, these cross section calculations can be run. Alkali metals such as potassium and sodium, and other atomic species in different groups such as strontium and ytterbium would all make for interesting and useful studies. Another potential study would involve running cross section calculations for rubidium and cesium again, but this time using many-electron or even all-electron calculations instead of model potentials. While this would be more computationally demanding, it would not be an unreasonable feat, and it would have the added bonus of testing the accuracy of the model

potentials. There are past examples of using many-body Hartree-Fock calculations to find PI minima in low-lying states of sodium [128] and cesium [129], and it would not be onerous to adapt these calculations for Rydberg-state atoms.

7.3 Ball Lens MOT

The ball lens MOT project is still in its developmental phase. While the first prototype was successful, there are a number of design changes that can and should be made in the next build. I will discuss these necessary changes, along with some ongoing ideas about future implementations and upgrades.

The dimensions of the BLOB were determined to a large degree by the vacuum chamber used for testing the apparatus. This particular chamber is quite narrow along one direction, so in order to fit in the chamber, the BLOB wound up being cubic in shape with a side length of 19 mm. Subsequent computer simulations found that this physical design was on the cusp of not working, and that the MOT would have trapped and cooled more atoms if the physical dimensions of the BLOB and spacing between ball lenses were somewhat greater. To that end, any future ball lens MOT designs will aim to have a side length of 38-50 mm. These dimensions will allow for a much larger number of atoms to be trapped while still maintaining a smaller-than-usual overall size.

The impetus for creating a ball lens MOT in the first place is the lab's High-B chamber, shown in Fig. 7.2. This is a cryogenic chamber that uses liquid helium-cooled superconducting magnets to generate magnetic fields of up to 2.6 T. The chamber, which was used in the past to study laser cooling and Rydberg atoms in the presence of strong magnetic fields [67, 68], has been dormant for a while, but plans are in place to utilize it for more types of cold atom and cold plasma experiments. The inspiration for the ball lens MOT came from discussions on how to improve the optical molasses design inside of the High-B chamber (the High-B chamber cannot maintain a MOT because the applied magnetic fields would distort the MOT quadrupole field beyond use). Now that the first design of the ball lens MOT was proven successful, preliminary work can begin on building a new ball lens optical molasses for the High-B chamber. One thing to note is that the available space in the chamber is limited in the vertical direction, so the ball lens MOT may wind up being oblate in its design. Asymmetric ball lens MOT designs have not yet been explored, but the preexisting code can be easily adapted to test such a configuration.

Aside from integration into the High-B chamber, it will be interesting to see where the ball lens MOT project leads next. The Faraday caging provided by the metal structure makes it an excellent platform for studying plasmas and other charged systems. Additionally, future designs could see the addition of electrodes to the inside of the structure, as well as azimuthally-

Figure 7.2: The cryostat containing the High-B setup. The magnets in the High-B setup are superconducting coil magnets and must be chilled to 4 K in order to operate.

symmetric electric field distributions. This could lead to Paul, Penning, or cusp traps, all in a relatively compact structure. Separate from plasmas, the enclosure and small solid angle of the ball lenses leads to protection against blackbody radiation. This is especially important for atomic clocks and other precision measurement experiments, and it would be interesting to see how well a ball lens MOT performs in a precision measurement experiment. The ball lens MOT also offers potential for miniaturization and portability, two attributes which become more important as quantum technology and engineering advance.

7.4 Other Projects

This last section will be dedicated to the other projects I have worked on in graduate school. While they did not make the cut for any of the chapters, they represent important work and learning experiences.

7.4.1 Analysis of Penning Trap Vapor Cell

Many of the other projects I worked on in graduate school focused on EIT with Rydberg atoms. My most recent experiment is an analysis of a unique rubidium vapor cell made by my colleague and former lab mate, Lu Ma. This cell is special in that it features built-in ring electrodes made of conducting silicon. The electrodes are not just attached to the interior of the cell, they in fact make up part of the body of the cell. This is all possible with a method called anodic bonding.

When silicon is successfully attached to glass by anodic bonding, it forms a leak-proof seal. This particular cell features eight ring electrodes evenly spaced by six mm, and these electrodes can be used to make a variety of electric field configurations. One possible configuration is a constant electric dipole field, which could be used to form a Penning trap if paired with a longitudinal magnetic field.

Our analysis of this cell involved using Rydberg-EIT as a field probe to measure the cell's response to applied AC and DC fields. I was heavily involved in the AC measurements; this involved applying external microwave radiation from a horn to the cell, and then measuring the resulting Autler-Townes splitting in the Rydberg-EIT signal. One set of measurements was fairly standard and involved measuring the Autler-Townes splitting at different microwave powers to determine electric field strength. The other set of measurements was slightly more unusual and was made possible by the cell's design. In addition to creating electric field configurations, the silicon electrodes can also be used as polarization filters for microwave radiation. Thus, the other set of measurements involved placing the horn on a rotating mount and measuring the Autler-Townes splitting at different polarization angles. These results, along with corresponding HFSS simulations of the cell, have been posted to the arXiv [130] and will be published in a forthcoming paper.

The Penning trap cell has an exciting future ahead. One potential experiment in the near future would be to produce plasmas inside of the cell, and then trap the plasma ions with the Penning trap configuration. This could lead to studies on position-dependent plasma electric field measurements with EIT, which is sometime our group has been interested in for a while.

7.4.2 Cold-atom EIT and Quantum Optics

The final experiment I will discuss is actually the first experiment I worked on as a graduate student. Unlike the Penning cell experiment, where EIT was used as a tool to measure electric fields, this experiment was a fundamental study of EIT itself. EIT is a quantum, nonlinear process that causes both dispersive and absorptive changes in the atomic medium, and one effect is slowing down the speed of light. By using EIT, researchers have been able to slow down and even stop light from propagating within the atomic medium [131]. From a particle viewpoint, light moving through an EIT medium can be thought of as a delocalized quasi-particle called a polariton, which arises from a quasi-bound state between a photon and the cold atomic medium. From a quantum optics viewpoint, observing slow light at a very low power should reveal photon anti-bunching. Anti-bunching, and photon correlations in general, are often described with the $g^2(\tau)$ correlation function [132].

The experiment I conducted regarding this material was to induce Rydberg-EIT in a sample of cold atoms, measure pair correlations of atoms and photon correlations simultaneously,

and find interplay between the two correlations. This experiment used the same vacuum chamber and ion imaging system that would later be used for the plasma studies of Chapter 4. I worked on this experiment for a while, but I was ultimately unable to get meaningful data for a number of reasons. First, cold-atom EIT is objectively difficult to achieve, especially if the atoms are in free space. There have been successful attempts and measurements of cold-atom EIT when the atoms are in cavities [133], and this is because cavities can enhance the EIT response and measurable signal. I did not have a cavity though, so EIT signals were difficult to detect. The other main issue was that conditions that yielded good atom spatial correlation data yielded bad photon correlation data, and vice versa. Much time was spent trying to strike the balance between these two measurements, but I could never get them to appear simultaneously.

In the end, I still think this is a worthwhile experiment to pursue, but I would make a few changes. I would like to see how well this experiment operates if the atoms are placed in a cavity that enhances the probe laser response. The other big change would be to use two single-photon detectors instead of one for measuring temporal correlations. This way, the setup can have a proper Hanbury Brown-Twiss interferometer and can register correlations shorter than the dead time of each individual detector. Aside from the data side, this experiment taught me valuable lessons and helped me become more comfortable with the setups, which would up paying off with the plasma expansion experiments.

APPENDIX A

Calibrating the Ion Imaging System

This appendix will focus on the ion imaging chamber discussed in Chapter 4. Before any meaningful data can be taken, two things must happen: the magnification must be determined, and the external electric fields must be zeroed out. In the past, when the chamber was equipped to create Rydberg-state atoms, there was a specific procedure for magnification calibration and field-zeroing. Magnification was determined by placing a double slit in the path of the blue upper-excitation laser, creating a double slit interference experiment. By taking many images and combining them, we could produce interference patterns and use the known spacing between fringes to determine the magnification. Field-zeroing and calibration, meanwhile, was done by producing Stark maps of the Rydberg transitions for all three spatial dimensions.

When the experimental setup was modified for plasma experiments, the laser used for Rydberg excitation was removed and utilized in another setup, taking away the ability to use these techniques. As a result, I developed alternate methods for magnification calibration and field-zeroing. I will explain these new methods in the following sections.

A.1 Magnification

The magnification is determined by translating plasma cylinder transverse to its axis by a certain physical distance, and measuring the plasma image displacement on MCP. The last mirror that the lower excitation beam reflects off of before being focused and sent into the chamber is mounted on a Thorlabs KM100 mirror mount. This is a standard mount for 1" optics, with two screws that control vertical and horizontal displacement respectively. In a separate setup, I profiled this mount and measured how much a focused beam moved for a given angular displacement of the screw. In the experimental setup, I move the plasma cylinder from the top of the field of view to the bottom, and I measure the angular displacement of the screw required for this. Once I know the angular displacement, I know how much the plasma has moved. It typically takes $\sim$20

degrees of adjustment screw displacement to move the plasma from the top to the bottom of the field of view, which translates to a physical displacement of roughly 200 μm.

The MCP has an overall diameter of 18 mm, but in most cases, the ion imaging does not use the entire diameter. After the translation step above, I observe how much of the MCP diameter is actively being used. Usually, the active diameter is 12-13 mm. Once I know the active diameter, I can calculate the magnification by dividing the active diameter by the plasma's vertical displacement. Typical magnifications for this setup are in the 50-60$\times$ range, and the magnification can be increased by bringing the needle electrode closer to the plasma formation region.

A.2 Field-zeroing

Field-zeroing the chamber involves adjusting the fields based on how the ions strike the MCP, both spatially and temporally. In this section, the spatial coordinates used to describe the chamber are the coordinates shown in Fig. 4.1. Additionally, x and z will be referred to as the transverse coordinates, while y will be referred to as the longitudinal coordinate. The voltages applied to the electrodes have a resolution of 0.01 volts, and the electrodes are separated by about a centimeter, so the resolution of the field zeroing is $\sim$10 mV/cm.

To field-zero along the transverse coordinates, I adjust the voltages along the x and z directions until the ions are centered on the MCP. This is done for increasingly longer delay times between plasma formation and imaging – the idea here is that if the ions are exposed to stray fields for a longer time before imaging, they will be pushed further away from the center of the MCP. For the plasma expansion experiment, the longest delay time used for experimental data was 10 μs. When I field-zeroed beforehand, I looked at delay times as far out as 20 μs, so the amount of zeroing done was more than adequate for the experiment.

Field-zeroing along the longitudinal coordinate requires looking at ion arrival times, not their spatial distribution on the MCP. To do this, I look at ion arrival signals in real time on an oscilloscope. I start with zero delay time between plasma formation and imaging, and I place a cursor at the point where the ion signals are. Next, I pick a delay time τ, and I move the second cursor on the oscilloscope τ away from the first cursor. If the longitudinal fields are zeroed, then the ion signals should be shifted over by τ exactly and should be aligned with the second cursor once I change the delay time. If the signals arrive early or late, then they are being accelerated or decelerated along the y direction, and I adjust accordingly. Just like with the transverse directions, I field-zero the y direction to a delay time much longer than what is used experimentally.

One advantage that this new method of field-zeroing has over the previously used Stark map method is that this method takes much less time. The Stark map method usually took some-

where between several hours to a day to complete, depending on how high-resolution the scans were. By comparison, I can field-zero the chamber with this new method in about ten minutes. Care must be taken, though, to ensure that the electric fields are zeroed throughout the chamber and not just at the excitation center. At one point, I created an electric quadrupole field along the y direction whose zero point was the plasma excitation region. This ruined the free expansion and caused the ions to refocus and pile up on the MCP, as shown in Fig. 4.2(c).

APPENDIX B

Electromagnetically-Induced Transparency

Electromagnetically-induced transparency is a quantum, nonlinear optical effect that occurs in atoms. EIT drastically alters the susceptibility of the atomic medium, which causes changes to both the dispersive and the absorptive properties of the medium. EIT gets its name from its ability to make an atomic sample transparent to a wavelength it normally absorbs. It also modifies the dispersion of the medium and can cause light to slow down to m/s-level speeds, or even stop completely. Chapters 1 and 7 already went into some detail about what uses EIT has in experiments; this appendix will explain how to get EIT in the first place.

EIT requires three atomic energy levels at minimum. Additionally, this three-level system must have two optically allowed transitions. With these restrictions in mind, there are three possible configurations, each named after their apparent shapes: V, lambda, and ladder. Figure B.1 shows what all three of these configurations look like. This figure also features different colored arrows to signify the two transitions. The $|1\rangle \leftrightarrow |2\rangle$ transitions (red arrows) are the probe transitions, while the $|2\rangle \leftrightarrow |3\rangle$ transitions (blue arrows) are the coupler transitions. The probe is the transition/laser that is usually observed and analyzed, while the coupler is typically not observed after it passes through the atomic medium. The distinction between probe and coupler can vary in the V and lambda configurations. In the ladder configuration, the probe is usually the lower-excitation transition, but not always (e.g. a non-Rydberg $5S_{1/2} \leftrightarrow 5P_{3/2} \leftrightarrow 5D_{5/2}$ configuration for rubidium). To produce EIT signals, one laser is usually scanned while the other is kept constant. Either the probe or the coupler can be scanned to produce an EIT signal, and whichever laser is scanned is usually picked given the context of the particular experiment being done. The lambda and ladder configurations are the most used configurations for EIT. V configuration EIT can also be done, but is far less common.

To provide a rough explanation of how EIT works, imagine that the probe laser is sent into a room temperature atomic vapor and is scanned across resonance, with no coupler on. The resulting signal is a Doppler-broadened absorption profile that is centered at resonance. When the coupler laser is turned on, it begins to drive the $|2\rangle \leftrightarrow |3\rangle$ transition. Subsequently, the atomic

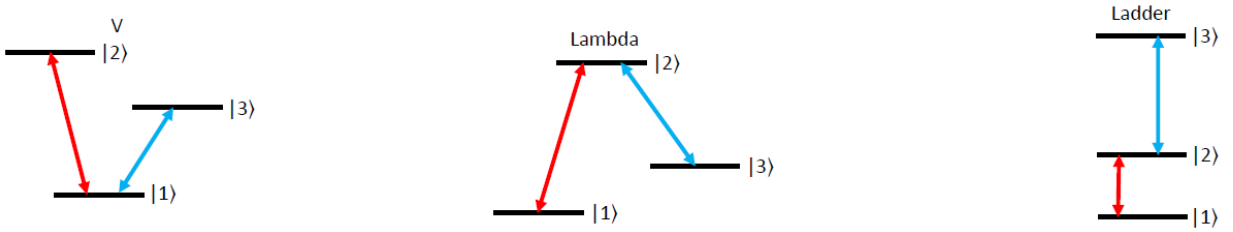

Figure B.1: V, lambda, and ladder EIT energy level configurations.

system ends up in a coherent superposition state of $|1\rangle$ and $|3\rangle$, and the excitation amplitudes in $|2\rangle$ destructively interfere. Thus, EIT is often referred to as a quantum interference effect. The superposition state of $|1\rangle$ and $|3\rangle$ is a "dark state" with respect to the probe laser, and this results in a spike in probe transmission at resonance, centered in the middle of the absorption profile. The EIT signal is narrower than the absorption profile because it is not affected by the Doppler effect.

For a more mathematically rigorous definition of EIT, see *Nonlinear Optics* by Boyd [134].

BIBLIOGRAPHY

[1] Foot, C. J., *Atomic Physics*, Oxford University Press, 2005.

[2] Gallagher, T. F., *Rydberg Atoms*, Cambridge University Press, Cambridge, 1994.

[3] Raab, E., Prentiss, M., Cable, A., Chu, S., and Pritchard, D., "Trapping of neutral sodium atoms with radiation pressure," *Phys. Rev. Lett.*, Vol. 59, 1987, pp. 2631 – 4.

[4] Metcalf, H. and van der Straten, P., *Laser Cooling and Trapping*, Springer, 1999.

[5] Phillips, W. D., "Nobel Lecture: Laser cooling and trapping of neutral atoms," *Rev. Mod. Phys.*, Vol. 70, Jul 1998, pp. 721–741.

[6] Schwarzkopf, A., Anderson, D. A., Thaicharoen, N., and Raithel, G., "Spatial correlations between Rydberg atoms in an optical dipole trap," *Phys. Rev. A*, Vol. 88, Dec 2013, pp. 061406.

[7] Thaicharoen, N., Schwarzkopf, A., and Raithel, G., "Measurement of the van der Waals interaction by atom trajectory imaging," *Phys. Rev. A*, Vol. 92, Oct 2015, pp. 040701.

[8] Thaicharoen, N., Goncalves, L. F., and Raithel, G., "Atom-Pair Kinetics with Strong Electric-Dipole Interactions," *Phys. Rev. Lett.*, Vol. 116, May 2016, pp. 213002.

[9] Grimmel, J., Stecker, M., Kaiser, M., Karlewski, F., Torralbo-Campo, L., Günther, A., and Fortágh, J., "Ionization spectra of highly Stark-shifted rubidium Rydberg states," *Phys. Rev. A*, Vol. 96, Jul 2017, pp. 013427.

[10] Stecker, M., Nold, R., Steinert, L.-M., Grimmel, J., Petrosyan, D., Fortágh, J., and Günther, A., "Controlling the Dipole Blockade and Ionization Rate of Rydberg Atoms in Strong Electric Fields," *Phys. Rev. Lett.*, Vol. 125, Aug 2020, pp. 103602.

[11] Gawlas, K. and Hogan, S. D., "Rydberg-state ionization dynamics and tunnel ionization rates in strong electric fields," *Phys. Rev. A*, Vol. 99, Jan 2019, pp. 013421.

[12] Veit, C., Zuber, N., Herrera-Sancho, O. A., Anasuri, V. S. V., Schmid, T., Meinert, F., Löw, R., and Pfau, T., "Pulsed Ion Microscope to Probe Quantum Gases," *Phys. Rev. X*, Vol. 11, Feb 2021, pp. 011036.

[13] Miller, S. A., Anderson, D. A., and Raithel, G., "Radio-frequency-modulated Rydberg states in a vapor cell," *New Journal of Physics*, Vol. 18, No. 5, May 2016, pp. 053017.

[14] Holloway, C. L., Gordon, J. A., Jefferts, S., Schwarzkopf, A., Anderson, D. A., Miller, S. A., Thaicharoen, N., and Raithel, G., "Broadband Rydberg Atom-Based Electric-Field Probe for SI-Traceable, Self-Calibrated Measurements," *IEEE Transactions on Antennas and Propagation*, Vol. 62, No. 12, 2014, pp. 6169–6182.

[15] Sedlacek, J. A., Schwettmann, A., Kübler, H., Löw, R., Pfau, T., and Shaffer, J. P., "Microwave electrometry with Rydberg atoms in a vapour cell using bright atomic resonances," *Nature Physics*, Vol. 8, Sep 2012, pp. 819.

[16] Sedlacek, J. A., Schwettmann, A., Kübler, H., and Shaffer, J. P., "Atom-Based Vector Microwave Electrometry Using Rubidium Rydberg Atoms in a Vapor Cell," *Phys. Rev. Lett.*, Vol. 111, Aug 2013, pp. 063001.

[17] Fan, H. Q., Kumar, S., Daschner, R., Kübler, H., and Shaffer, J. P., "Subwavelength microwave electric-field imaging using Rydberg atoms inside atomic vapor cells," *Opt. Lett.*, Vol. 39, No. 10, May 2014, pp. 3030–3033.

[18] Meyer, D. H., Cox, K. C., Fatemi, F. K., and Kunz, P. D., "Digital communication with Rydberg atoms and amplitude-modulated microwave fields," *Applied Physics Letters*, Vol. 112, No. 21, 2018, pp. 211108.

[19] Ma, L., Paradis, E., and Raithel, G., "DC electric fields in electrode-free glass vapor cell by photoillumination," *Opt. Express*, Vol. 28, No. 3, Feb 2020, pp. 3676–3685.

[20] Weller, D., Shaffer, J. P., Pfau, T., Löw, R., and Kübler, H., "Interplay between thermal Rydberg gases and plasmas," *Phys. Rev. A*, Vol. 99, Apr 2019, pp. 043418.

[21] Killian, T. C., Kulin, S., Bergeson, S. D., Orozco, L. A., Orzel, C., and Rolston, S. L., "Creation of an Ultracold Neutral Plasma," *Phys. Rev. Lett.*, Vol. 83, Dec 1999, pp. 4776–4779.

[22] Kulin, S., Killian, T. C., Bergeson, S. D., and Rolston, S. L., "Plasma Oscillations and Expansion of an Ultracold Neutral Plasma," *Phys. Rev. Lett.*, Vol. 85, Jul 2000, pp. 318–321.

[23] Pohl, T., Pattard, T., and Rost, J. M., "Plasma formation from ultracold Rydberg gases," *Phys. Rev. A*, Vol. 68, Jul 2003, pp. 010703.

[24] Pohl, T., Pattard, T., and Rost, J. M., "Coulomb Crystallization in Expanding Laser-Cooled Neutral Plasmas," *Phys. Rev. Lett.*, Vol. 92, Apr 2004, pp. 155003.

[25] Woolsey, N. C., Ash, A. D., Courtois, C., Dendy, R. O., Gregory, C. D., Hall, I. M., and Howe, J., "Collisionless Plasma Astrophysics Simulation Experiments using Lasers," *AIP Conference Proceedings*, Vol. 827, No. 1, 2006, pp. 365–375.

[26] McKenna, P., Neely, D., Bingham, R., and Jaroszynski, D. A., *Laser-Plasma Interactions and Applications*, Springer, 2011.

[27] Wessels, P., Ruff, B., Kroker, T., Kazansky, A. K., Kabachnik, N. M., Sengstock, K., Drescher, M., and Simonet, J., "Absolute strong-field ionization probabilities of ultracold rubidium atoms," *Comm. Physics*, Vol. 1, 2018, pp. 32.

[28] Djotyan, G., Bakos, J., Kedves, M., Ráczkevi, B., Dzsotjan, D., Varga-Umbrich, K., S´orlei, Z., Szigeti, J., Ignácz, P., Lévai, P., Czitrovszky, A., Nagy, A., Dombi, P., and Rácz, P., "Real-time interferometric diagnostics of rubidium plasma," *Nuclear Inst. and Methods in Physics Research A*, Vol. 884, 2018, pp. 25 – 30.

[29] Jiang, P. and Roberts, J. L., "Electric field influences on the initial electron temperature of ultracold plasmas," *Physics of Plasmas*, Vol. 26, No. 4, 2019, pp. 043513.

[30] Langin, T. K., Gorman, G. M., and Killian, T. C., "Laser cooling of ions in a neutral plasma," *Science*, Vol. 363, 2019, pp. 61.

[31] Lyon, M. and Rolston, S. L., "Ultracold neutral plasmas," *Rep. Prog. Phys.*, Vol. 80, 2017, pp. 017001.

[32] Murillo, M. S., "Ultrafast dynamics of neutral, ultracold plasmas," *Physics of Plasmas*, Vol. 14, 2006, pp. 005702.

[33] Ott, T., Bonitz, M., Stanton, L. G., and Murillo, M. S., "Coupling strength in Coulomb and Yukawa one-component plasmas," *Physics of Plasmas*, Vol. 21, No. 11, 2014, pp. 113704.

[34] Desbiens, N., Arnault, P., and Clérouin, J., "Parametrization of pair correlation function and static structure factor of the one component plasma across coupling regimes," *Physics of Plasmas*, Vol. 23, No. 9, 2016, pp. 092120.

[35] Sprenkle, T., Dodson, A., McKnight, Q., Spencer, R., Bergeson, S., Diaw, A., and Murillo, M. S., "Ion friction at small values of the Coulomb logarithm," *Phys. Rev. E*, Vol. 99, May 2019, pp. 053206.

[36] Boella, E., Paradisi, B. P., D'Angola, A., Silva, L. O., and Coppa, G., "Study on Coulomb explosions of ion mixtures," *J. Plasma. Phys.*, Vol. 82, 2016, pp. 904820110.

[37] Crockett, E. V., Newell, R. C., Robicheaux, F., and Tate, D. A., "Heating and cooling of electrons in an ultracold neutral plasma using Rydberg atoms," *Phys. Rev. A*, Vol. 98, Oct 2018, pp. 043431.

[38] Feldbaum, D., Morrow, N. V., Dutta, S. K., and Raithel, G., "Coulomb Expansion of Laser-Excited Ion Plasmas," *Phys. Rev. Lett.*, Vol. 89, Oct 2002, pp. 173004.

[39] Sous, J. and Grant, E. R., "Many-body physics with ultracold plasmas: quenched randomness and localization," *New J. Phys. (UK)*, Vol. 21, No. 4, 2019, pp. 043033.

[40] Anderson, D. A., Raithel, G., Simons, M., and Holloway, C. L., "Quantum-optical spectroscopy for plasma electric field measurements and diagnostics," 2017, arXiv:1712.08717 [physics.atom-ph].

[41] Murphy, D., Speirs, R. W., Sheludko, D. V., Putkunz, C. T., McCulloch, A. J., Sparkes, B. M., and Scholten, R. E., "Detailed observation of space–charge dynamics using ultracold ion bunches," *Nat. Commun.*, Vol. 5, 2014, pp. 4489.

[42] Morrison, J. P. and Grant, E. R., "Dynamics of colliding ultracold plasmas," *Phys. Rev. A*, Vol. 91, Feb 2015, pp. 023423.

[43] Forest, G. T., Li, Y., Ward, E. D., Goodsell, A. L., and Tate, D. A., "Expansion of an ultracold Rydberg plasma," *Phys. Rev. A*, Vol. 97, Apr 2018, pp. 043401.

[44] Samir, U., Wright Jr., K. H., and Stone, N. H., "The expansion of a plasma into a vacuum: Basic phenomena and processes and applications to space plasma physics," *Reviews of Geophysics*, Vol. 21, No. 7, 1983, pp. 1631–1646.

[45] Sack, C. and Schamel, H., "Plasma expansion into vacuum — A hydrodynamic approach," *Physics Reports*, Vol. 156, No. 6, 1987, pp. 311 – 395.

[46] Bychenkov, V. Y. and Kovalev, V., "Coulomb explosion in a cluster plasma," *Plasma. Phys. Rep.*, Vol. 31, 2005, pp. 178.

[47] Grech, M., Nuter, R., Mikaberidze, A., Di Cintio, P., Gremillet, L., Lefebvre, E., Saalmann, U., Rost, J. M., and Skupin, S., "Coulomb explosion of uniformly charged spheroids," *Phys. Rev. E*, Vol. 84, Nov 2011, pp. 056404.

[48] Gould, R. W., "Dynamics of non-neutral plasmas," *Phys. Plasma*, Vol. 2, 1995, pp. 2151.

[49] Walsh, D. and Dubin, D. H. E., "Bernstein modes in a non-neutral plasma column," *Physics of Plasmas*, Vol. 25, 2018, pp. 052119.

[50] Kaplan, A. E., Dubetsky, B. Y., and Shkolnikov, P. L., "Shock Shells in Coulomb Explosions of Nanoclusters," *Phys. Rev. Lett.*, Vol. 91, Oct 2003, pp. 143401.

[51] Drake, R. P., *High-Energy-Density Physics: Foundation of Inertial Fusion and Experimental Astrophysics*, Springer, 2006.

[52] Zerbe, B. S., Xiang, X., Ruan, C.-Y., Lund, S. M., and Duxbury, P. M., "Dynamical bunching and density peaks in expanding Coulomb clouds," *Phys. Rev. Accel. Beams*, Vol. 21, Jun 2018, pp. 064201.

[53] Pohl, T., Pattard, T., and Rost, J. M., "Relaxation to Nonequilibrium in Expanding Ultracold Neutral Plasmas," *Phys. Rev. Lett.*, Vol. 94, May 2005, pp. 205003.

[54] Gabrielse, G., Larochelle, P., Le Sage, D., Levitt, B., Kolthammer, W. S., McConnell, R., Richerme, P., Wrubel, J., Speck, A., George, M. C., et al., "Antihydrogen Production within a Penning-Ioffe Trap," *Phys. Rev. Lett.*, Vol. 100, Mar 2008, pp. 113001.

[55] Choi, J.-H., Knuffman, B., Zhang, X. H., Povilus, A. P., and Raithel, G., "Trapping and Evolution Dynamics of Ultracold Two-Component Plasmas," *Phys. Rev. Lett.*, Vol. 100, Apr 2008, pp. 175002.

[56] Schmid, S., Härter, A., Frisch, A., Hoinka, S., and Denschlag, J. H., "An apparatus for immersing trapped ions into an ultracold gas of neutral atoms," *Rev. Sci. Instrum.*, Vol. 83, No. 5, 2012, pp. 053108.

[57] Ma, L., *Electromagnetic Field Sensing with Rydberg Atoms in Vapor Cells*, Ph.D. thesis, University of Michigan, 2021.

[58] McMahon, B. J., Volin, C., Rellergert, W. G., and Sawyer, B. C., "Doppler-cooled ions in a compact reconfigurable Penning trap," *Phys. Rev. A*, Vol. 101, Jan 2020, pp. 013408.

[59] Andelkovic, Z., Cazan, R., Nörtershäuser, W., Bharadia, S., Segal, D. M., Thompson, R. C., Jöhren, R., Vollbrecht, J., Hannen, V., and Vogel, M., "Laser cooling of externally produced Mg ions in a Penning trap for sympathetic cooling of highly charged ions," *Phys. Rev. A*, Vol. 87, Mar 2013, pp. 033423.

[60] Goodwin, J. F., Stutter, G., Thompson, R. C., and Segal, D. M., "Resolved-Sideband Laser Cooling in a Penning Trap," *Phys. Rev. Lett.*, Vol. 116, Apr 2016, pp. 143002.

[61] Golovizin, A., Fedorova, E., Tregubov, D., Sukachev, D., Khabarova, K., Sorokin, V., and Kolachevsky, N., "Inner-shell clock transition in atomic thulium with a small blackbody radiation shift," *Nat. Commun.*, Vol. 10, Apr 2019, pp. 1724.

[62] Xu, Y.-L. and Xu, X.-Y., "Analysis of the blackbody-radiation shift in an ytterbium optical lattice clock," *Chin. Phys. B*, Vol. 25, No. 10, sep 2016, pp. 103202.

[63] Ushijima, I., Takamoto, M., Das, M., Ohkubo, T., and Katori, H., "Cryogenic optical lattice clocks," *Nat. Photonics*, Vol. 9, 2015, pp. 185–189.

[64] Flambaum, V. V., Porsev, S. G., and Safronova, M. S., "Energy shift due to anisotropic blackbody radiation," *Phys. Rev. A*, Vol. 93, Feb 2016, pp. 022508.

[65] Beloy, K., Zhang, X., McGrew, W. F., Hinkley, N., Yoon, T. H., Nicolodi, D., Fasano, R. J., Schäffer, S. A., Brown, R. C., and Ludlow, A. D., "Faraday-Shielded dc Stark-Shift-Free Optical Lattice Clock," *Phys. Rev. Lett.*, Vol. 120, May 2018, pp. 183201.

[66] Stebbings, R. F. and Dunning, F. B., *Rydberg States of Atoms and Molecules*, Cambridge University Press, 1983.

[67] Paradis, E., Zigo, S., Hu, K., and Raithel, G., "Characterization of laser cooling in a high-magnetic-field atom trap," *Phys. Rev. A*, Vol. 86, No. 2, 2012, pp. 023416.

[68] Paradis, E., Zigo, S., and Raithel, G., "Highly polar states of Rydberg atoms in strong magnetic and weak electric fields," *Phys. Rev. A*, Vol. 87, No. 1, 2013, pp. 012505.

[69] Goldston, R. J. and Rutherford, P. H., *Introduction to Plasma Physics*, Institute of Physics Publishing, 1995.

[70] Chen, F. F., *Introduction to Plasma Physics and Controlled Fusion*, Springer International Publishing, 2016.

[71] Donkó, Z., "Molecular dynamics simulations of strongly coupled plasmas," *J. Phys. A Math. Theor.*, Vol. 42, No. 21, May 2009, pp. 214029.

[72] Mansbach, P. and Keck, J., "Monte Carlo Trajectory Calculations of Atomic Excitation and Ionization by Thermal Electrons," *Phys. Rev.*, Vol. 181, May 1969, pp. 275–289.

[73] Viray, M. A., Miller, S. A., and Raithel, G., "Coulomb expansion of a cold non-neutral rubidium plasma," *Phys. Rev. A*, Vol. 102, Sep 2020, pp. 033303.

[74] Viray, M. A., Miller, S. A., and Raithel, G., "Expansion dynamics of a cold non-neutral plasma," 2019, arXiv:1911.05622 [physics.atom-ph].

[75] Schwarzkopf, A. D., *Imaging Spatial Correlations of Rydberg Excitations in Cold Atom Clouds*, Ph.D. thesis, University of Michigan, 2013.

[76] Miller, S. A., *Optical Measurements of Strong Radio-Frequency Fields Using Rydberg Atoms*, Ph.D. thesis, University of Michigan, 2017.

[77] Thaicharoen, N., *Spatial Imaging of Strongly Interacting Rydberg Atoms*, Ph.D. thesis, University of Michigan, 2017.

[78] Sapiro, R. E., *Bose Einstein Condensate Experiments in Optical Lattices*, Ph.D. thesis, University of Michigan, 2010.

[79] Chen, Y. C., Simien, C. E., Laha, S., Gupta, P., Martinez, Y. N., Mickelson, P. G., Nagel, S. B., and Killian, T. C., "Electron Screening and Kinetic-Energy Oscillations in a Strongly Coupled Plasma," *Phys. Rev. Lett.*, Vol. 93, Dec 2004, pp. 265003.

[80] Viray, M. A., Paradis, E., and Raithel, G., "Photoionization of nS and nD Rydberg atoms of Rb and Cs from the near-infrared to the ultraviolet spectral region," *New J. Phys*, Vol. 23, Jun 2021, pp. 063022.

[81] Cooper, J. W., "Photoionization from Outer Atomic Subshells. A Model Study," *Phys. Rev.*, Vol. 128, Oct 1962, pp. 681–693.

[82] Aymar, M., Luc-Koenig, E., and Farnoux, F. C., "Theoretical investigation on photoionization from Rydberg states of lithium, sodium and potassium," *J. Phys. B*, Vol. 9, No. 8, jun 1976, pp. 1279–1291.

[83] Aymar, M., Robaux, O., and Wane, S., "Central-field calculations of photoionisation cross sections of excited states of Rb and $Sr^+$and analysis of photoionisation cross sections of excited alkali atoms using quantum defect theory," *J. Phys. B*, Vol. 17, No. 6, Mar 1984, pp. 993–1007.

[84] Msezane, A. Z. and Manson, S. T., "Generality and Systematics of Multiple Minima in Photoionization Cross Sections of Excited Atoms," *Phys. Rev. Lett.*, Vol. 48, Feb 1982, pp. 473–475.

[85] Zatsarinny, O. and Tayal, S. S., "Photoionization of potassium atoms from the ground and excited states," *Phys. Rev. A*, Vol. 81, Apr 2010, pp. 043423.

[86] Yar, A., Ali, R., and Baig, M. A., "Evidence of a Cooper minimum in the photoionization from the $7s\ ^2S_{1/2}$ excited state of potassium," *Phys. Rev. A*, Vol. 88, Sep 2013, pp. 033405.

[87] Beterov, I. I., Mansell, C. W., Yakshina, E. A., Ryabtsev, I. I., Tretyakov, D. B., Entin, V. M., MacCormick, C., Piotrowicz, M. J., Kowalczyk, A., and Bergamini, S., "Cooper minima in the transitions from low-excited and Rydberg states of alkali-metal atoms," 2012, arXiv:1207.3626 [physics.atom-ph].

[88] Sahoo, S. and Ho, Y. K., "Photoionization of Li and Na in Debye plasma environments," *Physics of Plasmas*, Vol. 13, No. 6, 2006, pp. 063301.

[89] Lin, C. Y. and Ho, Y. K., "Influence of Debye plasmas on photoionization of Li-like ions: Emergence of Cooper minima," *Phys. Rev. A*, Vol. 81, Mar 2010, pp. 033405.

[90] Lin, C. and Ho, Y., "The photoionization of excited hydrogen atom in plasmas," *Computer Physics Communications*, Vol. 182, No. 1, 2011, pp. 125 – 129, Computer Physics Communications Special Edition for Conference on Computational Physics Kaohsiung, Taiwan, Dec 15-19, 2009.

[91] Felfli, Z. and Manson, S. T., "Influence of shape resonances on minima in cross sections for photoionization of excited atoms," *Phys. Rev. A*, Vol. 41, Feb 1990, pp. 1709–1710.

[92] Kar, S. and Ho, Y. K., "Shape resonance in the Ps^- system," *Phys. Rev. A*, Vol. 86, Jul 2012, pp. 014501.

[93] Boesten, H. M. J. M., Tsai, C. C., Verhaar, B. J., and Heinzen, D. J., "Observation of a Shape Resonance in Cold-Atom Scattering by Pulsed Photoassociation," *Phys. Rev. Lett.*, Vol. 77, Dec 1996, pp. 5194–5197.

[94] Boesten, H. M. J. M., Tsai, C. C., Gardner, J. R., Heinzen, D. J., and Verhaar, B. J., "Observation of a shape resonance in the collision of two cold $^{87}\mathrm{Rb}$ atoms," *Phys. Rev. A*, Vol. 55, Jan 1997, pp. 636–640.

[95] Yao, X., Qi, R., Liu, X., Wang, X., Wang, Y., Wu, Y., Chen, H., Zhang, P., Zhai, H., Chen, Y., and Pan, J., "Degenerate Bose gases near a d-wave shape resonance," *Nat. Phys.*, Vol. 15, 2019, pp. 570–576.

[96] Hamilton, E. L., Greene, C. H., and Sadeghpour, H. R., "Shape-resonance-induced long-range molecular Rydberg states," *Journal of Physics B: Atomic, Molecular and Optical Physics*, Vol. 35, No. 10, may 2002, pp. L199–L206.

[97] Peper, M. and Deiglmayr, J., "Formation of ultracold ion pairs through long-range Rydberg molecules," *J. of Phys. B*, Vol. 53, No. 6, feb 2020, pp. 064001.

[98] Marinescu, M., Sadeghpour, H. R., and Dalgarno, A., "Dispersion coefficients for alkali-metal dimers," *Phys. Rev. A*, Vol. 49, Feb 1994, pp. 982–988.

[99] Marinescu, M., Florescu, V., and Dalgarno, A., "Two-photon excitation of the 5^2D states of rubidium," *Phys. Rev. A*, Vol. 49, Apr 1994, pp. 2714–2718.

[100] Marinescu, M., Sadeghpour, H. R., and Dalgarno, A., "Dynamic dipole polarizabilities of rubidium," *Phys. Rev. A*, Vol. 49, Jun 1994, pp. 5103–5104.

[101] Reinhard, A., Liebisch, T. C., Knuffman, B., and Raithel, G., "Level shifts of rubidium Rydberg states due to binary interactions," *Phys. Rev. A*, Vol. 75, Mar 2007, pp. 032712.

[102] Friedrich, H., *Graduate Atomic Physics*, Springer International Publishing AG, Cham, 4th ed., 2017.

[103] Cardman, R., MacLennan, J., Anderson, S. E., Chen, Y.-J., and Raithel, G., "Photoionization of Rydberg Atoms in Optical Lattices," 2021, arXiv:2102.09622 [physics.atom-ph].

[104] Bethe, H. A. and Salpeter, E. E., *Quantum Mechanics of One- and Two-Electron Atoms*, Springer-Verlag, Boston, 1977.

[105] Sakurai, J. J. and Napolitano, J., *Modern Quantum Mechanics*, Addison-Wesley, San Francisco, 2nd ed., 2011.

[106] Anderson, S. E., Younge, K. C., and Raithel, G., "Trapping Rydberg Atoms in an Optical Lattice," *Phys. Rev. Lett.*, Vol. 107, Dec 2011, pp. 263001.

[107] Moore, K. R., Anderson, S. E., and Raithel, G., "Forbidden atomic transitions driven by an intensity-modulated laser trap," *Nat. Commun.*, Vol. 6, 2015, pp. 6090.

[108] Moore, K. R. and Raithel, G., "Probe of Rydberg-Atom Transitions via an Amplitude-Modulated Optical Standing Wave with a Ponderomotive Interaction," *Phys. Rev. Lett.*, Vol. 115, Oct 2015, pp. 163003.

[109] Lampen, J., Nguyen, H., Li, L., Berman, P. R., and Kuzmich, A., "Long-lived coherence between ground and Rydberg levels in a magic-wavelength lattice," *Phys. Rev. A*, Vol. 98, 2018, pp. 033411.

[110] Nichols, C. S., Nofs, L. M., Viray, M. A., Ma, L., Paradis, E., and Raithel, G., "Magneto-Optical Trap with Millimeter Ball Lenses," *Phys. Rev. Applied*, Vol. 14, Oct 2020, pp. 044013.

[111] Lee, J., Grover, J. A., Orozco, L. A., and Rolston, S. L., "Sub-Doppler cooling of neutral atoms in a grating magneto-optical trap," *J. Opt. Soc. Am. B*, Vol. 30, No. 11, Nov 2013, pp. 2869–2874.

[112] Imhof, E., Stuhl, B. K., Kasch, B., Kroese, B., Olson, S. E., and Squires, M. B., "Two-dimensional grating magneto-optical trap," *Phys. Rev. A*, Vol. 96, Sep 2017, pp. 033636.

[113] Lee, K., Kim, J., Noh, H., and Jhe, W., "Single-beam atom trap in a pyramidal and conical hollow mirror," *Opt. Lett.*, Vol. 21, No. 15, 1996, pp. 1177–1179.

[114] Arlt, J., Marago, O., Webster, S., Hopkins, S., and Foot, C., "A pyramidal magneto-optical trap as a source of slow atoms," *Opt. Commun.*, Vol. 157, No. 1-6, 1998, pp. 303–309.

[115] Vangeleyn, M., Griffin, P. F., Riis, E., and Arnold, A. S., "Single-laser, one beam, tetrahedral magneto-optical trap," *Opt. Express*, Vol. 17, No. 16, Aug 2009, pp. 13601–13608.

[116] Hinton, A., Perea-Ortiz, M., Winch, J., Briggs, J., Freer, S., Moustoukas, D., Powell-Gill, S., Squire, C., Lamb, A., Rammeloo, C., et al., "A portable magneto-optical trap with prospects for atom interferometry in civil engineering," *Philos. Trans. R. Soc. London, Ser. A*, Vol. 375, Oct 2016, pp. 20160238.

[117] Lu, Z., Corwin, K., Renn, M., Anderson, M., Cornell, E., and Wieman, C., "Low-velocity intense source of atoms from a magneto-optical trap," *Phys. Rev. Lett.*, Vol. 77, 1996, pp. 3331 – 4.

[118] di Stefano, A., Wilkowski, D., Müller, J., and Arimondo, E., "Five-beam magneto-optical trap and optical molasses," *Appl. Phys. B*, Vol. 69, No. 4, 1999, pp. 263–268.

[119] Edmund Optics Worldwide, "Understanding Ball Lenses," https://www.edmundoptics.com/knowledge-center/application-notes/optics/understanding-ball-lenses/, 2020.

[120] Kim, M.-S., Scharf, T., Mühlig, S., Fruhnert, M., Rockstuhl, C., Bitterli, R., Noell, W., Voelkel, R., and Herzig, H. P., "Refraction limit of miniaturized optical systems: a ball-lens example," *Opt. Express*, Vol. 24, No. 7, Apr 2016, pp. 6996–7005.

[121] Sasaki, M., Kurosawa, T., and Hane, K., "Micro-objective manipulated with optical tweezers," *Appl. Phys. Lett.*, Vol. 70, No. 6, 1997, pp. 785–787.

[122] Numata, T., Takayanagi, A., Otani, Y., and Umeda, N., "Manipulation of Metal Nanoparticles using Fiber-Optic Laser Tweezers with a Microspherical Focusing Lens," *Jpn. J. Appl. Phys.*, Vol. 45, No. 1A, jan 2006, pp. 359–363.

[123] Steck, D. A., "Rubidium 85 D line data," Available online at http://steck.us/alkalidata, Revision 2.1.6, 20 September 2013.

[124] Vrehen, Q. and Breimer, A., "Spectral properties of a pulsed dye laser with monochromatic injection," *Optics Communications*, Vol. 4, No. 6, 1972, pp. 416–420.

[125] Ganiel, U., Hardy, A., and Treves, D., "Analysis of injection locking in pulsed dye laser systems," *IEEE Journal of Quantum Electronics*, Vol. 12, No. 11, 1976, pp. 704–716.

[126] Siegman, A. E., *Lasers*, University Science Books, 1986.

[127] Yi, L., Mejri, S., McFerran, J. J., Le Coq, Y., and Bize, S., "Optical Lattice Trapping of ^{199}Hg and Determination of the Magic Wavelength for the Ultraviolet $^1S_0 \leftrightarrow ^3P_0$ Clock Transition," *Phys. Rev. Lett.*, Vol. 106, Feb 2011, pp. 073005.

[128] Saha, H. P., Froese-Fischer, C., and Langhoff, P. W., "Numerical multiconfiguration Hartree-Fock studies of atomic photoionization cross sections: Dynamical core-polarization effects in atomic sodium," *Phys. Rev. A*, Vol. 38, Aug 1988, pp. 1279–1285.

[129] Saha, H. P., "Multiconfiguration Hartree-Fock calculation of the photoionization of the Cs 7d excited state," *Phys. Rev. A*, Vol. 41, Jan 1990, pp. 174–180.

[130] Ma, L., Viray, M. A., Anderson, D. A., and Raithel, G., "Measurement of DC and AC electric fields inside an atomic vapor cell with wall-integrated electrodes," 2021, arXiv:2106.01968 [physics.atom-ph].

[131] Hau, L. V., Harris, S. E., Dutton, Z., and Behroozi, C. H., "Light speed reduction to 17 metres per second in an ultracold atomic gas," *Nature*, Vol. 397, 1999, pp. 594–598.

[132] Fox, M., *Quantum Optics: An Introduction*, Oxford University Press, 2006.

[133] Boddeda, R., Usmani, I., Bimbard, E., Grankin, A., Ourjoumtsev, A., Brion, E., and Grangier, P., "Rydberg-induced optical nonlinearities from a cold atomic ensemble trapped inside a cavity," *Journal of Physics B: Atomic, Molecular and Optical Physics*, Vol. 49, No. 8, apr 2016, pp. 084005.

[134] Boyd, R. W., *Nonlinear Optics*, Academic Press, Inc., 3rd ed., 2008.